

Absorption of Sunlight in Clear and Cloudy Atmospheres: A Solution to the Cloud Absorption Anomaly?

1). Crisp

Jet Propulsion Laboratory, California Institute of Technology, Pasadena, California

Received _____; accepted _____

Short title: ABSORPTION OF SUNLIGHT IN CLEAR AND CLOUDY ATMOSPHERES

Abstract.

Most global climate models underestimate the atmospheric absorption of sunlight by about 25 W m^{-2} . To identify the origin of this missing absorption, a spectrum-resolving (line-by-line) multiple scattering model was used to derive solar radiances, fluxes, and heating rates for realistic clear and cloudy atmospheres. Unlike the algorithms used in global climate models, this model accounts for virtually all of the observed absorption. Errors and oversimplifications in the treatment of water vapor, ozone, aerosols, and surface albedos appear to be responsible for most of the anomalous absorption. The present model shows that cloud-free, aerosol-free atmospheres over relatively dark ocean surfaces absorb $\sim 74.5 \text{ W m}^{-2}$ for global-annual-average illumination conditions and gas mixing ratios. The clear-sky atmospheric absorption increases with surface albedo as the atmosphere absorbs some of the more intense reflected solar flux. For example, the global-annual-average absorption increases to $\sim 80.5 \text{ W m}^{-2}$ for desert surfaces with albedos near 0.21. When realistic tropospheric aerosols with column-integrated visible optical depths near 0.1 and single scattering albedos between 0.9 and 0.95 are added to clear atmospheres, the clear-sky albedo increases, but the atmospheric absorption also increases by 6 to 8.5 W m^{-2} . Clouds produce much larger increases in the albedo of the system, but their effect on the atmospheric absorption depends on their water vapor abundance and their cloud-top altitude. In aerosol-free atmospheres, saturated low clouds increase the column-integrated atmospheric absorption by 5 to 12 W m^{-2} , while high clouds produce reductions of similar magnitude and middle clouds produce little net atmospheric radiative forcing. Even though aerosols embedded in clouds absorb little sunlight, realistic, weakly-absorbing aerosols above the cloud tops can reduce the albedo of the system and add to the atmospheric absorption. Both high-altitude tropospheric aerosols and weak visible ozone bands absorb more in cloudy regions or in regions over bright surfaces where they can absorb both the direct and reflected sunlight. The reflected sunlight that is scattered into the largest emission zenith angles

is most strongly attenuated by these constituents because it must traverse the longest optical paths on its way out of the atmosphere. Also, unlike absorbers embedded within the clouds, these optically-thin, high-altitude absorbers can increase the atmospheric absorption even at very large solar zenith angles. Atmospheres with plausible global cloud distributions and aerosol optical depths of 0.1 to 0.2 can absorb 81 to 87 W m^{-2} for global-annual-average illumination conditions. These values are consistent with results from recent observational studies, even though they show that clear-sky and all-sky regions absorb similar amounts of sunlight. Finally, these calculations suggest that realistic, weakly-absorbing tropospheric aerosols may reduce the Earth's albedo in cloudy regions more than they increase the albedos in clear regions. If this is the case, aerosols will produce a net positive solar radiative forcing rather than a negative forcing as many recent studies have predicted.

1. Introduction

Global satellite observations show that the Earth receives an average of 342 W m^{-2} from the sun and reflects about 30% of this energy (102 W m^{-2}) back to space (Wielicki et al. 1995). The remaining 240 W m^{-2} is absorbed by the surface and the atmosphere. However, the partitioning of this energy within this system, and the specific constituents responsible for this absorption are still poorly understood. Comparisons of solar flux measurements collected at the surface and from orbit show that the atmosphere may absorb as much as 86 to 98 W m^{-2} in the global-annual average (cf. Cess et al. 1995; 1996; Li and Moreau, 1996; Li et al. 1997). These measurements also indicate that cloudy regions often absorb up to 25 W m^{-2} more than clear regions. In contrast, the radiative transfer algorithms used in most global general circulation models (GCMs) yield estimates of the globally-averaged atmospheric absorption between 56 and 68 W m^{-2} , and indicate that clear and cloudy regions absorb similar amounts of solar radiation (Arking, 1996; Li et al. 1997). These results suggest that there may be a fundamental error or omission in the radiative transfer algorithms used in existing global climate models.

Because the largest discrepancies between theory and observation are often seen in cloudy regions, this phenomena has come to be known as the *cloud absorption anomaly* (Wiscombe, 1995; Cess et al., 1995; Ramanathan et al., 1995; Li et al. 1995; Li and Moreau, 1996). Several investigators have examined the absorption by cloud droplets and/or other constituents embedded within the clouds, but the origin of the anomalous absorption has not yet been determined. For example, Chou et al. (1995) and Ackerman and Toon (1996) find that cloud particles can account for the observed absorption only when their absorption is artificially increased by amounts large enough to require a substantial revision of our understanding of cloud particle microphysics. Lubin et al. (1996) find that near-infrared ($1.6 \mu\text{m}$) absorption by large ice crystals ($r > 100 \mu\text{m}$) could also enhance the absorption of sunlight at small solar zenith angles,

but this forcing decreases rapidly with increasing solar zenith angle, and therefore cannot account for the enhanced absorption often seen at high latitudes (Cess et al. 1995; 1996). Other studies implicate the effects of cloud spatial variability on the cloud albedo (Stephens and Tsay, 1990; Cahalan et al. 1994). These investigations indicate that spatially inhomogeneous clouds can sometimes have albedos that are up to 15% lower than those obtained from the commonly-used 1-dimensional radiative transfer models, but this mechanism can account for only 10 to 15% of the observed anomalous absorption in the global-annual average.

Taken together, these studies suggest that the anomalous absorption may be produced by atmospheric constituents other than the clouds themselves, and there is additional evidence to support this possibility. For example, Arking, (1996) finds that the amplitude of the anomalous absorption may be more strongly correlated with the column-integrated water vapor abundance than cloud amount. Imre et al. (1996) reanalyzed the data described by Cess et al. (1995) and concluded that the large differences between the atmospheric absorption in clear and cloudy skies was caused by underestimates of the clear sky absorption rather than the enhanced absorption in cloudy skies. This conclusion is reinforced by detailed comparisons between GCMs and observations, which show that most GCMs underestimate the clear-sky atmospheric absorption and overestimate the absorption by the surface by 10 to 15 W m^{-2} (Kiehl et al. 1994; Wild et al. 1995; 1996). Finally, cloud modeling studies show that if marine stratocumulus clouds absorbed enough solar radiation to explain the cloud absorption anomaly, they would be depleted of water during the middle of the day (Ackerman and Toon, 1996). Observations indicate that this does not happen.

Comparisons of results from rigorous line-by-line models and GCM radiative transfer algorithms suggest that errors and oversimplifications in the treatment of water vapor absorption by the GCM algorithms may account for a significant fraction of the cloud absorption anomaly (Fouquart et al., 1991; Ramaswamy and Freidenreich, 1992;

Crisp, 1997). Near-infrared (0.7 to 3 μm) absorption by water vapor dominates the absorption of solar radiation, and the solar heating rates at most tropospheric levels. Fouquart et al. (1991) found that GCM algorithms typically underestimated the water vapor absorption by 6 to 11% even in clear model atmospheres where water vapor was the only absorber. Much larger discrepancies between the benchmark line-by-line and GCM algorithms were seen in cloudy atmospheres. More recently, Crisp (1997) used a spectrum-resolving (line-by-line) multiple scattering model to estimate the absorption by water vapor in clear and cloudy atmospheres. That study shows that clear atmospheres with mid-latitude summer water vapor mixing ratios (McClatchey, 1972) can absorb up to 74.5 W m^{-2} , for global-annual-average illumination conditions. When saturated low clouds are added to this atmosphere, the absorption increases by an additional 12 W m^{-2} , to values near 86 W m^{-2} . However, middle and high clouds absorbed somewhat less than the clear-sky case, such that other absorbers were still needed to account for the amplitude of the all-sky absorption.

One source of extinction that has received relatively little attention in modeling studies of the cloud absorption anomaly is tropospheric aerosols. Even though empirical studies provide circumstantial evidence for enhanced aerosol absorption in cloudy atmospheres (Li and Moreau 1996, Li et al. 1997), the amplitude, distribution, and physical mechanism for this absorption have not yet been established. Most investigators have rationalized their omission because (i) they typically have much smaller optical depths than the clouds ($\tau_a \ll 1.0$ vs. $10 < \tau_{\text{cld}} \leq 100$), (ii) most common aerosol particles are only weakly absorbing at most solar wavelengths, and (iii) their spatial distribution and optical properties are not well characterized by existing global observations (cf. Kiehl and Briegleb, 1992; Kiehl and Trenberth, 1997). Negative results obtained in modeling efforts that have included the effects of absorbing tropospheric aerosols have also contributed to the limited attention that they have received. For example, Stevens and Tsay (1990) considered both internal and external mixtures of

absorbing aerosols within cloud layers, but concluded that unrealistically large amounts of absorbing material would be needed to significantly lower the cloud albedos. More recently, Lubin et al. (1996) considered the effects of absorbing aerosols on the solar radiative forcing by deep convective cloud systems. They found that even though aerosols can enhance the cloud radiative forcing at small solar zenith angles, this effect decreased too rapidly with solar zenith angle to explain the solar absorption anomaly.

These conclusions may be valid within their specific contexts, but they do not completely preclude a strong solar radiative forcing by aerosols in cloudy atmospheres. The principal shortcoming of these (and other) studies is that they neglect the effects of optically-thin absorbing aerosols distributed above the cloud tops. Such aerosols are often seen as discrete brown layers just above the cloud tops, or as diffuse hazes extending all of the way to the tropopause (cf. Jaenicke, 1993 and references therein). They will have little effect on the radiation field if they are buried under high clouds or if they are embedded in deep, optically-thick convective clouds (cf. Lubin et al. 1996). However, their absorption could be much larger if they are distributed above spatially-extensive middle and lower clouds decks because the solar radiation must traverse the aerosol layer both before and after it is reflected back to space. The sunlight that is diffusely reflected into the largest emission zenith angles by the clouds should be absorbed most efficiently by the aerosols because it must traverse the longest paths on its way out of the atmosphere. The absorption by these optically-thin, high-altitude aerosols complements the absorption by water vapor and cloud droplets because it is most effective at large solar zenith angles, where the other absorbers are least effective. Tropospheric aerosols should also enhance the atmospheric absorption over high-albedo surfaces (snow, sea ice, desert). When combined with the enhanced absorption over clouds, this absorption may account for a large fraction of the solar absorption anomaly at high latitudes.

The final absorbing constituent that might contribute to the cloud absorption

anomaly is ozone. This absorber has been largely ignored in theoretical investigations of this phenomena because the vast majority of the ozone is located at stratospheric levels, well above the cloud tops. It is important to note, however, that the satellite observations, which provide the only global constraints on the solar radiation budget at the top of the atmosphere, cannot clearly discriminate between absorbers within the clouds and those above the cloud tops. Observations acquired from high-altitude aircraft (cf. Pilewskie and Valero, 1995) share this shortcoming. The strong $0.25\ \mu\text{m}$ ozone Hartley band absorbs virtually all of the solar radiation at near-UV wavelengths before it reaches the tropopause. However, the much weaker Huggins (0.3 to $0.35\ \mu\text{m}$) and Chappuis bands ($0.6\ \mu\text{m}$) allow a significant fraction of the solar radiation to penetrate to the surface. These weak bands contribute only a few W m^{-2} to the solar radiation budget in clear skies, but their effects should be enhanced in cloudy regions and in regions with high surface albedos where they can absorb both the incoming and reflected solar radiation. Like the high-altitude tropospheric aerosols, the absorption by these weak ozone bands should be most effective at large solar zenith angles, and large backscattering emission angles.

Here, a comprehensive, spectrum-resolving (line-by-line) atmospheric radiative transfer model was used to assess the contributions by each of these absorbers to the solar radiation budget in clear and cloudy atmospheres. The radiative transfer modeling methods are described in the following section. These methods were used to produce high-resolution, angle-dependent solar radiance spectra, bolometric fluxes, and solar heating rates for a few representative clear, cloudy, and aerosol-laden model atmospheres (Section 3). These results are presented in Section 4, and their implications for the climate system are described in Section 5.

2. Methods

The radiative transfer algorithms used here were developed for thermal balance and remote sensing investigations of the atmospheres of Venus, Mars, and Neptune (cf. Crisp et al. 1994, 1995; Meadows and Crisp, 1996; Crisp and Titov 1997). These methods include a pair of related multi-level, spectrum-resolving (line-by-line) multiple scattering models that employ different approach for resolving the wavelength dependence of the atmospheric and surface optical properties and the solar source function. The Discrete Atmospheric Radiative Transfer (DART) model creates a spectral grid that is fine enough to completely resolve the spectral variability associated with near-infrared line absorption and UV pre-dissociation and electronic bands of gases, as well as the wavelength dependence of the optical properties of airborne particulate and the surface. This brute-force numerical model then performs a monochromatic multiple scattering calculation at each spectral grid point to produce a wavelength-dependent solar spectrum. The Spectral Mapping Atmospheric Radiative Transfer (SMART) model also explicitly resolves the wavelength and altitude dependence of the atmospheric and surface optical properties, but this model employs high-resolution spectral mapping methods (cf. Crisp and West, 1992; Meadows and Crisp, 1996) to minimize the number of monochromatic multiple scattering calculations needed to generate high resolution synthetic spectra in broad spectral regions. The spectrum- and altitude-dependent atmospheric gas absorption coefficients required by DART and SMART were provided by a line-by-line model (LBLABC, Meadows and Crisp 1996). The wavelength-dependent, single-scattering optical properties for spherical liquid water droplets, and hexagonal water ice crystals were derived with a Mie scattering model, and geometric optics model, respectively. A moderate-resolution solar spectrum was used for all simulations presented here (Wehrli, 1986). These methods are described in greater detail below.

2.1. The Radiative Transfer Models

130th DART and SMART use the multi-level, multi-stream, discrete ordinate algorithm, DISORT (Stamnes et al. 1988) to generate altitude- and angle-dependent solar radiances at each wavelength of interest. This algorithm is described in detail by Stamnes et al. (1988), and will only be summarized here. DISORT provides solutions to the monochromatic equation of transfer in plane parallel, scattering, absorbing atmospheres:

$$\mu \frac{dI(\tau, \mu, \phi, \nu)}{d\tau} = I(\tau, \mu, \phi, \nu) - S(\tau, \mu, \phi, \nu). \quad (1)$$

Here, I denotes the radiance, τ is the column-integrated vertical optical depth, measured from the top of the atmosphere downwards, μ is the cosine of the zenith angle, and ϕ is the azimuth angle. The source function, S , is defined by:

$$\begin{aligned} S = & \frac{\omega(\tau, \nu)}{4\pi} \int_0^{2\pi} d\phi' \int_{-1}^1 d\mu' P(\tau, \Theta, \nu) I(\tau, \Theta, \nu) \\ & + [1 - \omega(\tau, \nu)] B[\nu, T(\tau)] \\ & + \frac{\omega(\tau, \nu)}{4\pi} F_{\odot}(\nu) P(\tau, \Theta_{\odot}, \nu) \exp(-\tau/\mu_{\odot}) \end{aligned} \quad (2)$$

where $\omega(\tau, \nu)$ is the single scattering albedo, $P(\tau, \Theta, \nu) = P(\tau, \mu, \phi, \mu', \phi', \nu)$ is the scattering phase function, $B[\nu, T(\tau)]$ is the Planck function at wavenumber, ν , and temperature $T(\tau)$. $F_{\odot}(\nu)$ denotes the solar irradiance at the top of the atmosphere. DISORT was chosen for this application because of its speed and accuracy, and because a well-documented, numerically-stable code was readily available (W. Wiscombe, personal communication, 1992). The integrals in Eq. 2 are evaluated using Gaussian quadrature to yield radiances at a number of discrete zenith and azimuth angles for each atmospheric layer. Vertical inhomogeneity is accounted for by dividing the atmosphere

into a series of homogeneous layers. The optical properties ($\delta\tau$, ω , P) are assumed to remain uniform throughout each layer, but these properties can vary from layer to layer. When 4 or more streams are used, these methods usually produce angle dependent monochromatic radiance errors no larger than 1 % for clear, cloudy, and aerosol-laden atmospheres, but they will produce somewhat larger errors (1.0%) in atmospheres where Rayleigh scattering dominates because they neglect the effects of polarization (Adams and Kattawar; 1970; Mishchenko et al. 1994). These errors were considered acceptable for this investigation.

D] SORT, like most monochromatic multiple scattering algorithms, can provide accurate solutions to the equation of transfer only when it is used in spectral regions that are sufficiently narrow that the optical properties and source functions are roughly constant across each. The two radiative transfer models used in this investigation employ different approaches for resolving the wavelength dependence of the surface and atmospheric optical properties and the solar source function. The DART model simply divides the solar spectrum into a numerical grid that is sufficiently fine to completely resolve the wavelength dependence at all points along the optical path. The approach used to define the optimum spectral grid spacing is described in Meadows and Crisp (1996). DART then uses DISORT to perform a monochromatic multiple scattering calculation at each spectral grid point. Such methods are often called *line-by-line multiple scattering models*, by analogy to the line-by-line transmission models that are used for clear-sky transmission calculations at infrared wavelengths (cf. Fels and Schwarzkopf 1980; Clough et al. 1986). However, the term spectrum-resolving multiple scattering models is somewhat more appropriate because these models must resolve the wavelength dependence of UV electronic transitions of gases, the single scattering optical properties of cloud and aerosol particles, and surface albedos, as well as near-infrared gas absorption lines.

Direct numerical methods like DART should produce the most reliable results

possible because they use all of the available information about the atmospheric and surface optical properties, and employ a minimum number of approximations. Their principal drawback is their large computational expense. For example, for the calculations presented here, DART resolved the atmospheric and surface optical properties into about 3×10^6 unequally spaced spectral points at wavelengths between 0.125 and $8\mu\text{m}$. About 90% of these points were required at, near-infrared wavelengths (0.6 to $8\mu\text{m}$) where gas vibration-rotation transitions contribute to the spectral variability. DART then uses DISORT to perform a multi-level, multi-stream monochromatic multiple scattering calculation at each spectral grid point. For model atmospheres with 62 vertical levels, a 4-stream DART calculation usually requires 1 to 2 days to produce radiances, fluxes, and heating rates throughout the solar spectrum for a single solar zenith angle on a high-performance (mid-1990's vintage) desk-top workstation. Hence, even though these methods provide valuable standards for comparison, they are still impractical for routine use in GCMs.

The Spectral Mapping Atmospheric Radiative Transfer (SMART) model employs the same input data, the same spectral grid, and the same multiple scattering algorithm used by DART, but this model uses high resolution spectral mapping methods to enhance its computational speed (cf. Crisp and West, 1992; Meadows and Crisp, 1996). Like the correlated-k (c-k) method (Lacis and Wang, 1979; Lacis and Oinas, 1989; Goody et al. 1988; Fu and Lieu, 1993), and the optical depth binning method introduced by Ramaswamy and Freidenreich (1991), spectral mapping methods gain their efficiency by identifying monochromatic spectral intervals that have similar optical properties. These regions are then gathered into bins, and a single monochromatic multiple scattering calculation can be performed for each bin. However, the binning methods used in the spectral mapping algorithm differ from those used in the other two methods. In particular, both the c-k methods and the optical depth binning method assume that atmospheric optical properties are spectrally correlated at all points along

the optical path, such that monochromatic intervals with similar optical properties $(\delta\tau, \omega, P)$ at one level of the atmosphere will also remain similar at all other levels as well. If this condition holds, a monotonic ordering of the absorption coefficients (or optical depths) performed at any pressure level is exactly preserved at all other levels. This assumption is rigorously valid for homogeneous, isobaric, isothermal optical paths, but it usually breaks down for realistic inhomogeneous, non-isothermal, atmospheric optical paths. This loss of correlation can sometimes introduce significant flux and heating rate errors (cf. Goody et al. 1989, West et al. 1990; Fu and Liou, 1993). In contrast, spectral mapping methods make no assumption about the spectral correlation along the optical path. Instead, these methods perform a level-by-level comparison of monochromatic atmospheric and surface optical properties, and combine only those spectral regions that actually remain in agreement at all points along the inhomogeneous optical path. The spectral mapping approach is more computationally intensive and provides a substantially lower binning efficiency than that obtained with these other methods, but it is usually more reliable for use in inhomogeneous, non-isothermal atmospheres because it specifically avoids errors associated with the loss of correlation along the optical path.

SMART generates a high-resolution, angle-dependent solar radiance spectrum through the following series of steps. Like DART, it first defines the composite (gas and particulate) optical depths, $\tau(\nu_i, z_j)$, single scattering albedos, $\omega(\nu_i, z_j)$, and scattering phase functions, $P(\nu_i, z_j, \Theta_k)$ for each atmospheric layer, $z_j + dz_j$, at each spectral grid point, ν_j , in a multi-layer, scattering, absorbing atmosphere (cf. Lieu et al. 1978). Surface albedos, $a(\nu_i)$, and bi-directional reflection functions, $P_s(\nu_i, \Theta_k)$ are also specified as the lower boundary of the model, and solar fluxes are determined at the top of the atmosphere at each spectral grid point. Then, the spectral mapping algorithm employs a user-defined binning criteria to identify all spectral grid points that have optical properties that remain similar at all levels of the atmosphere and at the surface

(cf. West et al. 1990). Similar monochromatic intervals are collected into bins. Unlike the broad-band spectral mapping methods introduced by West et al. (1990), SMART then records the bin number associated with each grid point in a spectral map that is later used to map the computed radiances back to a full-resolution spectral grid.

For the calculations presented here, the spectral binning requirements were specified such that all contributions to a given bin must have optical properties that differ by no more than a constant fractional amount from that of the mean value in that bin at all points along the optical path (e.g. Method 2 in West et al. 1990). Specifically, the optical depths, single scattering albedos, and scattering phase functions for bin, l , and spectral grid point, ν_i must satisfy the constraints:

$$\delta\tau(\nu_i, z_j) = \delta\tau(l, z_j) \pm 0.25\delta\tau(l, z_j) \quad (3)$$

$$[1 - \omega(\nu_i, z_j)] = [1 - \omega(l, z_j)] \pm 0.1[1 - \omega(l, z_j)] \quad (4)$$

$$P(\Theta, \nu_i, z_j) = P(l, z_j, \Theta) \pm 0.1P(l, z_j, \Theta_k) \quad (5)$$

at all levels of the atmosphere, z_j . In addition, the surface albedos must satisfy the requirement that

$$a(\nu_i) = a(l) \pm 0.1a(l). \quad (6)$$

If all of these conditions are satisfied, grid point ν_i would be added to bin 1. In practice, the radiance errors introduced by this process rarely exceed 10 to 20% of the binning criteria (ie. a ± 0.1 binning requirement typically yields a 1 to 2% radiance error) because each spectral grid point must pass all of the binning requirements at all levels of the atmosphere, and at the surface to be added to that bin.

Once all similar spectral points have been gathered into bins, the mean optical properties for the bin are computed (cf. West et al. 1990), and DISORT is used to

perform a single monochromatic multiple scattering calculation for each bin (assuming a unit solar flux at the top of the atmosphere). For the calculations presented here, monochromatic radiances were obtained for 4 to 32 zenith angles (or *streams*) at 62 levels between the surface and 80 km. Spectrally-resolved radiances and fluxes were obtained for 4 to 8 solar zenith angles between 0 and 85°. The computed level-dependent radiances for each bin are then mapped back to their original spectral grid points, and multiplied by the solar flux at that wavelength to produce a high-spectral-resolution, angle-dependent description of the radiation field at each atmospheric level.

For the calculations presented here, SMART combined the $\sim 3 \times 10^6$ discrete spectral segments between 0.125 and $8 \mu\text{m}$ into about 3.6×10^4 unique spectral bins. The radiance spectra were then convolved with a 2 cm^{-1} wide (full-width at half maximum) triangular slit function for presentation, or integrated over angle and wavenumber to yield bolometric solar fluxes and heating rates. Comparisons between SMART and DART indicate that even though spectral mapping methods can reduce the number of monochromatic calculations needed in broad spectral intervals by about a factor of ~ 80 , they rarely introduce radiance errors larger than 2% in spectral intervals wider than 1 cm^{-1} . The spectral mapping algorithm adds some computational overhead, but this approach still reduces the computing time required for broad-band solar and thermal calculations in scattering, absorbing atmospheres by factors ranging from 40 (4 streams) to 80 (32 streams). SMART therefore provides the accuracy and efficiency needed for sensitivity studies, even on a global scale, but they still do not provide the computational speed needed for routine use in coupled GCMs. Comparisons of fluxes and heating rates obtained with SMART and DART are presented in Section 4.1.

The effects of clouds, gases, and aerosols were determined by computing the bolometric upward and downward ($F \downarrow$) solar irradiances (or *fluxes*) for clear and cloudy model atmospheres. If $F \downarrow(z)$ and $F \uparrow(z)$ are the spectrally-integrated (bolometric) downward and upward fluxes at level, z , the net downward solar flux at each atmospheric

level is given by:

$$F^n(z) = F \downarrow(z) - F \uparrow(z) \quad (7)$$

The value of this quantity at the top of the atmosphere indicates the total solar flux absorbed by the surface-atmosphere system. The net downward atmospheric fluxes at each level, F_a^n , were defined by subtracting the net downward flux at the surface from the total net downward flux at each atmospheric level:

$$F_a^n(z) = F^n(z) - F^n(z = 0). \quad (8)$$

The value of this quantity at the top of the atmosphere indicates the column-integrated solar flux absorbed by the atmosphere.

Bolometric solar fluxes and heating rates were integrated over solar zenith angle to approximate globally-averaged illumination conditions. To perform this integration, fluxes and heating rates that were obtained at a small number of discrete solar zenith angles (4 to 8) were first interpolated to a high resolution grid (~ 10 , using cubic splines), and then integrated numerically using the trapezoid rule. The globally-averaged net atmospheric flux was defined by:

$$\begin{aligned} \overline{F_a^n}(z) &= \frac{1}{2} \int_0^1 F_a^n(\mu, z) d\mu \\ &= \frac{1}{4} \sum_{i=2}^N [F_a^n(\mu_i, z) + F_a^n(\mu_{i-1}, z)] \Delta\mu_i \end{aligned} \quad (9)$$

where $\Delta\mu_i = \mu_i - \mu_{i-1}$ is the differences between the cosines of the solar zenith angles for points i and $i + 1$. Similarly, if the solar heating rates at solar zenith angle, μ , and level, z are defined by:

$$Q = \frac{1}{\rho c_p} \frac{\partial F^n}{\partial z} = -\frac{g}{c_p} \frac{\partial F^n}{\partial p} \quad (10)$$

where ρ is density, c_p is the specific heat at constant pressure for air, and g is the gravitational acceleration, the global-average heating rates were obtained from an expression of the form:

$$\begin{aligned}\bar{Q}(z) &= \frac{1}{2} \int_0^1 Q(\mu, z) d\mu \\ &= \frac{1}{4} \sum_{i=2}^N [Q(\mu_i, z) + Q(\mu_{i-1}, z)] \Delta\mu_i.\end{aligned}\tag{11}$$

Globally-average fluxes and heating rates derived from values evaluated at 8 discrete solar zenith angles (0, 15, 30, 45, 60, 75, 80, 85°) differed by less than 0.3% from those obtained from values evaluated at only 4 solar zenith angles (0, 30, 60, 85°). Only 4 solar zenith angles were therefore used for most of the globally-averaged results reported here.

2.2. Absorption and Scattering by Gases

Spectrum-resolving multiple scattering models like SMART and DART require a comprehensive, wavelength dependent description of the optical properties of gases and airborne particles. The monochromatic gas absorption coefficients for H₂O, CO₂, O₃, N₂O, CH₄, CO, and O₂ were obtained at 62 levels between the surface and 80 km with the line-by-line model, LBLABC (Meadows and Crisp, 1996). This model employs an efficient, multi-grid algorithm that completely resolves the cores of gas absorption lines at all atmospheric levels, and includes their contributions at large distances (1000 cm⁻¹) from the line centers. A Voigt line shape was used at line-center distances less than 40 times the Doppler half-width (Humlicek, 1982). At larger distances from the line center, a Van Vleck-Weisskopf profile modified by a x-factor is used (Meadows and Crisp, 1996). H₂O continuum absorption was explicitly included by using the far-wing x-factor recommended by Clough et al. (1989). A x-factor was also used to simulate the

sub-Lorentzian line profiles for CO_2 and CO . These line profiles have been extensively tested against existing laboratory measurements and high-resolution spectroscopic observations of planetary atmospheres (cf. Clough et al. 1989; Meadows and Crisp, 1996).

At each frequency of the output spectral grid, contributions were included from all spectral lines located at distances less than a specified line cut-off distance, ν_c . The line cut-off distance for all gases besides H_2O was 500 cm^{-1} . The nominal H_2O line cut-off was 1000 cm^{-1} , but alternative absorption coefficient files were generated with $\nu_c(\text{H}_2\text{O}) = 10 \text{ cm}^{-1}$ to test the effects the near-infrared far-wing continuum. The spectral line parameters for all gases at near-infrared wavelengths were obtained from the HITRAN 96 database (Rothman et al. 1992). The UV and visible absorption cross-sections for gases were derived from DeMore et al. (1992). Rayleigh scattering by air molecules was also included at all solar wavelengths (McCartney, 1976; Young, 1980).

2.3. Cloud Optical Properties

The lower and middle clouds were assumed to be composed of polydispersions of spherical liquid water droplets. Two-parameter gamma distributions were adopted for both cloud types. The mean radii and variances for Stratocumulus (SC) and Altostratus (AS) clouds specified by Hansen (1971) were used here. Their single scattering optical properties were computed with a Mie scattering model that incorporates the MIEV0 algorithm (Wiscombe, 1980), and methods for integrating over a broad range of particle size distributions (Hansen and Travis, 1974). Cirrus clouds were parameterized as $30 \mu\text{m}$ diameter by $200 \mu\text{m}$ long hexagonal ice crystals. Their optical properties were derived using a geometric optics algorithm based on a modified Kirchhoff approximation (Muinonen et al. 1989). The wavelength-dependent liquid water and ice refractive indices were obtained from Segelstein (1981) and Warren, (1984), respectively.

2.4. Aerosol Optical Properties

Four different aerosol compositions and three aerosol size distributions were used in these simulations. The wavelength dependent optical properties for the tropospheric aerosols were derived from refractive index data compiled by E. P. Shettle (included on the HITRAN96 CD ROM). These aerosols were divided into background aerosols, which were assumed to have constant number densities between the surface and the tropopause, and a boundary layer aerosol population, whose number densities decreased rapidly with increasing altitude (cf. Jaenicke, 1993). The nominal background aerosols were simulated an external mixture of particles, whose composition was compiled from a variety of sources (Toon and Pollack, 1976; Jaenicke, 1993; d'Almeida et al., 1991; Penner et al., 1994; Chýlek et al., 1996; Li et al., 1996). About half of the aerosol population (48%) was assumed to consist of ammonium sulfate particles, which are almost conservative scatterers at wavelengths shorter than 3 μ m. Weakly-absorbing dust-like and water-soluble aerosols (imaginary refractive index, $0.005 < n \leq 0.02$) were each assumed to contribute 25% of the remaining population. Strongly-absorbing carbonaceous aerosols ($n \sim 0.5$) contributed only 2% to the background aerosol population. This composition may not characterize the background aerosols at any particular location, but it should provide a reasonably representative globally-averaged composition. The boundary layer aerosol population consisted of equal amounts of sea salt and ammonium sulfate, both of which are almost conservative scatterers at most solar wavelengths.

The nominal particle size distribution for the background aerosols was based on the tri-modal, log-normal background aerosol distribution (Jaenicke, 1993):

$$\frac{dN(r)}{d(\log r)} = \sum_{i=1}^3 \frac{n_i}{\sqrt{2\pi} \log \sigma_i} \exp \left\{ -\frac{(\log r / R_i)^2}{2 (\log \sigma_i)^2} \right\} \quad (12)$$

The modal radii and variances for these particles are listed in Table 1. The tri-modal log-normal Maritime particle size distribution suggested by Jaenicke (1993) was used

for the boundary layer aerosols. The mid-tropospheric power-law size distribution suggested by Toon and Pollack (1976) was adopted as an alternate background aerosol size distribution. This size distribution has the form:

$$\frac{m'(r)}{d(\log r)} = \begin{cases} C & r < r_0 \\ a_i \left(\frac{r_0}{r}\right)^{(\beta_i+1)} & r_i \leq r < r_{i+1} \end{cases} \quad (13)$$

where $r_0 = 0.045 \mu\text{m}$, $r_1 = 5.0 \mu\text{m}$, $r_2 = 50 \mu\text{m}$, $\beta_1 = 2.6$, and $\beta_2 = 4.0$. C and a_i are normalization constants. These size distributions are illustrated in Figure 1. All aerosol particles were assumed to be spherical and their optical properties were derived with the Mie scattering model. The derived optical properties shown in Figures 2 to 4 are generally consistent with global observations of aerosol optical properties (d'Almeida et al., 1991; Jaenicke, 1993; Anderson et al. 1996; Hegg et al. 1996; and references listed in Table 8 of Liousse et al., 1996).

3. Model Atmospheres and Surfaces

The McClatchey et al. (1972) mid-latitude summer (MLS) atmospheric temperature profile was used in all experiments presented here. The MLS gas mixing ratios were adopted for all gases except H_2O (Figure 5). The MLS water vapor mixing ratios were used only for the nominal clear-sky simulations. Alternate clear-sky water vapor mixing ratio profiles were used to determine the relationship between the water vapor abundance and the net solar flux. These profiles included the McClatchey et al. (1972) sub-arctic winter (SAW'), sub-arctic summer (SAS), mid-latitude winter (MLW), and a globally-average water vapor profile derived from the climatological results published by Peixoto and Oort (1992). These profiles are shown in Figure 6. In cloudy atmospheres, the MLS water vapor mixing ratios were used everywhere except within and just below the clouds. At levels within the clouds, water vapor mixing ratios were increased to their saturation values (Crisp, 1997), and then held constant below the clouds until they intersected the background MLS values (Figure 7). The cloudy model atmospheres

included a single, plane-parallel cirrus (Cir), alto-stratus (AS), or stratocumulus (SC) cloud layer, or combinations of two of these cloud layers. The range of optical depths and cloud altitudes is summarized in Table 2.

A range of boundary layer and background aerosol distributions were considered in these calculations. Existing measurements indicate that boundary layer aerosols are concentrated near the surface, and have concentrations that vary dramatically with location and time. Their effects were simulated by adopting boundary layer aerosol distributions with particle scale heights of 1 km and column-integrated visible (0.5 μm) optical depths of $0.0 \leq \tau_a \leq 0.1$. In contrast, existing observations indicate that the background aerosol populations at levels above the boundary layer are much more uniformly mixed, with globally-averaged number densities between 10 and 1000 en^{-3} and column-integrated visible optical depths between 0.05 and 0.2 (Toon and Pollack; 1976; Jaenicke, 1993). A series of uniformly mixed (constant number density) aerosol distributions were therefore developed with column-integrated visible optical depths of $\tau_a(0.6\mu\text{m}) = 0.0, 0.1, 0.15, \text{ or } 0.2$. These optical depths are consistent with constant number densities of 0, 10, 15, or 20 particles per cubic centimeter (cm^{-3}) for the nominal Jaenicke (1993) background aerosol size distribution (which has extinction cross sections, $\sigma(0.6\mu\text{m}) \sim 1\mu\text{m}$), or values about 100 times larger for the much smaller Toon-Pollack distribution ($\sigma(0.6\mu\text{m}) \sim 0.01\mu\text{m}$). This range of optical depths is consistent with nominal values observed over a broad range of locations, (cf. d'Almeida et al. 1991; Leiterer et al. 1992; Dutton, et al. 1994; Penner et al. 1994; Villevalde et al. 1994; Esposito et al. 1996; Smirnov et al., 1994, 1996; Kaufman and Holben, 1996; Charlock and Alberta, 1996; Clarke et al. 1996; Liou et al. 1997). However, it does not include the much larger values often observed in heavily industrialized regions, or areas with active biomass burning (cf. Anderson et al., 1996).

Three different surface albedo spectra were used in these simulations. The spectrum of a moderately rough ocean surface ($0.05 \leq a \leq 0.07$) was adopted as the nominal

surface. A desert albedo spectrum (actually a spectrum of the planet Mars) was adopted as the first of two alternate albedo spectra. The wavelength dependence and the solar-flux-weighted average of this spectrum ($a \sim 0.2$) are similar to those of central Australia or the Atmospheric Radiation Measurement (ARM) Program's Cloud and Radiation Testbed (CART) site in Oklahoma. A fresh snow surface was also used (O'Brien et al., 1975). These surface albedos are shown in Figure 8.

4. Results

4.1. Model Validation

To validate the spectral mapping methods that were used for the majority of the sensitivity tests presented here, both the SMART and DART models were used to compute the solar radiation fields for clear and cloudy model atmospheres. These tests employed a solar zenith angle of $\theta_{\odot} = 60^{\circ}$ and surface albedos for a relatively rough ocean surface (Figure 8). The cloudy atmosphere includes a single, optically-thick stratocumulus cloud deck ($\tau_c(0.5\mu\text{m})=60$) at altitudes between 1 and 1.5 km (~ 0.82 to 0.9 Bars). The nominal MLS gas mixing ratios were used for all gases in clear atmospheres, and for all gases besides water vapor in cloudy atmospheres. The nominal H_2O profile for a saturated stratocumulus cloud deck was used in the cloudy case (Figure 7). No aerosols were included in these validation tests.

Computed upward (reflected) solar flux spectra at the top of clear and cloudy atmospheres obtained with SMART and DART are compared in Figure 9. Vertical profiles of the spectrally-integrated net solar flux, $F^n(z)$, the atmospheric net solar flux, $F_a(z)$, and the solar heating rate, $Q(z)$, are shown in Figure 10, 11 and 12, respectively. Differences between the results obtained by SMART and DART are barely discernible in these figures, confirming that the spectral mapping methods employed by SMART rarely contribute errors larger than a few percent. The largest errors are seen at the

shortest wavelengths (0.3 to $0.4\mu\text{m}$) and at the highest altitudes considered here ($p \leq 0.002$ Bar). These errors contribute little to the solar radiation budget.

Figure 9 illustrates the principal effects of clouds and absorbing gases on the solar radiation budget. Optically-thick clouds increase the intensity of the reflected solar flux by a factor of 3 to 4 (at $\theta_{\odot} = 60^\circ$). The absorption features centered near 0.6, 0.65, 0.70, 0.72, 0.82, 0.94, 1.1, 1.4, and $1.9\mu\text{m}$ are water vapor bands. The sharp features near 0.69 and $0.76\mu\text{m}$ are O_2 bands. The broad absorption feature centered near $0.6\mu\text{m}$ is the weak ozone Chappuis band. Ozone is also the principal absorber at wavelengths less than $0.4\mu\text{m}$. These gas absorption features are somewhat stronger in regions occupied by low clouds or bright, reflecting surfaces because the solar radiation must traverse most of the atmospheric column twice, and these bands absorb both the incoming and reflected solar radiation. The absorption by these bands is somewhat reduced in regions occupied by high clouds, which reflect the sunlight back to space before it can traverse much of the atmospheric column.

The vertical distribution of solar energy in clear and cloudy atmospheres is illustrated by Figures 10 - 12. Figure 10 shows that even though the clear-sky case absorbs about 3 times as much solar radiation as the cloudy sounding (at $\theta_{\odot} = 60^\circ$), the majority of the additional solar radiation absorbed under clear skies is deposited at the surface. In spite of this, Figure 11 shows that the cloudy atmosphere actually absorbs almost 20 W m^{-2} more than the clear case. The majority of the additional atmospheric flux divergence occurs within the cloud or above the cloud top. This behavior is also seen in the solar heating rates. Figure 12 reveals enhanced solar heating by water vapor in the vicinity of the cloud top, as well as enhanced heating at stratospheric levels that is produced as the weak near UV and visible ozone bands absorb some of the reflected solar radiation. The enhanced absorption at levels above and within the cloud is compensated to some extent by much weaker absorption below the cloud base.

The radiative transfer methods used here were also validated through comparisons

with the line-by-line multiple scattering results described by Ramaswamy and Freidenreich (1992). They computed the solar flux absorbed by water vapor alone in atmospheres with McClatchey et al. (1972) MLS mixing ratios and a wavelength-independent surface albedo of 0.2. Their models indicated values of 178.1 and 71.4 W m^{-2} at solar zenith angles of 30 and 70°, respectively. The corresponding results obtained from SMART are 189.4 and 73.7 W m^{-2} . The somewhat larger values obtained here appear to be primarily a consequence of differences in the treatment of the far wings of water vapor lines in these two studies. The line-by-line model used by Ramaswamy and Freidenreich assumes that the far wings of water vapor lines have Lorentzian shapes, and ignores contributions by lines at distances more than 10 cm^{-1} from their centers. In contrast, LBLABC assumes a more realistic super-Lorentzian line profile (Clough et al. 1989), and retains line contributions at distances less than 1000 cm^{-1} from the line centers. This line shape produces a weak water vapor continuum that is absent in the Ramaswamy and Freidenreich model. To test the effects of this continuum, absorption lines were arbitrarily truncated at 10 cm^{-1} from the line centers and the atmosphere absorption was recalculated. This reduced the absorption to 182.1 W m^{-2} at $\theta_{\odot}=30^{\circ}$, and 70.9 at $\theta_{\odot}=75^{\circ}$. These values are in remarkable agreement with those obtained by Ramaswamy and Freidenreich (1992).

4.2. Clear Sky Absorption

To more completely assess the effects of clouds and absorbing gases on the Earth's solar radiation budget, the SMART model was used to evaluate the solar forcing for solar zenith angles between 0 and 85 degrees. The clear-sky net solar fluxes and the atmospheric net fluxes are shown as functions of altitude and solar zenith angle in Figures 13 and 14. These fluxes were integrated over solar zenith angle to simulate the effects of globally-averaged illumination conditions (Eq. 9). The nominal model uses the same gas mixing ratios and surface albedos as those used in the validation tests

described above, but a range of alternative water vapor mixing ratio profiles and cloud optical depths were also considered.

The resulting bolometric net flux profiles for global-annual-average illumination conditions are shown in Figure 15. The corresponding net atmospheric solar fluxes are shown figure 16. These simulations show that clear, aerosol-free atmospheres with MLS water vapor mixing ratios over moderately-dark ocean surfaces absorb about 74.5 W m^{-2} . This is somewhat larger than that obtained by the radiative transfer algorithms used in most GCMs (56 to 68 W m^{-2}). This enhanced clear-sky absorption may reflect the use of a much more rigorous treatment of gas absorption by the present model, or it may simply be a consequence of the adoption of the MLS water vapor profile in this simulation. To help discriminate between these possibilities, globally-averaged, clear-sky atmospheric fluxes were derived for the entire range of water vapor profiles shown in Figure 6. The resulting globally averaged net atmospheric absorption ranged from 50.5 W m^{-2} for the McClatchey sub-arctic winter (SAW) profile to $\sim 79 \text{ W m}^{-2}$ for the tropical profile (Figure 15). If water vapor is neglected entirely, the net atmospheric absorption falls to 20.7 W m^{-2} .

Clear atmospheres with mid-latitude winter (MLW) and sub-arctic summer water vapor profiles roughly span the range of atmospheric fluxes derived by GCM radiative transfer algorithms, producing values near 57.5 and 69.1 W m^{-2} . The U.S. Standard Atmosphere, 1976 water vapor profile (cf. Lieu, 1982) was also tested to facilitate comparisons with the results recently published by Kiehl and Trenberth (1997). For that water vapor profile, the present model finds atmospheric fluxes near 64.7 W m^{-2} for clear skies and global-annual average illumination conditions, while Kiehl and Trenberth report a value of 60 W m^{-2} . These water vapor profiles are significantly drier than the global average (GA) profile, which produces net atmospheric fluxes comparable to those obtained for the MLS profile (72.5 vs 74.5 W m^{-2}). The similarity of the MLS and GA profiles suggest that the MLS water vapor profile should provide an acceptable proxy

for the globally averaged water abundance. In addition, the clear-sky results obtained for globally-averaged water vapor amounts are very similar to the clear sky atmospheric fluxes derived from the Earth Radiation Budget Experiment (ERBE) and the Global Energy Balance Archive (GEBA) (79.1 W m^{-2} ; Li et al. (1995;1996; 1997)). To the extent that this comparison is valid, the present model accounts for 5 to 18 W m^{-2} of the 25 to 40 W m^{-2} that is usually missed by the radiative transfer algorithms used in existing GCMs.

4.3. The Effects of Low, Middle, and High Clouds

To determine the effects of low (stratus, cumulus, stratocumulus, nimbostratus, etc.), middle (altostratus), and high (cirrus) clouds on the solar radiation budget, solar fluxes were derived as functions of wavelength and altitude for model atmospheres with a broad range of cloud altitudes, optical depths, and solar illumination angles. Results for each model atmosphere were then integrated over wavelength and zenith angle to yield globally-averaged bolometric fluxes for comparison with the clear-sky results described above. Even though low, middle, and high clouds can enhance the albedo of the surface-atmosphere system, their effects on the column-integrated atmospheric absorption can differ dramatically. These differences have received relatively little attention within the context of the cloud absorption anomaly.

The spectral dependence of the solar fluxes reflected by optically-thick low, middle, and high clouds is shown in Figures 17 and 18. Water vapor is the principal absorber of sunlight in both clear and cloudy atmospheres, but the absorption by this gas is inversely proportional to the cloud top height in atmospheres occupied by optically thick clouds. In particular, the strong water vapor bands at 0.94, 1.1, 1.3, and $1.9 \mu\text{m}$ are more pronounced in the spectrum reflected by the stratocumulus cloud, but they are progressively less prominent in the spectra reflected by middle and high clouds. Two competing processes act to modulate the absorption by water vapor and other absorbers

in cloudy atmospheres. Multiple scattering by cloud particles increases the path lengths traveled by photons, enhancing their probability of absorption. Clouds also reduce the absorption by water vapor and other atmospheric constituents by reflecting a large fraction of the incident solar radiation back to space before it can penetrate to altitudes where it can be effectively absorbed. The results presented here suggest that this “cloud shading” effect dominates for high clouds, while path length enhancements by multiple scattering are more important for low clouds.

The effects of these two processes are described more completely in Figure 19. This figure shows the vertical distribution of fluxes in clear and cloudy atmospheres for global-annual-average illumination conditions. For each cloud type, the vertical divergence of the solar flux is largest at levels within the cloud, indicating strong absorption by cloud particles, water vapor, and other gases. However, the cloud-shading effect decreases the amplitude and the divergence of the flux at levels below the cloud base. These effects are also seen in the solar heating rates, which peak at levels within the cloud, but fall far below the clear-sky values at levels below the cloud (Figure 20). Cloud-level absorption, and cloud shading increase with cloud optical depth.

The net effect of clouds on the column-integrated atmospheric absorption depends on the relative contributions of these two processes. High cirrus clouds produce net reductions in the column-integrated atmospheric absorption because the absorption within these clouds is not large enough to compensate for the cloud shading effects. The absorption within optically-thick middle and low clouds is actually less than that in high clouds, but these clouds shade a much smaller fraction of the atmospheric column. In addition, because the water vapor abundance above low clouds is much larger than that above high clouds, a low cloud can enhance the absorption above the cloud top by reflecting a large fraction of the incident radiation back through this absorbing layer for a second pass. This effect is illustrated in Figure 21, which shows the solar heating rates produced by stratocumulus clouds with a range of optical depths. Even though the top

of this cloud is located near 1.5 km, the absorption of reflected radiation by water vapor at levels above the cloud increases the heating rates at altitudes as high as 5 km.

The effects of low, middle, and high clouds on the atmospheric absorption are summarized in Figure 22. This figure compares the spectrally-integrated absorption in cloudy atmospheres to that obtained for the nominal clear-sky case for global annual-average illumination conditions. When an optically-thick ($\tau_c=60$) stratocumulus cloud is added to the model atmosphere at altitudes between 1 and 1.5 km, the column-integrated flux absorbed by the surface-atmosphere system decreases by almost 191 W m^{-2} . However, even though this optically thick cloud decreases the flux absorbed by the surface by $\sim 203 \text{ W m}^{-2}$, it actually increases the atmospheric absorption by about 12 W m^{-2} relative to the nominal clear sky case. This cloudy atmosphere therefore absorbs about 86.9 W m^{-2} for global-annual-average illumination conditions. Optically-thick altostratus clouds produce comparable reductions in the net solar flux at the top of the atmosphere and at the surface. These clouds therefore have little effect on the column-integrated atmospheric absorption for global-annual-average illumination conditions. Optically-thick cirrus clouds reduce the net fluxes at the top of atmosphere more than they reduce the fluxes absorbed at the surface. For the largest cirrus optical depths considered here ($\tau_c=10$), these clouds reduce the atmospheric absorption by as much as 20 W m^{-2} for global-annual-average illumination conditions. Cirrus clouds therefore cool the atmosphere (as well as the surface) at solar wavelengths, partially offsetting the net atmospheric heating that they contribute at thermal wavelengths.

The zenith angle dependence of the absorption in cloudy atmospheres is shown in Figure 23. These results show that the absorption in atmospheres with middle and low clouds decreases more rapidly with solar zenith angle than that in clear atmospheres. For example, atmospheres with optically-thick ($\tau_c \geq 60$), low-altitude (1 to 1.5 km), saturated clouds can absorb up to 75 W m^{-2} more than clear skies with nominal MLS remixing ratios when the sun is at the zenith ($\theta_\odot=0^\circ$). The difference between the clear

and cloudy sky absorption decreases roughly as $\cos^2 \theta_c$ at $\theta_c \leq 70^\circ$. At the largest solar zenith angles, atmospheres with optically-thick low clouds absorb slightly less than clear atmospheres. This solar zenith angle dependence decreases with decreasing cloud optical depth, but even atmospheres with optically-thin low clouds absorb less than clear atmospheres at the largest solar zenith angles. However, when these results are integrated over the globe, atmospheres with low clouds always absorb more than clear atmospheres (Figure 22). The zenith angle dependence of the absorption in atmospheres with altostratus clouds also exceeds that in clear skies. These clouds can produce a positive atmospheric radiative forcing exceeding 30 W m^{-2} at small solar zenith angles, but they produce a negative radiative forcing for larger solar zenith angles. When integrated over the globe, these clouds produce little net radiative forcing. High clouds in aerosol-free atmospheres produce a negative radiative forcing at all solar zenith angles. However, unlike middle and lower clouds, the amplitude of the negative forcing actually decreases at the largest zenith angles for optically thick high clouds.

This dependence on zenith angle is caused primarily by variations in the relative effectiveness of scattering and absorption by cloud particles and water vapor, respectively. Because water vapor is concentrated at the lowest altitudes, a significant fraction of the incident radiation must penetrate to these levels to be absorbed by this gas. More of this radiation can penetrate to these levels when the solar zenith angles and cloud optical depths are small. At larger solar zenith angles and cloud densities, more of the incident sunlight is reflected back to space by the highly-reflective cloud particles before it can be absorbed by this gas. This solar zenith angle dependence is not as strong for optically-thick high clouds because cloud particle absorption plays a larger role in these clouds.

4.4. Absorption by Water Vapor, Liquid Water, and Water Ice

Because water, vapor, liquid water, and water ice are the principle absorbers of sunlight in both clear and cloudy skies, several sensitivity tests were performed to determine their relative contributions to the column-integrated atmospheric absorption. Figure 15 showed that if water vapor is omitted from cloud-free model atmospheres, the column-integrated atmospheric absorption is reduced by $\sim 54 \text{ W m}^{-2}$ (to values near 20.7 W m^{-2}) for global-annual-average illumination conditions. Stratospheric ozone accounts for about half of the remaining absorption ($\sim 12.5 \text{ W m}^{-2}$), while CO_2 , O_2 , CH_4 , and N_2O account for the rest.

The omission of water vapor in regions with optically-thick ($\tau_c=60$) low and middle clouds reduces the atmospheric absorption by ~ 36 and 19 W m^{-2} , respectively, for global-annual-average illumination conditions (Figure 24). In atmospheres with optically-thick ($\tau_c=10$) high clouds, the omission of water vapor reduces the atmospheric absorption by only 6.4 W m^{-2} for these illumination conditions. The water vapor absorption in cloudy atmospheres is inversely proportional to the cloud optical depth and the cloud top altitude.

Figure 15 shows that even relatively small changes in the water vapor abundance can produce significant changes in the absorption by clear skies. Such changes can also make significant contributions to the absorption in cloudy atmospheres. For example, if the nominal MLS water vapor mixing ratios are assumed within low (stratocumulus) and middle (altostratus) clouds, rather than the saturated values adopted in our nominal model, the atmospheric absorption decreases by values ranging from about 3 W m^{-2} for optically-thin low clouds to values near 1 W m^{-2} for optically-thick low clouds (Figure 22). The absorption by cirrus clouds is somewhat less sensitive to these small differences in the water vapor abundance because this gas contributes much less absorption at the altitudes where these clouds form.

To further discriminate the absorption by cloud particles and water vapor in

cloudy atmospheres, solar fluxes were computed for atmospheres with clouds composed of completely non-absorbing (conservative) particles. Comparisons of reflected solar spectra at the top of the Earth's atmosphere for cases with and without cloud droplet absorption indicate that cloud particles contribute only a few percent to the absorption at ultraviolet and visible wavelengths. However, they absorb more strongly at near-infrared wavelengths between strong water vapor bands (Figures 17 and 18). When cloud absorption is neglected, the bolometric absorption by atmospheres with low clouds remained near 77 W m^{-2} for all cloud optical depths considered here (Figure 25). The cloud liquid water absorption increases with cloud optical depth, but it does not exceed 10 W m^{-2} in the global-annual-average for the range of cloud optical depths considered here when nominal water vapor abundances and cloud refractive indices are assumed. Similar comparisons for middle and high clouds indicate that the absorption by cloud droplets increases with altitude as the water vapor abundances decrease. Figure 25 shows that cloud droplets contribute as much as 15.6 W m^{-2} for altostratus clouds, and as much as 2214 W m^{-2} for cirrus clouds for global-annual-average illumination conditions. The zenith angle dependence of cloud droplet absorption can be inferred from Figure 26, which compares the absorption in atmospheres with high, middle, and low clouds composed of absorbing and non-absorbing (NA) particles. These results indicate that the absorption by cloud droplets in horizontally-infinite, plane-parallel clouds decreases more rapidly with solar zenith angle than the water vapor absorption. This may not be the case in more realistic, 3-dimensional clouds, however.

As the cloud optical depth increases, the absorption by cloud particles increases, but both the intensity of the solar flux and the absorption by water vapor within and below the cloud decreases, partially offsetting the enhanced cloud particle absorption. The effects of low clouds on the vertical distribution of solar radiation can be inferred from the solar heating rates (Eq. 10). Figure 21 shows that the maximum amplitude of the solar heating rates increases with cloud optical depth, but the full width at

half maximum of the heating spike decreases with increasing optical depth, such that the maximum solar flux divergences are confined to the top few hundred meters of optically-thick clouds. The effect of shading beneath the clouds is also apparent here, with the thickest clouds reducing the heating rates to about one tenth of their clear sky values at levels near the surface. Finally, some of the radiation reflected back to space by optically-thick low clouds is absorbed by water vapor above the cloud tops. Most of this enhanced absorption occurs near the cloud tops because the water vapor abundance decreases rapidly with altitude, but decreases in the water vapor absorption coefficients associated with reduced pressure broadening of water vapor lines also contributes to the rapid decay of this absorption with height.

The validation tests presented at the beginning of this section showed that the weak continuum absorption between strong water vapor lines can contribute significantly to the atmospheric absorption of solar radiation. To quantify these effects in clear and cloudy atmospheres, fluxes obtained with the nominal water vapor absorption coefficients were compared to values obtained when the H_2O lines were truncated 10 cm^{-1} from the line centers (e.g. Ramaswamy and Freidenreich, 1992). For clear atmospheres, the omission of continuum absorption reduced the column-integrated atmospheric flux from 74.5 to 72.1 W m^{-2} for global-annual-average illumination conditions. In model atmospheres with optically-thick ($\tau_c=60$) low clouds, the omission of continuum absorption reduces the atmospheric flux by only 2 W m^{-2} to $85\text{ J T}^7\text{ n}^2$ (Figure 27). The errors introduced by the omission of the far-wing continuum in cloudy atmospheres are somewhat smaller than one might expect because a large fraction of the omitted water vapor absorption is replaced by enhanced absorption by cloud liquid water droplets. In addition, even though these spectrally-integrated differences are small, the omission of the far-wing continuum can introduce significant errors at some infrared wavelengths and for some illumination conditions. For example, for $\theta_{\odot}=60^\circ$, the upwelling solar flux can be overestimated by more than $50\text{ W m}^{-2}\mu\text{m}^{-1}$ at

some wavelengths within the wings of the 0.94 and 1.1 μm bands in atmospheres with optically-thick low clouds. The spectral extent of these errors is shown in Figure 28. Figure 29, which shows an expanded view of the reflected spectrum in the vicinity of the 1.1 μm band. These results suggest that even though the spectral extent of these errors is too small to seriously affect bolometric flux or heating rate calculations, they could compromise the accuracy of remote sensing retrievals of water vapor from these bands.

4.5. Enhanced Ozone Absorption in Cloudy Skies

The second most important absorber of sunlight in the Earth's atmosphere is stratospheric ozone. In clear skies with MLS mixing ratios, this gas absorbs about 12.5 W m^{-2} for global-annual-average illumination conditions. Highly reflective tropospheric clouds and bright surfaces can enhance the absorption by the weak ozone Huggins (0.3 μm) and Chappuis (0.6 μm) bands by reflecting a large fraction of the incident sunlight back through the stratosphere for a second pass. This effect was first mentioned by Lieu et al. (1978), and its implications for stratospheric heating rates were explored in greater detail by Crisp (1987) and Olaguer et al. (1992). However, this source of absorption has received little attention in studies of the cloud absorption anomaly. The spectral dependence of ozone absorption in clear and cloudy atmospheres is shown in Figure 30. Because the weak Huggins and Chappuis bands are optically thin, their absorption increases almost linearly with increasing ozone abundance and increasing optical path length. Hence, unlike water vapor and cloud particle absorption, the enhanced ozone absorption is most efficient at large solar and emission zenith angles. The amplitude of the enhanced absorption in cloudy atmospheres can be as large as 3 W m^{-2} in the global-annual average. This is a relatively small contribution to the total solar radiation budget, but it increases the solar heating rates by up to 30% (0.5 K day^{-1}) at pressures near 0.02 bars (Figure 31).

4.6. Aerosol Absorption in Clear and Cloudy Skies

Several recent studies have addressed the effects of aerosols on the Earth's radiation budget (cf. Lieu et al. 1978; Charlson et al. 1992; Penner et al. 1992; 1994). These studies show that the ubiquitous, optically-thin, weakly-absorbing, tropospheric aerosols act to enhance the clear-sky albedo over dark land or ocean surfaces, reducing the effective solar insolation, and producing a net cooling effect. The aerosol radiative forcing in cloudy skies has received much less attention, but a broad range of modeling studies suggests that aerosol particles embedded within clouds will produce only modest changes in their albedos (cf. Twomey 1977; Liou et al. 1978; Stevens and Tsay, 1990; Lubin et al. 1996). However, this long-held belief has recently been challenged by empirical studies of the Earth's solar radiation budget, which appear to show spatial correlations between enhanced aerosol abundances and enhanced atmospheric absorption (e.g. Li et al. 1995; Li and Moreau, 1996; Li et al. 1997). These studies provide strong circumstantial evidence that aerosols may play a significant role in the cloud absorption anomaly, but the exact mechanism for their absorption has not yet been identified.

To quantify the solar radiative forcing by aerosols, radiances, fluxes, and heating rates were derived for clear and cloudy aerosol laden atmospheres. These simulations indicate that weakly-absorbing aerosols like those described in Section 2.4 have opposing effects in clear and cloudy atmospheres. Figure 32 shows that in cloud-free regions with dark (ocean) surfaces, these aerosols enhance the effective albedos at most solar wavelengths, confirming the results of earlier studies (cf. Penner et al. 1994). In cloudy regions, aerosols actually reduce the albedos at most of these wavelengths. Hence, even though aerosols have a net cooling effect in cloud-free regions, they should produce a net warming of the climate system in cloudy regions.

In clear skies, uniformly-mixed aerosols with column-integrated visible optical depths between 0.1 and 0.2 (corresponding to visibilities of 100 and 50 km, respectively) will reduce the spectrally-integrated solar flux deposited in the surface-atmosphere

system by 3.8 to 7.4 W m^{-2} (1.2 to 2.4%) (Figure 33). However, this net flux reduction is not shared equally by the surface and the atmosphere. Figure 34 shows that aerosols increase the atmospheric absorption by 6.0 to 12.3 W m^{-2} (8 to 16%), while reducing the surface absorption by 9.8 to 19.7 W m^{-2} (4.2 to 8.4%), compared to the aerosol-free case. These changes in the vertical distribution of solar energy between the surface and the atmosphere should have a stabilizing influence on the vertical temperature lapse rates.

In regions with optically-thick ($\tau_c=60$) low clouds, the nominal, uniformly-mixed, weakly-absorbing, tropospheric aerosols with column-integrated visible optical depths between 0.1 and 0.2 will reduce the albedo of the earth-atmosphere system at most wavelengths between 0.3 and 2 (Figure 32). For global-annual-average illumination conditions, the surface-atmosphere system absorbs between 125.3 and 134.211 W m^{-2} . The corresponding values of the atmospheric absorption vary from 97.1 and 106.9 W m^{-2} for this range of aerosol optical depths (Figure 35). These values are 10.2 to 201 W m^{-2} larger than those obtained in aerosol-free atmospheres with the same optically-thick low cloud (86.9 W m^{-2}), and 22.6 to 32.4 W m^{-2} larger than those obtained for the nominal, cloud-free, aerosol-free atmosphere (74.52 W m^{-2}). Aerosols with the alternate Toon-Pollack aerosol distribution (Figures 1 and 3) and this range of optical depths produce comparable, but somewhat smaller enhancements in the atmospheric absorption (Figure 37). In contrast, these aerosol distributions reduce the spectrally-integrated solar insolation at the surface by only 2 to 3 W m^{-2} when compared to the aerosol-free case with the same optically-thick low cloud.

For optically-thick clouds, most of the aerosol absorption occurs at levels above the cloud tops, and not within the clouds themselves (Figure 38). Weakly-absorbing background and boundary layer aerosols with optical depths like those considered here have little or no effect on the albedo of these clouds, as previous studies have concluded. For low and middle clouds, the amplitude of the aerosol-induced absorption increases

slightly as the optical depth and albedo of the underlying clouds increases. because thicker, brighter clouds reflect a greater fraction of the incident sunlight back through the aerosol layer (Figure 39). Because of this, increased cloud albedos associated with aerosol-related enhancements in the cloud particle number densities (cf. Twomey, 1977; Hobbs, 1993; Penner et al. 1994) might actually increase, rather than decrease the solar radiative forcing by optically thick low and middle clouds in aerosol-laden atmospheres.

The results presented in Figure 39 also show that the absorption by uniformly mixed tropospheric aerosols in atmospheres occupied by optically-thick clouds is inversely proportional to the cloud top height. This is simply a consequence of the fact that the fraction of a uniformly-mixed aerosol column that extends above the cloud tops decreases as the cloud top approaches the tropopause. For an aerosol layer with a constant number density, about 80% of the aerosol column extends above the top of the nominal low cloud, while ~60% of this aerosol column extends over the middle cloud top and less than 10% of this column extends above the top of the high cloud. If the aerosol concentrations decrease with increasing altitude (as they usually do), the aerosol absorption would be even weaker in regions occupied by optically-thick high clouds. These conclusions are consistent with those derived by Lubin et al. (1996), who found that aerosol absorption is not particularly effective in atmospheres with vertically-extended tropical clouds or their extended, high-altitude anvils. However, the results presented in Figure 39 also suggest that those conclusions can not be generalized to the vast majority of clouds, which have tops below 5 ktn.

Figures 36 and 39 show that aerosols can increase the absorption of solar radiation even in atmospheres occupied by optically-thin ($\tau_c < 1$) clouds. These enhancements result because aerosols can have a much larger effect on the net albedo of thin clouds. In addition, multiple scattering of sunlight by optically-thin clouds increases the photon path lengths above, within, and below the cloud, enhancing the probability of absorption

by the aerosols. The vertical distribution of the solar energy absorbed by the aerosols in atmospheres with optically-thin clouds can be inferred from Figure 40, which shows the fluxes and heating rate profiles in cloudy atmospheres with and without aerosols. For optically-thin high clouds, weakly-absorbing aerosols contribute primarily to the flux divergence within and below the cloud deck. For optically-thin low clouds, the majority of the aerosol absorption still occurs above the cloud top. Aerosols contribute comparable amounts of absorption above, within, and below optically-thin altostratus decks.

These experiments indicate that the amplitude of the aerosol absorption in cloudy atmospheres should be a strong function of both the incident solar zenith angle and the emission angle of the radiation reflected by the clouds. The emission angle dependence of the enhanced absorption in aerosol-laden clear and cloudy atmospheres is illustrated in Figures 41 and 42. Clouds scatter the incident solar radiation into a wide range of emission zenith angles. The sunlight that is scattered into the largest zenith angles traverses the longest optical paths through the overlying aerosol layer and is absorbed most efficiently. Because realistic, spatially-varying clouds reflect a greater fraction of the incident sunlight into large emission zenith angles than the plain-parallel clouds used here, these calculations may underestimate the absorption by aerosols above the tops of such clouds.

In addition, unlike absorbers embedded within the clouds, the aerosols distributed above the cloud tops can also produce significant cloud radiative forcing ratios for large solar zenith angles, because the optical paths for both the incoming direct and outgoing scattered components of the solar radiation field are maximized when the sun is near the horizon. The solar zenith angle dependence of the enhanced aerosol absorption is illustrated in Figure 39. The aerosol absorption is strongest when the sun is near the zenith, but aerosols produce significant enhancements in the absorption even at the largest solar zenith angles considered here. With the relatively-thin ($\tau_a=0.1$) aerosol

layer used in this example. low clouds produce a positive radiative forcing at all solar zenith angles. This thin aerosol layer also produces a net positive solar forcing for altostratus clouds at all but the largest solar zenith angles ($>70^\circ$), such that these clouds have a net warming effect on the atmosphere for global-annual-average illumination conditions (Figure 43). Only optically-thick cirrus clouds produce a significant negative forcing for global-annual-average illumination conditions in aerosol-laden atmospheres (Figure 44).

4.7. Effects of Overlapping Clouds in Aerosol-Laden Atmospheres

The cloudy atmospheres described above included a single cloud layer. A significant (but poorly-constrained) fraction of the Earth's surface is covered by multiple, overlapping cloud layers. To estimate the absorption of sunlight in these conditions, aerosol-free and aerosol-laden model atmospheres were created with overlapping middle (AS) and low (SC) clouds or overlapping high (Cir) and low (SC) clouds. In each case, the low cloud was assumed to have a visible optical depth of 10. The middle cloud had an optical depth of either 1 or 10, while the high cloud had an optical depth of 0.1 or 1.0. Uniformly-mixed aerosols with column-integrated optical depths of 0.1 and 0.2 were included in the aerosol-laden cases. The column-integrated results for global-annual-average illumination conditions are presented in Table 3. The altitude-dependent fluxes and heating rates are shown in Figures 45 and 46.

The amplitude of the absorption in atmospheres with overlapping clouds was very sensitive to the optical thickness of the upper cloud layer. In aerosol-free atmospheres with relatively-thick upper clouds, the absorption was generally intermediate between the values obtained for the upper cloud or lower cloud alone. For example, an atmosphere with overlapping, optically-thick ($\tau_c = 10$) AS and SC clouds absorbs 77.7 W m^{-2} in the global-annual-average, while the same atmosphere with an isolated $\tau_c = 10$ AS cloud absorbs 72.46 W m^{-2} , and an atmosphere with an isolated $\tau_c = 10$ SC cloud

absorbs 81.9 W m^{-2} . Similarly, an aerosol-free atmosphere with a “cloud sandwich” consisting of $\tau_c=1$ Cirrus cloud and a $\tau_c=10$ SC cloud absorbs 68 W m^{-2} , while a same atmosphere with an isolated $\tau_c=1$ Cirrus cloud absorbs only 61 W m^{-2} .

This behavior is also seen in cases that include overlapping clouds along with an optically-thin ($\tau_a=0.1$), uniformly-mixed aerosol layer, but the absorption increases by 7 to 9 W m^{-2} compared to the aerosol-free case. If the column-integrated aerosol optical depth is increased to $\tau_a=0.2$, the cloud sandwich consisting of optically-thick ($\tau_c=10$) SC and AS clouds absorbs 7 W m^{-2} more than the SC cloud alone, and almost 19 W m^{-2} more than the AS cloud alone. Most of the added absorption occurs above the top of the AS deck (whose albedo exceeds that of an isolated $\tau_c=10$ AS deck), but some solar flux is absorbed in the region between the 2 cloud layers where photons are trapped by multiple scattering (Figures 45 and 46).

If the upper cloud is relatively thin ($\tau_c=1$ AS, or $\tau_c=0.1$ Cir), cloud sandwiches in aerosol-laden atmospheres absorb much more solar radiation than atmospheres with either cloud layer alone. For example, atmospheres with overlapping $\tau_c=1$ AS and $\tau_c=10$ SC clouds absorb 84.5, 93.3, and 113.3 W m^{-2} for column-integrated aerosol optical depths of 0.0, 0.1, and 0.2, respectively. Similarly, atmospheres with overlapping $\tau_c=0.1$ Cir and $\tau_c=10$ SC clouds absorb 79, 88, and 107 W m^{-2} for this range of aerosol optical depths. Unlike the cases with optically-thick high clouds, the majority of the radiation is absorbed in the cavity between the two cloud layers (Figures 45 and 46). Even very thin upper clouds can efficiently trap radiation in this cavity, where it can bounce back and forth until it is absorbed by gases, aerosols, or cloud droplets. The largest absorption enhancements occur for small solar zenith angles, where a large fraction of the incident sunlight can penetrate the optically-thin upper cloud. It then traverses the cavity and strikes the optically-thick lower cloud, which scatters most of it back upward into a wide range of emission zenith angles. The radiation that is scattered into the largest emission zenith angles traverses a long path through the cavity. This radiation

then strikes the upper cloud at an oblique angle, and encounters a much larger effective backscattering optical depth than it encountered on the way into the atmosphere. A large fraction of this radiation is therefore reflected back into the cavity for another pass, and this process repeats until much of the trapped radiation is absorbed. In any case, the very large solar forcings associated with these overlapping cloud systems emphasize the need to accurately detect and map thin high clouds over optically-thick low clouds on a global scale. This is beyond the capability of most existing or planned remote sensing instruments.

4.8. Effects of High Surface Albedos on the Atmospheric Absorption

The results presented above indicate that a significant fraction of the solar radiation reflected by optically-thick clouds can be absorbed at levels above the cloud tops by water vapor, ozone, and aerosols. The absorption of backscattered sunlight should also enhance the atmospheric absorption over regions with high surface albedos. To test this hypothesis, radiances, fluxes, and heating rates were derived for the alternate “desert” and “(snow)” surface albedo spectra shown in Figure 8. The effects of these increased surface albedos on the spectrally-dependent reflected solar fluxes above cloud-free atmospheres are shown in Figure 47. The upward fluxes for the desert surface are comparable to those for the nominal ocean surface at short wavelengths where the desert albedos are relatively low, but much larger at wavelengths longer than $0.5\mu\text{m}$, where the desert albedos are substantially greater than the ocean values. Weakly-absorbing aerosols decrease the reflected fluxes above bright, snow-covered surfaces at most visible wavelengths, but increase the reflected fluxes at near infrared wavelengths where the albedo of this surface is relatively low.

When the results in Figure 47 are integrated over wavelength and over a global-annual-average distribution of solar zenith angles, aerosol-free, clear atmospheres over desert and snow-covered surfaces absorb 78.4 and 88.5 W m^{-2} , respectively. For

comparison, a cloud-free atmosphere over the nominal ocean surface absorbed 74.5 W m^{-2} . The corresponding solar fluxes absorbed by the ocean, desert, and snow-covered surfaces are 233.3, 190.0, and 46.8 W m^{-2} . Combining these surface and atmosphere results, the system-integrated absorption for these three surface types are 307.8, 268.3, and 135.3 W m^{-2} . These results show that even though surface albedo increases produce a net decrease in the total solar energy absorbed by the system, they can significantly increase the atmospheric absorption.

Figure 48 summarizes the absorption by cloud-free atmospheres as a function of surface albedo and aerosol abundance. If uniformly-mixed aerosols with column-integrated optical depths near 0.1 are added to the atmospheres with desert and snow-covered surfaces, the atmospheric absorption increases to 85 and 97 W m^{-2} . The amplitude of the atmospheric absorption enhancements over bright, snow-covered surfaces are comparable to those seen for low cloud layers. However, even more modest albedos, like those seen over many land surfaces, are sufficient to increase the atmospheric absorption by several W m^{-2} , when compared to the nominal ocean case.

Surface albedos have their largest effects on the atmospheric absorption for cloud-free conditions, but high surface albedos can also contribute to the absorption in cloudy atmospheres. Figure 49 shows the atmospheric absorption as a function of cloud optical depth for ocean and desert surfaces and column-integrated aerosol optical depths near 0.1. For small cloud optical depths, multiple reflections between highly-reflective surfaces and the cloud deck increase the effective photon path lengths and the efficiency of the water vapor, aerosol, and liquid water absorption. Substantial increases in the atmospheric absorption are therefore predicted for these conditions. These results emphasize the need to accurately determine the spatial extent and optical depths of thin clouds over bright surfaces.

5. Implications for the Global-Average Solar Budget

The calculations presented above show that atmospheres occupied by low clouds (with and without overlapping middle and high clouds), and regions with high surface albedos will usually absorb more solar radiation than otherwise comparable clear atmospheres over dark surfaces. However, these results also show that aerosol-free atmospheres occupied by altostratus clouds absorb about as much sunlight as clear atmospheres, while atmospheres with optically thick high clouds (or, by analogy, vertically-extended clouds) almost, always absorb much less than otherwise comparable clear atmospheres. Water vapor, ozone, and weakly-absorbing aerosols can contribute significantly to the atmospheric absorption, but their global effects depend strongly on their meridional and vertical distributions. These results suggest that a comprehensive, global modeling effort that accurately accounts for the spatial distribution and optical properties of clouds, aerosols, water vapor, and ozone is needed to quantify their effects on the global climate system. Those objectives are well beyond the scope of the present mechanistic study, but a few back-of-the-envelope calculations were performed to further motivate such an investigation.

In these calculations, non-overlapping high, middle, and low clouds were each assumed to cover about 12% of the globe in the global-annual-average. Overlapping high and low clouds, and overlapping middle and low clouds were each assumed to cover 8% of the Earth. The total cloud cover was therefore 52%. These values are roughly consistent with the lower bounds on cloudiness derived by the Nimbus 7 (cf. Stowe et al. 1989) and the ISCCP projects (Rossow and Lacis, 1990). The middle and lower clouds were assumed to have global-average optical depths near 10, while upper cloud optical depths were set to 3 (cf. Rossow and Lacis, 1990). Dark (ocean) surface albedos were assumed to cover ~80% of the surface for the cloud-free regions, while the somewhat brighter desert albedos were adopted for the remaining 20%. For simplicity, ocean albedos were adopted for all cloudy cases.

With these assumptions, the modeling results for the nominal aerosol-free atmospheres presented above yield globally-averaged atmospheric fluxes near 74.8 W m^{-2} , and albedos near 0.31. These all-sky fluxes are almost identical to those obtained for clear, aerosol-free skies (74.5 W m^{-2}), indicating a cloud forcing ratio near unity. If an optically-thin ($\tau_a=0.1$) layer of weakly-absorbing aerosols is added to these atmospheres, the globally-averaged all-sky atmospheric fluxes increase to about 81.4 W m^{-2} , while the system albedos remain near 0.31. The derived all-sky fluxes are virtually identical to the clear-sky fluxes in aerosol-laden atmospheres (80.5 W m^{-2}). If the aerosol optical depths are increased to 0.2, the the globally-averaged all-sky flux increases to 90 W m^{-2} , and the system albedo decreases to 0.304. The corresponding clear-sky flux is 86.7 W m^{-2} .

The clear-sky and all-sky atmospheric fluxes and albedos for these aerosol-laden atmospheres are remarkably similar to the values inferred from the ERBE and GEBA data sets. Specifically, Li et al. (1997) find globally-averaged, clear-sky and all-sky atmospheric fluxes of 79.1 and 83 W m^{-2} , and globally-averaged albedos near 0.296. However, this agreement may be somewhat fortuitous, considering the coarseness of the estimates of the cloud properties, and the total disregard for the effects spatial correlations in the solar forcing and the absorber distributions (ie. more high clouds and aerosols in the tropics, less in the sub-tropics, etc.).

It is also interesting to note that even though the globally-averaged clear sky albedo increases from 12% to 13.5% as the aerosol optical depth increases from 0 to 0.2, the system albedo actually decreases from 31.1% to 30.4%. In other words, the weakly-absorbing aerosols used in this investigation produce albedo decreases in cloudy regions (which occupy 52% of the Earth in this example) that are as large or larger than the albedo increases that they produce in cloud-free regions. This result directly contradicts the conclusions of many recent studies of the effects of aerosols on the climate system. This effect was apparently missed in those studies because they focused

on the effects of completely conservative aerosols (cf. Kiehl and Briegleb), or simply ignored the effects of aerosols in cloudy regions (cf. Chylek and Wong, 1995).

In many recent empirical studies of the cloud absorption anomaly, the net effects of clouds have been described in terms of the shortwave cloud forcing at the surface, C_s , and at the top of the atmosphere, C_t (cf. Cess et al. 1995; Li and Moreau, 1996). These quantities are derived by subtracting the net downward solar fluxes for otherwise similar all-sky (*all*) and clear (*clr*) columns:

$$C_s = F_{all}^n(z_0) - F_{clr}^n(z_0) \quad (14)$$

$$C_t = F_{all}^n(z = \infty) - F_{clr}^n(z = \infty) \quad (15)$$

Because clouds reduce the solar radiation absorbed by the surface-atmosphere system, both C_s and C_t are negative. Given these quantities, the solar forcing by clouds is often expressed in terms of the ratio of the cloud radiative forcings at the surface and at the top of the atmosphere,

$$R = \frac{C_s}{C_t}. \quad (16)$$

The quantity, R , has gained popularity in empirical studies of the Earth's radiation budget because it provides a convenient non-dimensional measure of the absorption by the entire atmospheric column. If the clear and cloudy atmospheres absorb identical amounts of radiation, $R = 1$, while larger and smaller values indicate that the cloudy atmosphere absorbs more or less radiation than the clear atmosphere.

Even though the present model appears to account for much more of the observed atmospheric solar radiation budget than the radiative transfer algorithms currently used in GCMs, it predicts comparable amounts of absorption in clear-sky and all-sky conditions. In other words, it accounts for the amplitude of the observed atmospheric absorption with values of R near unity. The relatively large estimates of the clear-sky

absorption, and associated low values of R predicted here are completely consistent with some recent empirical studies (Li et al. 1995; 1997; Li and Moreau, 1996). They also support the conclusions of Imre et al. (1996), by showing that the large values of R derived in other recent empirical studies may be due to underestimates in of the clear sky absorption rather than enhanced absorption in cloudy skies. Imre et al. show that the “upper envelope method” used to identify clear skies in those studies tends to isolate the clearest of clear skies, rather than the average clear sky conditions. To produce globally-averaged clear-sky absorption values as low as 54 W m^{-2} with the present, model, such that $R \sim 1.5$, absorbing aerosols would have to be eliminated, and the water vapor abundances would have to be reduced by about a factor of 4. Such dry, aerosol-free conditions are often seen in clear regions associated with deep downdrafts, but it is unlikely that they provide a complete or accurate globally-averaged description of clear atmospheres.

6. Conclusions

The rigorous, spectrum-resolving, multiple scattering calculations presented here indicate that the absorption by realistic amounts of water vapor, ozone, weakly-absorbing aerosols, and cloud droplets should be adequate to explain the observed solar radiation budget. No mystery absorbers or missing physics are required. These calculations also provide a more detailed mechanistic description of the role of aerosols in the climate system, and provide new insight into the vertical distribution of solar radiation in the troposphere and stratosphere. In particular, they show that in cloudy atmospheres, or regions with high surface albedos, small amounts of weakly absorbing aerosols can produce a positive solar radiative forcing that can equal or exceed the negative forcing that they produce in clear-skies over dark surfaces. Even though only low and moderate amounts of weakly-absorbing aerosols were considered here, these results suggest that more abundant or more strongly absorbing aerosols, like those associated

with heavily-polluted areas, or regions with active biomass burning, would produce even larger effects than those described here. Spatial and temporal variations in the abundances of these aerosols could easily account for the range of solar forcing ratios represented in the available data sets (cf. Li et al. 1995; Li and Moreau, 1996). In addition, because the present model shows that more sunlight is absorbed in the middle and upper troposphere, and less is absorbed at the surface than most existing GCMs predict, these results could have important consequences for our understanding of the vertical transport, of latent and sensible heat, water vapor, and momentum by general circulation (cf. Sherwood et al. 1994).

It is interesting to note that even though none of the absorbers, absorption mechanisms, or modeling methods presented here are entirely new, these particular factors have received surprisingly little attention in the context of the cloud absorption anomaly. Spectrum-resolving (line-by-line) multiple scattering models like those used here are still too computationally expensive for routine use in GCMs, but they have been available for almost a decade, and have been widely used for simple mechanistic studies like the one presented here (cf. Ramaswamy and Freidenreich, 1991). The rigorous methods used to model water vapor absorption (including the origin and physical mechanisms for continuum absorption) have also been around for at least a decade (cf. Clough et al. 1989). Furthermore, intercomparisons of line-by-line models with the simplified radiative transfer algorithms used in GCMs have clearly shown that the highly parametrized GCM methods often seriously underestimate the absorption by water vapor in clear and cloudy skies (Fouquart et al., 1991). Enhanced absorption by stratospheric ozone in cloudy atmospheres was first described by Crisp (1987) and Olaguer et al. (1992). Even the potential role of aerosols in the cloud absorption anomaly was recently proposed by Li et al. (1995). The specific mechanism for that absorption (ie. the absorption of reflected radiation by aerosols above the cloud tops) was not identified there, but this mechanism can be inferred from results published by

Liou et al. (1978). Differences in the radiative effects of weakly-absorbing aerosols over dark and bright surfaces were mentioned by Wang and Domoto (1974) two decades ago, and numerous times since then (cf. Tegen et al. 1996). Other radiative processes that were not included in this investigation, like those associated with the three-dimensional structure of clouds, almost certainly contribute to the absorption of solar radiation in the Earth's atmosphere, but even those mechanisms have been characterized (cf. Cahalan et al. 1994).

With this arsenal of resources at their disposal, one might wonder how the climate modeling community has overlooked up to 10% of the Earth's solar radiation budget, and up to 30% of the atmospheric solar radiation budget for the past 4 decades. There are several plausible explanations for this oversight. First, it can be argued that even though the cloud absorption anomaly was first identified in the mid 1950's, it is only recently that the accuracy and spatial coverage of the observations have been adequate to establish its existence beyond a shadow of a doubt. Several investigators deserve credit for bringing this problem to the attention of the community (Cess, Li, Ramanathan, Stevens, Wiscombe, and others).

Second, the present investigation indicates that no single mystery absorber or missing physical process is responsible for the so-called cloud absorption anomaly. A broad range of different absorbers and radiative processes apparently contribute to the missing absorption, including (i) enhanced water vapor line and continuum absorption in clear and cloudy skies, (ii) enhanced water vapor absorption within and below saturated clouds, (iii) enhanced ozone absorption above the tops of high-albedo clouds, (iv) enhanced aerosol absorption in clear and cloudy atmospheres, and (v) enhanced atmospheric H_2O , O_3 , and aerosol absorption above bright surfaces. This list is almost certainly not complete. For example, if more realistic, three-dimensional clouds scatter a larger fraction of the incident sunlight into quasi-horizontal paths, more of this radiation could then be absorbed by water vapor, ozone, aerosols, and other weakly-absorbing

atmospheric constituents.

Third, even though the radiative effects of aerosols has received a great deal of recent attention by the climate modeling community, their potential contributions to the cloud absorption anomaly have been largely overlooked. There are several reasons for this. For example, the recent intense focus on anthropogenically-produced sulfate aerosols has apparently led many members of the climate modeling community to conclude that “At visible wavelengths, all constituents of tropospheric aerosols with the exception of elemental carbon are non absorbing” (Harshvardhan, 1993). This is clearly not the case. In fact, the available aerosol literature shows that most tropospheric aerosol particles (with the exception of pristine sulfate aerosols) are at least weakly absorbing at some solar wavelengths (Toon and Pollack, 1976; d’Almeida et al. 1991; Jaenicke, 1993). In addition, until recently, the radiative forcing by optically-thin, weakly-absorbing aerosols seemed insignificant, when compared to the uncertainties in the forcing by other absorbing constituents (e.g. water vapor, clouds). Finally, even though the radiative properties of clouds and aerosols have been studied separately for decades, their combined effects have received much less attention. In most such studies, the aerosols have been included as conservative scatterers (cf. Kiehl and Briegleb, 1993; Chuang et al. 1997), embedded in cloud particles (Stevens and Tsay, 1992), or completely ignored in cloudy atmospheres (Chýlek and Wong, 1995). Within this context, the relatively strong absorption by optically-thin, weakly-absorbing aerosols above the cloud tops is somewhat surprising (if not insidious).

Fourth, even the best available observations provide inadequate spatial, spectral, and angular coverage and resolution to facilitate the diagnosis of problems at the 10 to 30%, level. In particular, cloud radiative forcing ratios derived from observations taken from orbit and at the surface provide no meaningful constraints on the vertical distribution of candidate anomalous absorbers. Because of this, investigators have focused much of their attention on absorbers embedded within clouds, rather than

those located above the cloud tops (which the present study shows may play a much larger role than anticipated). Routine in-situ measurements of net solar flux profiles are needed to accurately detect and quantify the vertical distribution of absorbers as a function of space and time. In addition, even though state-of-the-art, research-grade, broad-band radiometers provide adequate constraints on the bolometric fluxes, their measurements can not discriminate UV, visible, and NIR absorbers. These instruments also produce no information about the angular distribution of the scattered radiation. The results presented here suggest that such information would have been particularly valuable for identifying those absorbers distributed above the cloud tops.

In closing, it is important to reiterate that even though this mechanistic modeling study employs plausible globally-averaged model atmospheres and surfaces, it does not explicitly account for spatial correlations between absorbers that contribute to the absorption of sunlight. To do this, a much more comprehensive, spatially-resolved, global investigation is needed. The input data needed includes spatially and temporally-correlated observations of pressure, temperature, water vapor and ozone mixing ratios, cloud cover, cloud optical depth, and aerosol optical depths as functions of latitude and altitude. In addition, a complete, spectrally-dependent description of the surface albedos and aerosol optical properties is needed. Any of these quantities that is not explicitly measured must be supplied from climatological estimates, or simply guessed, introducing uncertainties into the investigation. To validate these modeling results, the data collected by broad-band, all-sky radiometers must be supplemented by spatially and spectrally-resolved observations that can discriminate the vertical, angular, and spectral distribution of fluxes. This array of measurements is beyond the scope of existing observational systems, but it may be possible to address most of these needs during the next decade, as NASA deploys its Earth Observing System (EOS) satellites, and other agencies (DOE and NOAA) augment their ground-based and aircraft based observing systems.

6.1. Acknowledgments

This project started as an effort to validate a series of radiative transfer modeling tools that were developed for studies of the atmospheres of Venus and Mars. I greatly acknowledge the patience and generous support from the NASA Planetary Atmospheres Program and the encouragement of my NASA sponsors (J. Bergstralh and W. Huntress) to complete this exercise in comparative planetology. This project would have been severely delayed without the development of the DISORT algorithm by Knut Stamnes and his colleagues, and its distribution by Warren Wiscombe. This work is dedicated to the memory of the late Dr. Stephen B. Fels. This research was conducted at the Jet Propulsion Laboratory/California Institute of Technology.

References

- Ackerman, A. S., and O.B.Toon, 1996: Unrealistic desiccation of marine stratocumulus clouds by enhanced solar radiation, *Nature*, *380*, 512-515.
- d'Almeida, G. A., P. Koepke, and E.P.Shettle, 1991, Atmospheric Aerosols, Global Climatology and Radiative Characteristics, A. Deepak Publishing, Hampton Virginia, 561pp.
- Anderson, B. E., W. B. Grant, G. L. Gregory, E. V.Browell, J. E. Collins Jr., G.W.Sachse, D. R.Bagwell, C. H. Hudgins, D. R. Blake, and N. J. Blake, 1996, Aerosols from biomass burning over the tropical South Atlantic Region: Distribution and impacts, *J. Geophys. Res.*, *101*, 24117-24137.
- Arking, A., 1996: Absorption of solar energy in the atmosphere: Discrepancy between model and observations, *Science*, *273*, 779-782.
- R. F., W.Ridgeway, W.J. Wiscombe, T. L. Bell, and J. B. Snider, 1994: The albedo of fractal stratocumulus clouds, *J. Atmos.Sci.*, *51*, 2434-2455.
- Cess, R. D., M. H. Zhang, P. Minnis, L. Corsetti, E. G. Dutton, B. W. Forgan, D. P. Garber, W. L. Gates, J. J. Hack, E. F. Harrison, X. Jing, J. T. Kiehl, C. N. Long, J.-J. Morcrette, G. L. Potter, V. Ramanathan, B. Subasilar, C. H. Whitlock, d. F.Young, and Y.Zhou, 1995: Absorption of solar radiation by clouds: observations versus models, *Science*, *267*, 496-499.
- Charlock, T. P., and T. L. Alberta, 1996: The CERES/ARM/GEWEX Experiment (CAGEX) for the retrieval of radiative fluxes with satellite data. *Bull. Amer. Meteor. Soc.*, *77*, 2673-2683.
- Chou, M. D., A. Arking, J. Otterman, and W.L. Ridgeway, 1995: The effect of clouds on atmospheric absorption of solar radiation, *Geophys. Res. Lett.*, *22*, 1885-1888.
- Chýlek, P. and J. Wong, 1995, Effect of absorbing aerosols on global radiation budget. *Geophys. Res. Lett.*, *22*, 929-931.
- Chýlek, P., C. M. Banic, B. Johnson, P. A. Damiano, G. A. Isaac, W. R. Leaitch,

- P. S. K. Liu, F. S. Boudala, B. Winter, and D. Ngo, 1996: Black Carbon: Atmospheric concentrations and cloud water content measurements over Nova Scotia, *J. Geophys. Res.*, *101*, 29105-29110.
- Chuang, C. C., J. E. Penner, K. E. Taylor, A. S. Grossman, and J. J. Walton, 1997: An assessment of radiative effects of anthropogenic sulfate, *J. Geophys. Res.*, *102*, 3761-3778.
- Clarke, A. D., J. N. Porter, F. P. J. Valero, P. Pilewskie, 1996: Vertical profiles, aerosol microphysics, and optical closure during the Atlantic Stratocumulus Transition Experiment: Measured and modeled column optical properties, *J. Geophys. Res.*, *101*, 4443-4453.
- Clough, S. A., F. X. Kneizys, and R. W. Davies, 1989: Line shape and the water vapor continuum, *Atmos. Res.*, *23*, 229-241.
- Crisp, D., 1986: Radiative forcing of the Venus mesosphere. I. Solar fluxes and heating rates, *Icarus*, *67*, 484-514.
- Crisp, D., 1987: The effect of tropospheric clouds on stratospheric net radiative heating rates, *EOS*, *68*, 274.
- Crisp, D., and R. West, 1992: Spectral mapping transformations for broad-band radiances and high-resolution spectra in absorbing, emitting, scattering atmospheres, *International Radiation Symposium*, Tallin, 3-8 August, 1992.
- Crisp, D., 1997: Absorption of sunlight by water vapor in cloudy conditions: A partial explanation for the cloud absorption anomaly, *Geophys. Res. Lett.*, *24*, 571-574.
- DeMore, M., S. Sander, D. Golden, R. Hampson, M. Kurylo, C. Howard, A. Ravishankara, C. Kolb, and M. Molina, 1992: Chemical kinetics and photochemical data for use in stratospheric modeling, *JPL Publication 92-20*, 185pp.
- Dutton, E. G., P. Reddy, S. Ryan, and J. J. DeLuisi, 1994: Features and effects of aerosol optical depth observed at Mauna Loa, Hawaii: 1982-1992, *J. Geophys. Res.*, *99*,

8295-8306.

- Esposito, F., C. Serio, H. Horvath, and F. Romano. 1996. Vertical and horizontal aerosol spectral extinction at a rural location in southern Italy, *J. Geophys. Res.*, *101*, 19285-19292.
- Fels, S. B. and M. D. Schwarzkopf, 1981, .411 efficient, accurate algorithm for calculating CO₂ 15 μ m band cooling rates, *J. Geophys. Res.*, *86*, 1205-1232.
- Fouquart, Y., B. Bonnel, and V. Ramaswamy, 1991. Intercomparing shortwave radiation codes for climate studies. *J. Geophys. Res.*, *96*, 8955-8968.
- Fu, Q., and K.-N. Lieu, 1992: On the correlated k-distribution method for radiative transfer in nonhomogeneous atmospheres, *J. Atmos. Sci.*, *49*, 2139-2156.
- Hansen, J., 1971: Multiple scattering of polarized light in planetary atmospheres. Part II. Sunlight reflected by terrestrial water clouds, *J. Atmos. Sci.*, *28*, 1400-1426.
- Hansen, J., and L. D. Travis, 1974, Light scattering in planetary atmospheres, *Space Sci. Rev.*, *16*, 527-610.
- Harshvardhan, 1993: Aerosol-climate interactions, *Aerosol-Cloud-Climate interactions* ed. P. V. Hobbs, (Academic Press, Inc., San Diego), 76-95.
- Hegg, D. A., P. V. Hobbs, S. Gassó, J. D. Nance, and A. L. Range, 1996, Aerosol measurements in the Arctic relevant to direct and indirect radiative forcing, *J. Geophys. Res.*, 23349-23363.
- Hobbs, P., 1993: Aerosol-cloud interactions, *Aerosol-Cloud-Climate Interactions* ed. P. V. Hobbs, (Academic Press, Inc., San Diego), 33-73.
- Imre, D. G., E. H. Abramson, and P. H. Daum, 1996, Quantifying cloud-induced shortwave absorption: An examination of uncertainties and recent arguments for large excess absorption, *J. Appl. Met.*, *35*, 1991-2010.
- Jaenicke, R. 1993: Tropospheric aerosols, *Aerosol-Cloud-Climate Interactions* ed. P. V. Hobbs, (Academic Press, Inc., San Diego), 1-31.
- Kaufman, Y. J., and B. N. Holben, 1997, Hemispherical backscattering by biomass

- burning and sulfate particles derived from sky measurements. *J. Geophys. Res.*, 102, 19433-19446.
- Kiehl, J. T., J. J. Hack, and B. P. Briegleb, 1994: The simulated Earth radiation budget of the National Center for Atmospheric Research community climate model (CCM2) and comparisons with the Earth Radiation Budget Experiment (ERBE), *J. Geophys. Res.*, 99, 20815-20827.
- Kiehl, J. T. and K. E. Trenberth, 1997, Earth's annual global mean energy budget, *Bull. Am. Met. Soc.*, 78, 197-208.
- Lacis, A. A., and V. Oinas, 1991: A description of the correlated-k-distribution method for modeling nongrey gaseous absorption, thermal emission, and multiple scattering in vertically inhomogeneous atmospheres, *J. Geophys. Res.*, 96, 9027-9063.
- Leiterer, U., M. Weller, and A. Herber, 1992, Global changes of Aerosols - Ground-based monitoring of the optical thickness in polar regions and central Europe. *Ber. Bunsenges. Phys. Chem.* 96, 377-380.
- Li, S.-M., M. Banic, W. R. Leaitch, P. S. K. Liu, G. A. Isaac, X.-L. Zhou, and Y.-N. Lee, 1996: Water-soluble fractions of aerosol and their relations to number size distributions based on aircraft measurements from the North Atlantic Regional Experiment, *J. Geophys. Res.*, 101, 29111-29121.
- Li, Z., H. W. Baker, and L. Moreau, 1995: The variable effect of cloud on atmospheric absorption of solar radiation. *Nature*, 376, 486-490.
- Li, Z. and L. Moreau, 1996: Alteration of atmospheric solar radiation by clouds: Simulation and observation, *J. Appl. Met.*, 35, 653-670.
- Liou, K.-NT., K. P. Freernan, and T. Sasamori, 1978: Cloud and aerosol effects on the solar heating rate of the atmosphere, *Tellus*, 30, 62-70.
- Liousse, C., F. Dulac, H. Cachier, and D. Tanré, 1997, Remote sensing of carbonaceous aerosol production by African savanna biomass burning, *J. Geophys. Res.*, 102,

- 5895-5911.
- Lioussse, C., J. E. Penner, C. Chuang, J. J. Walton, H. Eddleman, and H. Cachier, 1996, .4 global three-dimensional model study of carbonaceous aerosols. *J. Geophys. Res.*, 101, 19411-19432.
- Lubin, D., J.-P. Chen, P. Pilewski, V. Ramanathan, and P. J. Valero, 1996: Microphysical examination of excess cloud absorption in the tropical atmosphere, *J. Geophys. Res.*, 101, 16961-16972.
- McClatchey, R., R. W. Fenn, J. E. A. Selby, F. E. Voltz, and J. S. Garing, 1972: Optical properties of the atmosphere (revised), *Environ. Res. Paper 354*, 110 pp.
- McCartney, E. J., 1976: *Optics of the Atmosphere*, (Wiley, New York), 187-215.
- Meadows, V. S. and D. Crisp, 1996: Ground-Based Near-Infrared Observations of the Venus Night Side, *J. Geophys. Res.*, 101, 4595-4622.
- Muinonen, K., K. Lumme, J. Peltoniemi, and W. M. Irvine-WM, 1989: Light Scattering by randomly-oriented crystals, *Appl. Opt.*, 28, 3044-3050.
- O'Brien, H. W. 1975. Red and near infrared spectral reflectance of snow, *U. S. Army Army Cold Region Research and Engineering Laboratory*, Hanover, NH, CRREL (AD-A007732).
- Olague, E. P., H. Yang, and K. K. Tung, 1992: A reexamination of the radiative balance in the stratosphere, *J. Atmos. Sci.*, 49, 1242-1263.
- Palmer, K. F., and D. Williams, 1975. Optical constants of sulfuric acid: Application to the clouds of Venus? *Appl. Opt.* 14, 208-219.
- Peixoto, J. P., and A. H. Oort, 1992: The climatology of relative humidity in the atmosphere, *J. Climate*, 9, 3443-3463.
- Penner, J. E., R. E. Dickinson, C. A. O'Neil, 1992: Effects of aerosol from biomass burning on the global radiation budget, *Science*, 256, 1432-1434.
- Penner, J. E., R. J. Charlson, J. M. Hales, N. S. Laulainen, R. Leifer, T. Novakov, J. Ogren, L. F. Radke, S. E. Schwartz, and L. Travis, 1994, Quantifying and

- minimizing the uncertainty of climate forcing by anthropogenic aerosols, *Bull. Am. Meteor. Soc.* **75**, 375-400.
- Pilewskie, P. and F. P. J. Valero, 1995: Direct observation of excess solar absorption by clouds, *Science*, **267**, 1626-1629.
- Ramanathan, V., B. Subasilar, G. J. Zhang, W. Conant, R. D. Cess, J. T. Kiehl, H. Grassl, and L. Shi, 1995: Warm pool heat budget and shortwave cloud forcing: A missing physics? *Science*, **267**, 499-503.
- Rossow, W. B., and A. Lacis, 1990, Global, seasonal, cloud variations from satellite radiance measurements. Part II: Cloud properties and radiative effects, *J. Climate*, **3**, 1204-1253.
- Rothman, L., R. Gamache, R. Tipping, C. Rinsland, M. A. Smith, D. Chris Benner, V. Malathy Devi, J.-hf. Flaud, C. Camy-Peyret, .4. Perrin, A. Goldman, S. T. Massie, L. Brown, and R. Toth, 1992: The HITRAN molecular database: Editions of 1991 and 1992, *J. Quant. Spectrosc. Radiat. Transfer*, **48**, 469-507.
- Segelstein, D., 1981: The complex refractive index of water", M.S. Thesis, University of Missouri-Kansas City.
- Sherwood, S. C., V. Ramanathan, T. P. Barnett, M. K. Tyree, and E. Roeckner, 1994: Response of an atmospheric general circulation model to radiative forcing of tropical clouds, *J. Geophys. Res.*, **99**, 20829-20845.
- Smirnov, A., A. Royer, N. T. O'Neill, and A. Tarusov, 1994, A study of the link between synoptic air mass type and atmospheric optical parameters, *J. Geophys. Res.*, **99**, 20967-20982.
- Smirnov, A., N. T. O'Neill, A. Royer, A. Tarusov, and A. McArthur, 1996, Aerosol optical depth over Canada and the link with synoptic air mass types, *J. Geophys. Res.*, **101**, 19299-19318.
- Starnnes, K., S. C. Tsay, W. Wiscombe, and K. Jayaweera, 1988: Numerically stable algorithm for discrete-ordinate-method radiative transfer in multiple scattering

- and emitting layered media. *Appl. Opt.*, 28, 2502-2509.
- Stephens, G. L., and S.-C. Tsay, 1990: On the cloud absorption anomaly, *Q. J. R. M. Soc.* **116**, 671-704.
- Toon, O. B. and J. B. Pollack, 1976: A global average model of atmospheric aerosols for radiative transfer calculations, *J. Appl. Meteorol.* **15**, 225-246.
- Twomey, S. 1977: *Atmospheric Aerosols*, (Elsevier), 289pp.
- Villevalde, Y. V., A. V. Smirnov, N. T. O'Neill, S. P. Smyshlyaev, and V. V. Yakolev, 1994, Measurement of aerosol optical depth in the Pacific Ocean and North Atlantic, *J. Geophys. Res.*, **99**, 20983-20988.
- Warren, S., 1984: Optical constants of ice from the ultraviolet to the microwave, *Appl. Opt.*, **23**, 1206-1225.
- Wehrli, C., 1986: *WCRP Publication Series No. 7, WMO ITD-No. 149*, 119-126.
- Wielicki, B. A., R. D. Cess, M. D. King, D. A. Randall, and E. F. Harrison, 1995: Mission to Planet Earth: Role of Clouds and Radiation in Climate, *Bull. Amer. Meteor. Soc.* **76**, 2125-2153.
- Wild, M., A. Ohmura, H. Gilgen, and E. Roeckner, 1995: Validation of general circulation model radiative fluxes using surface observations, *J. Climate*, **8**, 1309-1324.
- Wild, M., A. Ohmura, H. Gilgen, and E. Roeckner, 1996: Regional climate simulation with a high resolution GCM: surface radiative fluxes, *Climate Dynamics*, **11**, 469-486.
- Wiscombe, W. J., 1980: Improved mie scattering algorithms, *Appl. Opt.*, **19**, 1505-1509.
- Wiscombe, W. J., 1995: Atmospheric physics: An absorbing mystery, *Nature*, **376**, 466-467.
- Young, A. T., 1980: Revised depolarization corrections for atmospheric extinction,

Appl. Opt., 19, 3427-3428.

Table 1. Nominal Aerosol Size Distributions (Jaenicke, 1993):

Distribution	Type	i	n_i	R_i	$\log \sigma_i$	$\bar{r} \text{ (}\mu\text{m)}$	$r_{eff} \text{ (}\mu\text{m)}$	$G \text{ (}\mu\text{m}^2)$
Background		1	129	0.0036	0.645	0.218	3.7	0.431
		2	59.7	0.127	0.253			
		3	0.636	0.259	0.425			
Maritime Boundary Layer		1	133	0.0039	0.657	0.266	4.31	0.913
		2	66.6	0.133	0.210			
		3	3.06	0.290	0.396			

Table 2. Cloud optical depths and altitudes

Cloud Type	Optical Depth Range (at 0.6 μm)	Altitude (km)
cirrus	$0.1 \leq \tau_c \leq 10$	$7.0 \leq z \leq 10$
alto-stratus	$0.3 \leq \tau_c \leq 60$	$3.6 \leq z \leq 4.8$
stratocumulus	$0.3 \leq \tau_c \leq 60$	$1.0 < z < 1.5$

Table 3. Column-integrated fluxes and albedos in atmospheres with overlapping stratocumulus (SC) and altostratus (AS) clouds. τ_c^1 is the optical depth of the 1st cloud layer, τ_c^2 is the optical depth of the 2nd cloud layer, τ_a is the aerosol optical depth, F^n is the column-integrated flux absorbed by the surface and atmosphere, F_s^n is the solar flux absorbed by the surface, F_a^n is the column-integrated flux absorbed by the surface and atmosphere, ΔF_a^n is the difference between the column-integrated flux absorbed by this atmosphere, and that absorbed by an otherwise-equivalent atmosphere with a cloud-free sky, $\Delta F_a^n(0)$ is the difference between the column-integrated flux absorbed by this atmosphere, and that absorbed by the nominal, cloud-free, aerosol-free atmosphere, and Albedo is the albedo.

Cloud ¹	τ_c^1	Cloud ²	τ_c^2	τ_a	F^n W m ⁻²	F_s^n W m ⁻²	F_a^n W m ⁻²	ΔF_a^n W m ⁻²	$\Delta F_a^n(0)$ W m ⁻²	Albedo
Clear				0.00	307.79	233.27	74.52	0.00	0.00	0.096
SC	10			0.00	192.49	110.63	81.86	7.34	7.34	0.435
AS	1			0.00	282.33	206.30	76.03	1.52	1.52	0.171
AS	10			0.00	185.96	113.50	72.46	-2.06	-2.06	0.454
SC	10	AS	1	0.00	186.29	101.75	84.53	10.02	10.02	0.453
SC	10	AS	10	0.00	148.24	70.54	77.70	3.18	3.18	0.565
Clear				0.10	303.97	223.43	80.54	0.00	0.00	0.107
SC	10			0.10	195.49	104.52	90.97	10.43	10.43	0.426
AS	1			0.10	279.90	196.77	83.13	2.58	2.58	0.178
AS	10			0.10	187.21	107.16	80.04	-0.50	-0.50	0.450
SC	10	AS	1	0.10	191.77	98.43	93.34	12.80	12.80	0.437
SC	10	AS	10	0.10	154.37	68.02	86.35	5.81	5.81	0.547

Table 3. (continued)

Cloud ¹	τ_c^1	Cloud ²	τ_c^2	τ_a	F^n	F_s^n	F_a^n	ΔF_a^n	$\Delta F_a^n(0)$	Albedo
					W m^{-2}	W m^{-2}	W m^{-2}	W m^{-2}	W m^{-2}	
SC	10			0.00	192.49	110.63	81.86	7.34	7.34	0.435
Cir	0.1			0.00	288.05	216.73	71.32	-3.20	-3.20	0.154
Cir	1			0.00	197.08	136.06	61.01	-13.50	-13.50	0.421
SC	10	Cir	0.1	0.00	183.48	104.46	79.02	4.50	4.50	0.461
SC	10	Cir	1.0	0.00	147.95	80.14	67.82	-6.70	-6.70	0.566
Clear				0.10	303.97	223.43	80.54	0.00	0.00	0.107
SC	10			0.10	195.49	104.52	90.97	10.43	10.43	0.426
Cir	0.1			0.10	285.75	208.31	77.44	-3.10	-3.10	0.161
Cir	1			0.10	196.70	130.91	65.78	-14.76	-14.76	0.423
SC	10	Cir	0.1	0.10	188.69	100.94	87.75	7.21	7.21	0.446
SC	10	Cir	1.0	0.10	151.82	76.68	75.14	-5.41	-5.41	0.554
Clear				0.20	301.16	214.30	86.86	0.00	0.00	0.116
SC	10			0.20	200.50	101.11	99.39	12.52	12.52	0.411
Cir	0.1			0.20	283.87	199.86	84.01	-2.86	-2.86	0.167
Cir	1			0.20	197.16	126.12	71.04	-15.82	-15.82	0.421
SC	10	Cir	0.1	0.20	201.18	93.82	107.36	20.49	20.49	0.409
SC	10	Cir	1.0	0.20	160.96	69.73	91.22	4.36	4.36	0.527

Figure Captions:

Figure 1. Particle size distributions for the nominal(Jaenicke Background) and alternate (Toon-Pollack Mid-Troposphere) background and boundary layer(Jaenicke Maritime) aerosol distributions adopted in this study.

Figure 2. Wavelength-dependent single scattering optical properties (extinction cross section, σ_e , scattering cross section, σ_s , single scattering albedo, ω_o , and scattering asymmetry parameter, g) for ammonium sulfate, soluble organics, dust, and carbonaceous aerosols with the nominal Jaenicke (1993) background aerosol size distribution.

Figure 3. Wavelength-dependent single scattering optical properties for ammonium sulfate, soluble organics, dust, and carbonaceous aerosols with the alternate Toon-Pollack mid-troposphere size distribution.

Figure 4. Wavelength-dependent single scattering optical properties for ammonium sulfate and sea salt aerosols with the Jaenicke Maritime size distribution.

Figure 5. Volume mixing ratios for H_2O , CO_2 , O_3 , N_2O , CO , and CH_4 for the nominal Mid-Latitude Summer (MLS) atmosphere (McClatchey et al. 1972) are shown as a function of pressure. The Volume mixing ratio of O_2 (not shown here) was 0.21.

Figure 6. Comparison of water vapor mixing ratio profiles, including the Mid-Latitude Summer (MLS), Tropical (Trop), Mid-Latitude Winter (MLW), Sub-Arctic Summer (SAS), and Sub-Arctic Winter (SAW) from McClatchey et al. (1972). A globally-averaged profile (GA) derived from climatological results presented by Peixoto and Oort (1992) is also shown.

Figure 7. The nominal MLS water vapor profile is compared to alternate profiles that are saturated within Stratocumulus (SC), Altostratus (AS) and Cirrus (Cir) cloud decks. The mixing ratios are set to a constant value between the cloud base and the level where they intersect the nominal mixing ratio profile.

Figure 8. Surface albedo spectra for a moderately rough ocean surface, (rms wave

slopes of 15 degrees), a desert surface (adapted from spectra of the planet Mars, which resembles terrestrial deserts at visible and near infrared wavelengths), and a moderately fresh snow-covered surface.

Figure 9. Comparison of upward solar flux spectra above clear and cloudy atmospheres obtained with the DART (solid line) and SMART (clotted line) models. The solar zenith angle is 60° . The visible and near-infrared parts of each spectrum are displayed separately (left and right hand panels) with their wavelength and intensity scales optimized to reveal the most prominent spectra features. Panels (a) and (b) show the reflected fluxes above clear atmospheres with nominal dark ocean surfaces. Panels (c) and (d) show the upward visible and near-infrared fluxes above atmospheres with a single optically-thick ($\tau_c=60$) stratocumulus cloud deck above a dark ocean surface. The results obtained by DART and SMART are virtually indistinguishable for these cases. The largest differences are 2 to 4%, but these differences are both positive and negative, and tend to average out over broad spectral regions.

Figure 10. Comparison of spectrally-integrated (0.125 to $8.3\mu\text{m}$) net solar flux profiles obtained with the DART and SMART models for the clear and cloudy atmospheres described in Figure 9. The differences between these two models never exceeds 2%. The net flux at the top of the atmosphere indicates the total solar energy absorbed by the surface-atmosphere system, while the net flux at the surface indicates the amount of flux absorbed at that level. This column-integrated absorption slightly exceeds that shown here because this plot does not show the flux divergence at mesospheric levels.

Figure 11. Comparison of spectrally-integrated (0.125 to $8.3\mu\text{m}$) atmospheric net flux profiles obtained with SMART and DART for the clear and cloudy atmospheres described in Figure 9. The quantity, F_a^n is derived from the total (surface + atmosphere) net fluxes (Figure 10) by subtracting the net solar flux absorbed at the surface from the net flux absorbed at each atmospheric level. The value of F_a^n at the top of the

atmosphere indicates the total solar flux deposited in the atmospheres. Large flux divergences are seen near the surface ($p = 1$ Bar) where water vapor is the principal absorber of solar radiation. Comparisons of these results with those shown in Figure 10 show that even though the surface-atmosphere system absorbs less solar radiation in cloudy regions, the atmosphere can actually absorb more radiation in these regions.

Figure 12. Solar heating rates obtained by DART and SMART for the model atmospheres and solar illumination conditions described in Figure 9. The differences between the exact (DART) and spectral mapping (SMART) models never exceed 2% at pressures greater than 0.002 Bars. The optically-thick ($\tau_c = 60$) stratocumulus cloud enhances the heating rates at levels near the cloud top, but decreases the heating rates below the cloud base. The stratospheric heating rates are higher for the cloudy case because the weak ozone bands absorb some of the intense solar radiation reflected by the cloud tops.

Figure 13. SMART clear sky net solar fluxes for the nominal MLS atmosphere are shown as a function of pressure and solar zenith angle.

Figure 14. SMART clear sky atmospheric net solar fluxes for the nominal h4LS atmosphere are shown as a function of pressure and solar zenith angle.

Figure 15. SMART clear-sky net fluxes for globally-averaged illumination conditions and the nominal ocean surface albedos are shown for each of the water vapor mixing ratios shown in Figure 6, and for a case with no water vapor (diamonds). The omission of water vapor dramatically reduces the atmospheric absorption, but produces much smaller changes the solar flux absorbed by the surface-atmosphere system, because the radiation not absorbed by the atmosphere is deposited on the surface.

Figure 16. Atmospheric net fluxes as a function of altitude for the range of water vapor mixing ratios described in Figure 15.

Figure 17. Solar flux spectra generated with the SMART model. These spectra show the reflected “fluxes above clear and cloudy atmospheres for a solar zenith angle of

60°. Panels (a) and (b) show solar fluxes reflected by a cloud-free atmosphere above a dark ocean surface. Panels (c) and (d) show the fluxes reflected by an atmosphere that includes a single, optically-thick ($\tau_c=60$) stratocumulus (SC) cloud deck with (solid) and without (dotted) liquid water absorption.

Figure 18. Same as Figure 17 for optically-thick ($\tau_c=60$) altostratus clouds with and without liquid water absorption (panels a and b) and optically-thick ($\tau_c=10$) cirrus clouds with and without water ice absorption (panels c and d).

Figure 19. Net solar fluxes in clear and cloudy atmospheres with nominal MLS water vapor mixing ratios, ocean surface albedos and global-annual-average illumination conditions. (a) Net solar fluxes as a function of pressure in clear and cloudy atmospheres. (b) Atmospheric net solar fluxes for atmospheres with stratocumulus (SC) clouds with a range of optical depths. (c) Atmospheric net solar fluxes for atmospheres with altostratus (AS) clouds with a range of optical depths. (d) Atmospheric net solar fluxes for atmospheres with cirrus (Cir) clouds with a range of optical depths.

Figure 20. Tropospheric heating rates for clear atmospheres and atmospheres with moderately-thick stratocumulus (SC, $\tau_c=10$), altostratus (AS, $\tau_c=10$), and cirrus (Cir, $\tau_c=3$) clouds and global-annual-average illumination conditions.

Figure 21. Tropospheric solar heating rates for a clear atmosphere, and for atmospheres with a single stratocumulus cloud deck with a range of optical depths ($0.3 < \tau_c < 60$). Optically-thin clouds increase the absorption and heating rates at all levels. For optically-thick low clouds, the heating rates near the cloud top increase with the cloud optical depth, but the heating rates below the cloud base decrease with increasing optical depth. The enhanced heating rates above the cloud are produced as some of the upwelling solar radiation that is reflected by the cloud is absorbed by water vapor above the cloud.

Figure 22. Net downward solar fluxes and albedos for cloudy atmospheres over dark (ocean) surfaces with global-annual-average illumination conditions. Each

atmosphere includes a single low (SC), middle (.4 S), or high (Cir) cloud with a range of optical depths (Table 2). Results obtained for the MLS water vapor profile (MLS H₂O) are compared to those obtained when the water vapor mixing ratios are saturated within the cloud layers. (a) Net fluxes at the top of cloudy atmospheres as a function of cloud height and cloud optical depth, τ_c . The net flux at the top of the baseline clear atmosphere is 307.8 W m^{-2} for these illumination conditions. (b) Net fluxes at the surface as a function of cloud height and optical depth. The baseline clear-sky case absorbs 233.3 W m^{-2} at the surface for these illumination conditions. (c) Net solar flux absorbed by the atmosphere for the cloud and water vapor distributions described in panel (a). The baseline clear atmosphere absorbs 74.5 W m^{-2} (thin solid line). (d) Top-of-atmosphere albedos for the cloud and water vapor distributions used in panel (a).

Figure 23. Atmospheric absorption in cloudy skies as a function of solar zenith angle and cloud optical depth. (a) Atmospheric fluxes for saturated low (SC), middle (AS), and high (Cir) clouds when the sun is at the zenith ($\theta_{\odot}=0^\circ$). For these conditions, the nominal clear atmosphere absorbs 255.9 W m^{-2} (thin solid line). (b) Same as (a) for a zenith angle of 30° , where the nominal clear atmosphere absorbs 230.2 W m^{-2} . (c) Same as (a) for a zenith angle of 60° , where the nominal clear atmosphere absorbs 155.5 W m^{-2} . (d) Same as (a) for a zenith angle of 85° , where the nominal clear atmosphere absorbs 44.4 W m^{-2} .

Figure 24. Column-integrated atmospheric absorption by cloudy atmospheres with and without water vapor (No H₂O). The thin, horizontal solid line shows the absorption by the baseline clear atmosphere with MLS gas mixing ratios (74.5 W m^{-2}).

Figure 25. Column-integrated atmospheric absorption by cloudy atmospheres with and without cloud liquid water and ice absorption (No Cld Abs). The thin, horizontal solid line shows the absorption by the baseline clear atmosphere with MLS gas mixing ratios (74.5 W m^{-2}).

Figure 26. Solar zenith angle dependent absorption by the nominal clear atmosphere (thin solid line) and cloudy atmospheres with and without (NA) cloud liquid water or ice absorption. The solar zenith angles are (a) 0° , (b) 0° , (c) 0° , and (d) 85° .

Figure 27. Column-integrated atmospheric absorption by cloudy atmospheres with and without water vapor far-wing continuum absorption for global-annual-average illumination conditions. The absorption by the nominal clear atmosphere is shown by thin solid horizontal line (74.5 W m^{-2}). The atmospheric absorption for stratocumulus (SC), altostratus (AS), and cirrus (Cir) clouds are shown. For the cases without water vapor continuum absorption, the water vapor lines were truncated 10 cm^{-1} from the line centers ($\nu_c(\text{H}_2\text{O})=10\text{cm}^{-1}$).

Figure 28. Differences between the reflected solar fluxes at the top of the atmosphere (Figure 9) and those obtained when the water vapor lines are truncated 10 cm^{-1} from the line centers. The solar zenith angle is 60° , and the spectral resolution is 2 cm^{-1} . Panels (a) and (b) show the top-of-atmosphere flux differences for a clear atmosphere with MLS water vapor mixing ratios. Panels (c) and (d) show the flux differences for an atmosphere with an optically-thick ($\tau_c=60$) stratocumulus cloud.

Figure 29. Reflected solar flux spectra at the top of (a) clear and (b) cloudy atmospheres for models with (solid) and without (dotted) far-wing water vapor continuum absorption. The solar zenith angle is 60° , and the spectral resolution is 2 cm^{-1} . For this band, the omission of far-wing absorption introduces the largest errors in micro-windows near the band center.

Figure 30. Reflected fluxes at the top of (a) clear and (b) cloudy atmospheres are shown with and without stratospheric ozone absorption. The solar zenith angle is 60° . The cloudy atmosphere includes a optically-thick ($\tau_c=60$) stratocumulus cloud deck at altitudes between 1 and 1.5 km. The nominal atmosphere uses the MLS ozone abundances (solid line), while the ozone has been omitted entirely from the “No O_3 ” case (dotted line). The largest differences are seen in the weak Huggins bands near $0.3 \mu\text{m}$,

and the Chappuis bands centered near $0.6 \mu\text{m}$. The flux differences are substantially larger in the cloudy case.

Figure 31. Solar heating rates as a function of pressure for clear and cloudy atmospheres with globally-averaged solar illumination conditions. The cloudy atmospheres include a single stratocumulus cloud deck at altitudes between 1 and 1.5 km with a range of optical thickness ($0.3 < \tau_c < 60$). The largest lower-stratospheric solar heating rates are obtained for the thickest clouds because these clouds reflect a larger fraction of the incident radiation back through the stratosphere for a second pass, where it can be absorbed by the weak Huggins and Chappuis bands.

Figure 32. Computed upward solar flux spectra above clear and cloudy atmospheres for a solar zenith angle of 60° . The aerosol-laden atmospheres (dotted lines) have uniform number densities at tropospheric levels (pressures greater than 0.2 bars), column-integrated aerosol optical depths, $\tau_a(0.5 \mu\text{m}) = 0.15$, and single scattering albedos, $\omega(0.5 \mu\text{m}) \sim 0.9$. The cloud-free cases shown in panels (a) and (b) have nominal MLS gas mixing ratios and surface albedos for a moderately-rough ocean (Figure 8). The cloudy atmospheres in panels (c) and (d) include a single, optically-thick ($\tau_c(0.5 \mu\text{m}) = 60$) stratocumulus (SC) cloud at altitudes between 1 and 1.5 km that is saturated with water vapor. Even though these aerosols enhance the albedos in clear skies over dark surfaces, they decrease the albedos over cloudy regions.

Figure 33. Spectrally-integrated clear-sky net solar fluxes for an aerosol-free atmosphere (solid line) are compared to those obtained for aerosol-laden atmospheres for global-annual-average solar illumination conditions and a relatively-dark ocean surface. The aerosol-laden cases include the nominal, uniformly-mixed Jaenicke Background aerosols (J Bkg) with column-integrated optical depths between 0.1 and 0.2, and solar-averaged single scattering albedos near 0.9. Another case includes a combination of uniformly-mixed Jaenicke Background aerosols ($\tau_a = 0.1$) along with equal amounts of the mostly conservative boundary layer aerosols (J Bkg + BL), which are confined near

the surface (particle scale height, $H < 1$ km). These aerosol distributions are described in greater detail in the text.

Figure 34. Spectrally-integrated clear-sky atmospheric net solar flux profiles for global-annual-average illumination conditions and the range of aerosol loadings described in Figure 33. Even though aerosols reduce the absorption by the surface-atmosphere system in clear skies over dark surfaces, they can increase the absorption by the atmosphere.

Figure 35. The spectrally-integrated, global-annual-average atmospheric net flux profile for the nominal, aerosol-free, clear atmosphere (solid line) is compared to those obtained for aerosol-laden atmospheres that include a single, optically-thick ($\tau_c = 60$) stratocumulus cloud deck and the range of aerosol loadings described in Figure 33. The absorption of the incident and reflected sunlight by optically-thin, weakly-absorbing aerosols above the tops of optically-thick low clouds can produce large enhancements in the atmospheric absorption.

Figure 36. Column-integrated atmospheric absorption for the aerosol-laden atmospheres described in Figure 33 are compared to that of the nominal, cloud-free, aerosol-free atmosphere (solid line at 74.5 W m^{-2}). Each cloudy atmosphere includes a single stratocumulus cloud deck between 1.0 and 1.5 km altitude. The boundary layer aerosols considered here (J Bkg+BL) contribute little to the atmospheric absorption because they have single scattering albedos near unity.

Figure 37. Same as Figure 36 for the somewhat more weakly absorbing Toon-Pollack aerosols.

Figure 38. Solar flux and heating rate profiles for aerosol-free and aerosol-laden atmospheres with optically-thick stratocumulus (SC), altostratus (AS), and cirrus (Cir) clouds. The aerosol-laden atmospheres have uniformly-mixed aerosols with the nominal Jaenicke background aerosol size distribution, and column-integrated optical depths near 0.1 at $0.5 \mu\text{m}$. Global-annual-average illumination conditions are used.

(a) Altitude-dependent atmospheric net solar fluxes for cloudy atmospheres with and without aerosols. (b) Differences between the atmospheric net fluxes for the cloudy cases shown in panel (a) and the nominal, aerosol-free clear atmosphere with MLS gas mixing ratios. Aerosols increase the absorption between the cloud top and the tropopause (~ 12 km), but produce negligible changes at levels within or below the clouds. (c) Solar heating rates for cloudy atmospheres with and without aerosols. (d) Differences between the cloudy-sky solar heating rates shown in panel (c) and those obtained for the nominal, aerosol-free clear atmosphere.

Figure 39. Column-integrated atmospheric absorption for the atmospheres described in Figure 38 are shown as a function of cloud optical depth, τ_c , and solar zenith angle, θ_\odot . Results for the nominal, cloud-free, aerosol-free atmosphere are shown as a thin solid horizontal line. The solar zenith angles are (a) 0° , (b) 30° , (c) 60° , and (d) 85° .

Figure 40. Solar fluxes and heating rates for aerosol-free and aerosol-laden atmospheres with optically-thin stratocumulus (SC), altostratus (.4 S), and cirrus (Cir) clouds. The aerosol-laden atmospheres have uniformly-mixed aerosols with the nominal Jaenicke background aerosol size distribution, and column-integrated optical depths near 0.1 at $0.5\mu\text{m}$. Global-annual-average illumination conditions are used. (a) Altitude-dependent atmospheric net solar fluxes for cloudy atmospheres with and without aerosols. (b) Differences between the atmospheric net fluxes for the cloudy cases shown in panel (a) and the nominal, aerosol-free clear atmosphere with MLS gas mixing ratios. In atmospheres occupied by optically-thin clouds, aerosols can enhance the absorption of sunlight above, within, and below the cloud deck. Also, in aerosol-laden atmospheres, thin cirrus clouds can produce a positive solar radiative forcing, while these clouds produce a strong negative forcing in aerosol-free atmospheres. (c) Solar heating rates for cloudy atmospheres with and without aerosols. (d) Differences between the cloudy-sky solar heating rates shown in panel (c) and those obtained for the nominal,

aerosol-free clear atmosphere.

Figure 41. Reflected radiances at the top of the atmosphere are shown as a function of emission zenith angle for clear and cloudy atmospheres with and without aerosols. The sun is at the zenith and the nominal dark ocean albedos are used for all cases shown here. The aerosol-laden atmospheres have uniformly-mixed aerosols with the nominal Jaenicke background aerosol size distribution, and column-integrated optical depths near 0.15 at $0.5\mu\text{m}$. (a) in cloud-free skies over dark surfaces with the sun at the zenith, Rayleigh scattering enhances the reflected radiances at the larger emission zenith angles. For these conditions, aerosols produce modest increases in the reflected radiances at emission zenith angles less than 20° , but they attenuate the reflected radiation at the largest emission zenith angles ($\theta > 80^\circ$). (b) The cloudy atmospheres include a single, optically-thick ($\tau_c = 60$) stratocumulus cloud at altitudes between 1.0 and 1.5 km. In cloudy skies, weakly-absorbing aerosols attenuate the reflected sunlight at all emission angles.

Figure 42. Reflected radiances shown in Figure 41 were integrated over the wavelength range, 0.3 to $1.0\mu\text{m}$ and displayed as a function of emission zenith angle for clear and cloudy atmospheres with and without aerosols. In clear skies, weakly absorbing aerosols increase the reflected radiance at small emission angles because they are much brighter than the underlying dark surface. However, at the largest emission angles, where Rayleigh scattering dominates, these aerosols can reduce the intensity of the reflected radiation. In atmospheres occupied by optically-thick clouds, aerosol absorption above the cloud tops attenuates the reflected sunlight at all emission angles, but a larger fraction of the radiation reflected into the largest zenith angles is absorbed by these aerosols. The thin dotted line shows the effect of scaling the radiances reflected by the aerosol-free atmosphere (SC $\tau_a = 0$) by a constant factor (0.877) such that they matched the results for the aerosol laden atmosphere at the largest emission angle. If the aerosol absorption was independent of the emission angle, this dotted curve would

lie along the results for the aerosol-laden atmosphere (dash-dot-dot-clot).

Figure 43. Column-integrated atmospheric absorption in cloudy, aerosol-laden atmospheres for global-annual-average illumination conditions. Each cloudy atmosphere includes a single altostratus (AS) cloud deck with $0.5 \mu\text{m}$ optical depths between 0.3 and 60 at altitudes between 3.6 and 4.8 km. The aerosol-laden atmospheres have uniformly-mixed aerosols with the nominal Jaenicke size distribution (Figures 1 and 2), and column-integrated optical depths between 0.1 and 0.2 at $0.5 \mu\text{m}$. About half of the aerosol column extends above the cloud tops. Results for the nominal, cloud-free, aerosol-free atmosphere are shown as a thin, solid, horizontal line (74.5 W m^{-2}).

Figure 44. Column-integrated atmospheric absorption in cloudy, aerosol-laden atmospheres for global-annual-average illumination conditions. Each cloudy atmosphere includes a single cirrus cloud deck with $0.5 \mu\text{m}$ optical depths between 0.3 and 60 at altitudes between 7 and 10 km. The aerosol-laden atmospheres have uniformly-mixed aerosols with the nominal Jaenicke size distribution (Figures 1 and 2), and column-integrated optical depths between 0.1 and 0.2 at $0.5 \mu\text{m}$. Less than 20% of the aerosol column extends above the cloud tops. Results for the nominal, cloud-free, aerosol-free atmosphere are shown as a thin, solid, horizontal line (74.5 W m^{-2}).

Figure 45. Atmospheric net fluxes and heating rates for atmospheres with isolated or overlapping stratocumulus (SC) and alto-stratus (AS) clouds. Global-annual-average illumination conditions were used. The cloud types include moderately thick ($\tau_c=10$) SC clouds (SC(10)), moderately-thick ($\tau_c=10$) AS clouds (AS(10)), optically-thin ($\tau_c=1$) AS clouds (AS(1)), and “cloud sandwiches” composed of SC clouds with optically-thick AS clouds (SC(10)+AS(10)), or optically-thin AS clouds (SC(10)+AS(1)). Results for aerosol free and aerosol-laden atmospheres are shown. The aerosol laden atmospheres have constant particle number densities below 12 km (0.2 Bars), the nominal aerosol size distribution, and $0.5 \mu\text{m}$ optical depths of 0.1 or 0.2. (a) Atmospheric net solar flux distributions in clear and cloudy aerosol-free atmospheres. (b) same as (a) for

aerosol-laden atmospheres with column-integrated aerosol optical depths. $\tau_a = 0.1$.

(c) Same as (b) for $\tau_a = 0.2$. (d) Solar heating rates in clear and cloudy aerosol-free atmospheres. (e) Same as (d) for aerosol-laden atmospheres with $\tau_a = 0.1$. (f) Same as (e) for aerosol-laden atmospheres with $\tau_a = 0.2$.

Figure 46. Atmospheric net fluxes and heating rates are shown as functions of altitude in clear atmospheres and atmospheres with isolated or overlapping stratocumulus (SC) and cirrus (Cir) clouds. Global-annual-average illumination conditions were used. The cloud types include moderately thick ($\tau_c = 10$) SC clouds (SC(10)), moderately-thick ($\tau_c = 1$) Cir clouds (Cir(1)), optically-thin ($\tau_c = 0.1$) Cir clouds (Cir(0.1)), and “cloud sandwiches” composed of SC clouds with optically-thick Cir clouds (SC(10)+Cir(1)), or optically-thin Cir clouds (SC(10)+Cir(0.1)). Results for aerosol free and aerosol-laden atmospheres are shown (see Figure 45). (a) Atmospheric net solar flux distributions in clear and cloudy aerosol-free atmospheres. (b) same as (a) for aerosol-laden atmospheres with column-integrated aerosol optical depths, $\tau_a = 0.1$. (c) Same as (b) for $\tau_a = 0.2$. (d) Solar heating rates in clear and cloudy aerosol-free atmospheres. (e) Same as (d) for aerosol-laden atmospheres with $\tau_a = 0.1$. (f) Same as (e) for aerosol-laden atmospheres with $\tau_a = 0.2$.

Figure 47. Upward solar fluxes at the top of the atmosphere are shown for clear atmospheres above desert (panels a and b) and snow (panels c and d) covered surfaces (Figure 8). The solar zenith angle is 60 degrees. Results for aerosol free (solid line) and aerosol-laden (dotted line) atmospheres are shown. The aerosol laden atmospheres have constant particle number densities at altitudes below 12 km (0.2 Bars), the nominal Jaenicke aerosol size distribution, and column-integrated optical depths of 0.15.

Figure 48. Solar flux absorbed by clear atmospheres as a function of surface albedo and aerosol loading for global-annual-average illumination conditions. The aerosol laden atmospheres have constant particle number densities at altitudes below 12 km (0.2 Bars), the nominal Jaenicke aerosol size distribution, and column-integrated

optical depths of 0.1 to 0.2.

Figure 49. Column-integrated atmospheric absorption in cloudy, aerosol-laden atmospheres over dark (Ocean) and moderately-bright (Desert) surfaces for global-annual-average illumination conditions. Each cloudy atmosphere includes a single stratocumulus (SC), altostratus (AS), or cirrus (Cir) cloud, and uniformly-mixed aerosols with the nominal Jaenicke size distribution (Figures 1 and 2). and column-integrated optical depths of 0.1.

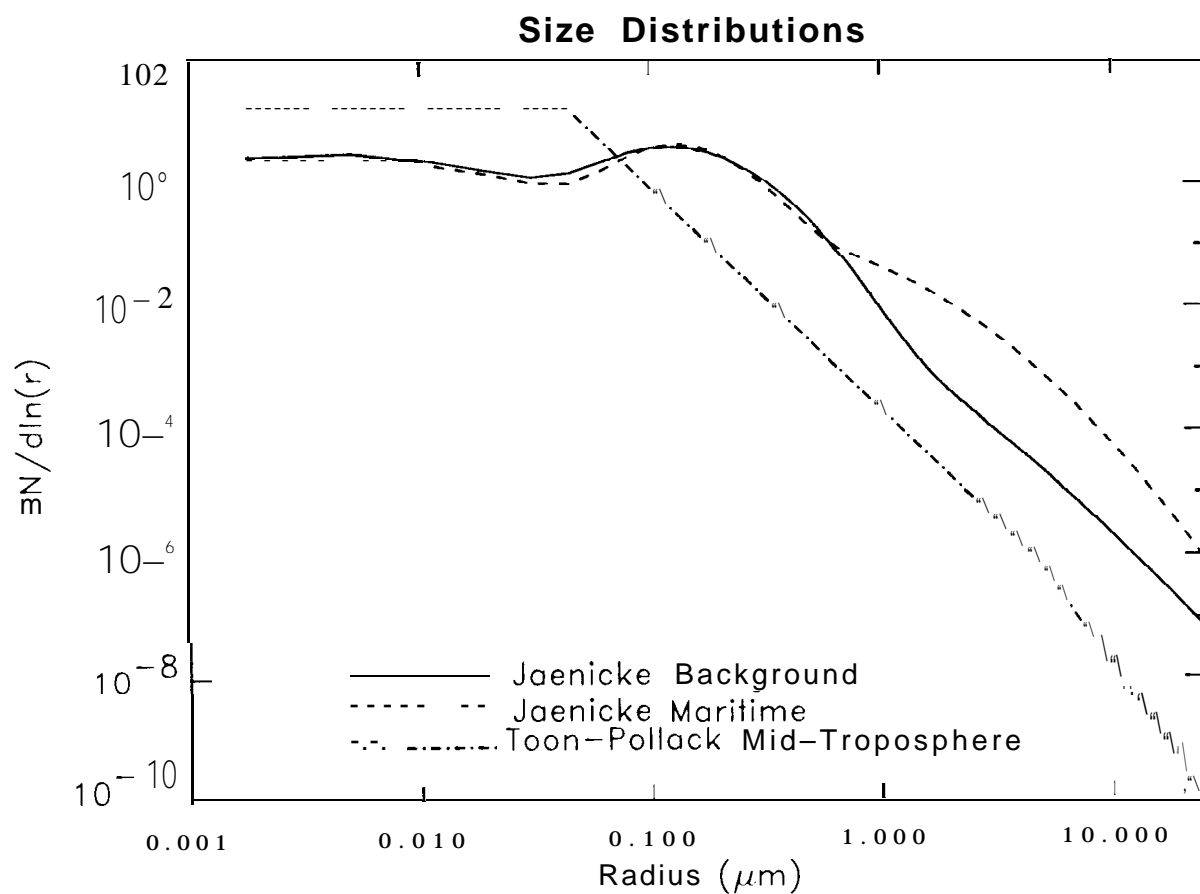


Figure 1. Particle size distributions for the nominal (Jaenicke Background) and alt innate (Toon-Pollack Mid-Troposphere) background and boundary layer (Jaenicke Maritime) aerosol distributions adopted in this study.

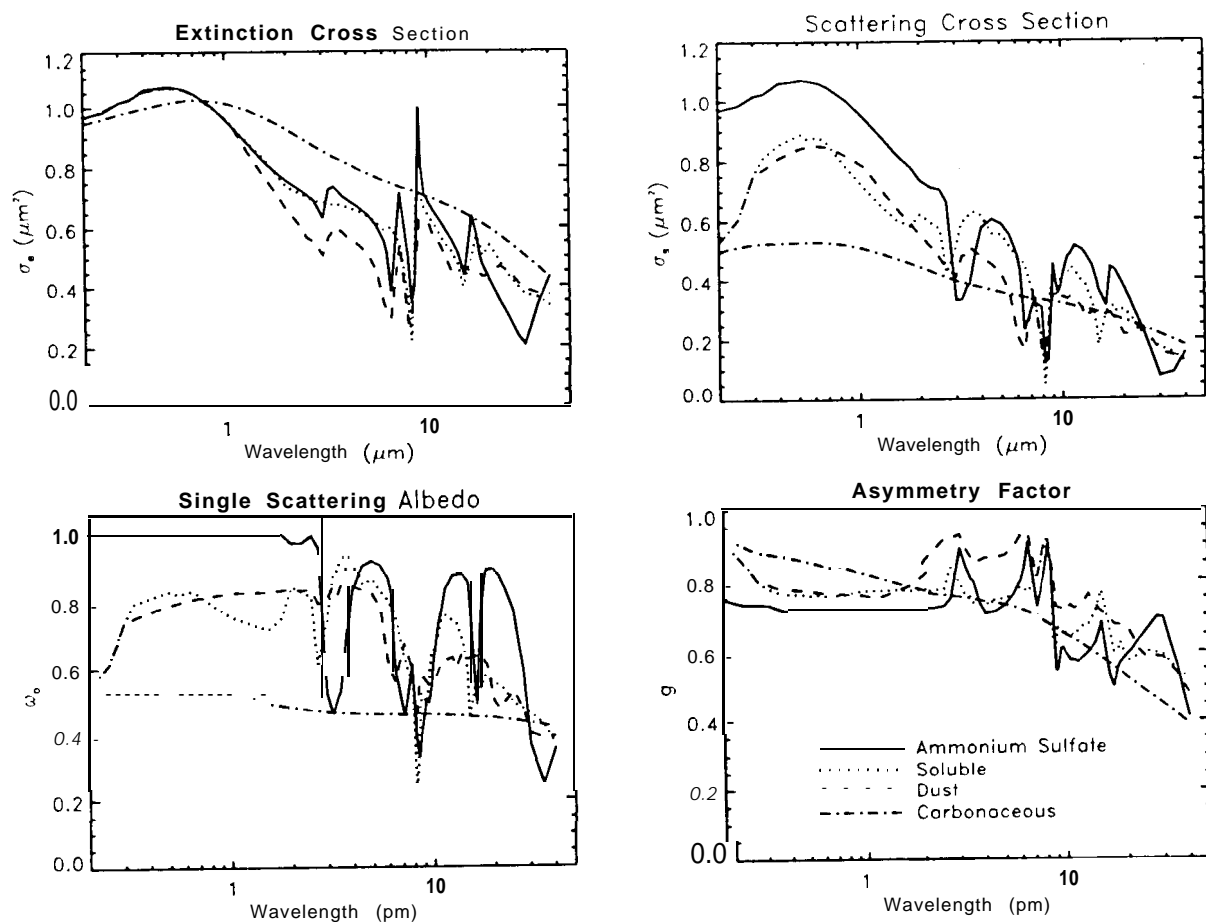


Figure 2. Wavelength-dependent single scattering optical properties (extinction cross section, σ_e , scattering cross section, σ_s , single scattering albedo, ω_o , and scattering asymmetry parameter, g) for ammonium sulfate, soluble organics, dust, and carbonaceous aerosols with the nominal Jaenicke (1993) background aerosol size distribution.

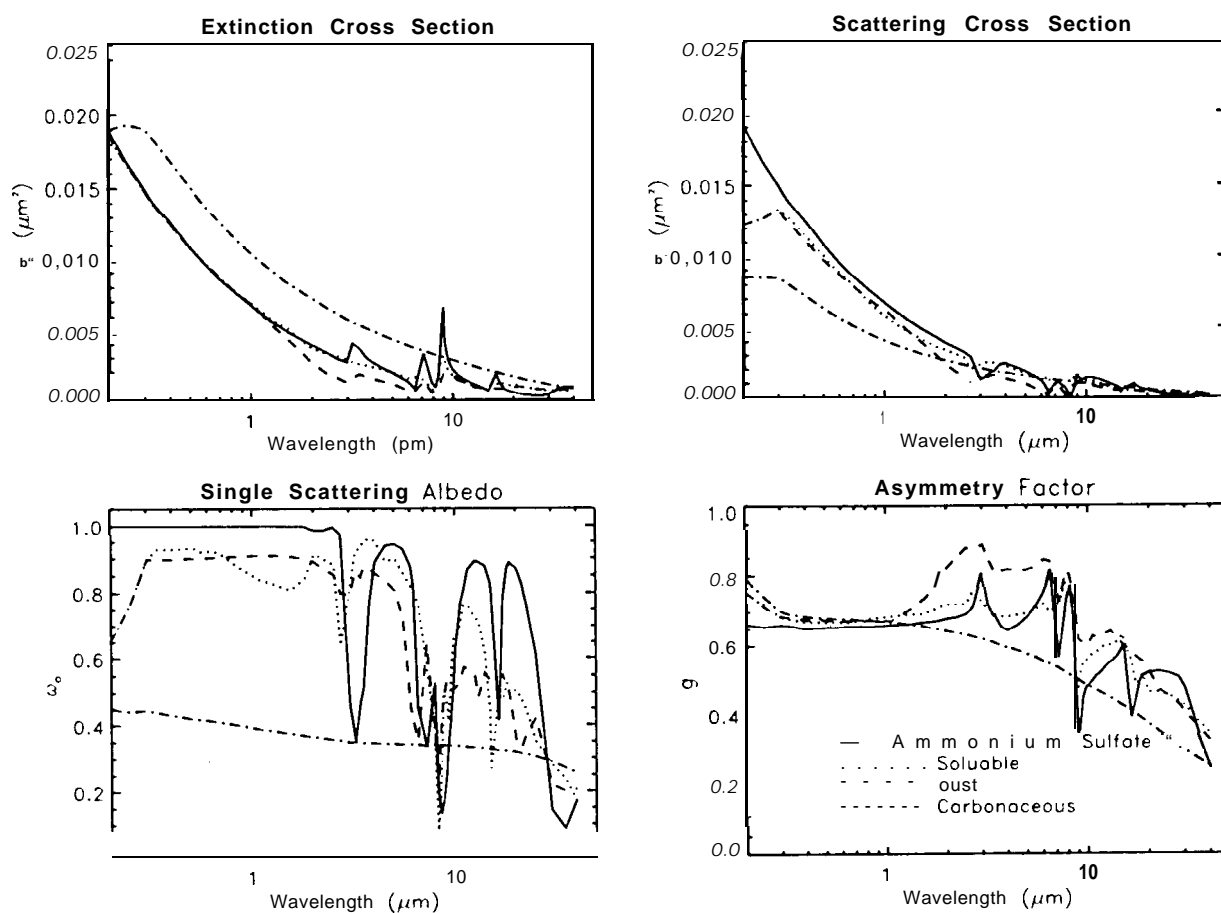


Figure 3. Wavelength- dependent single scattering optical properties for ammonium sulfate, soluble organics, dust, and carbonaceous aerosols with the alternate Toon-Pollack mid-troposphere size distribution.

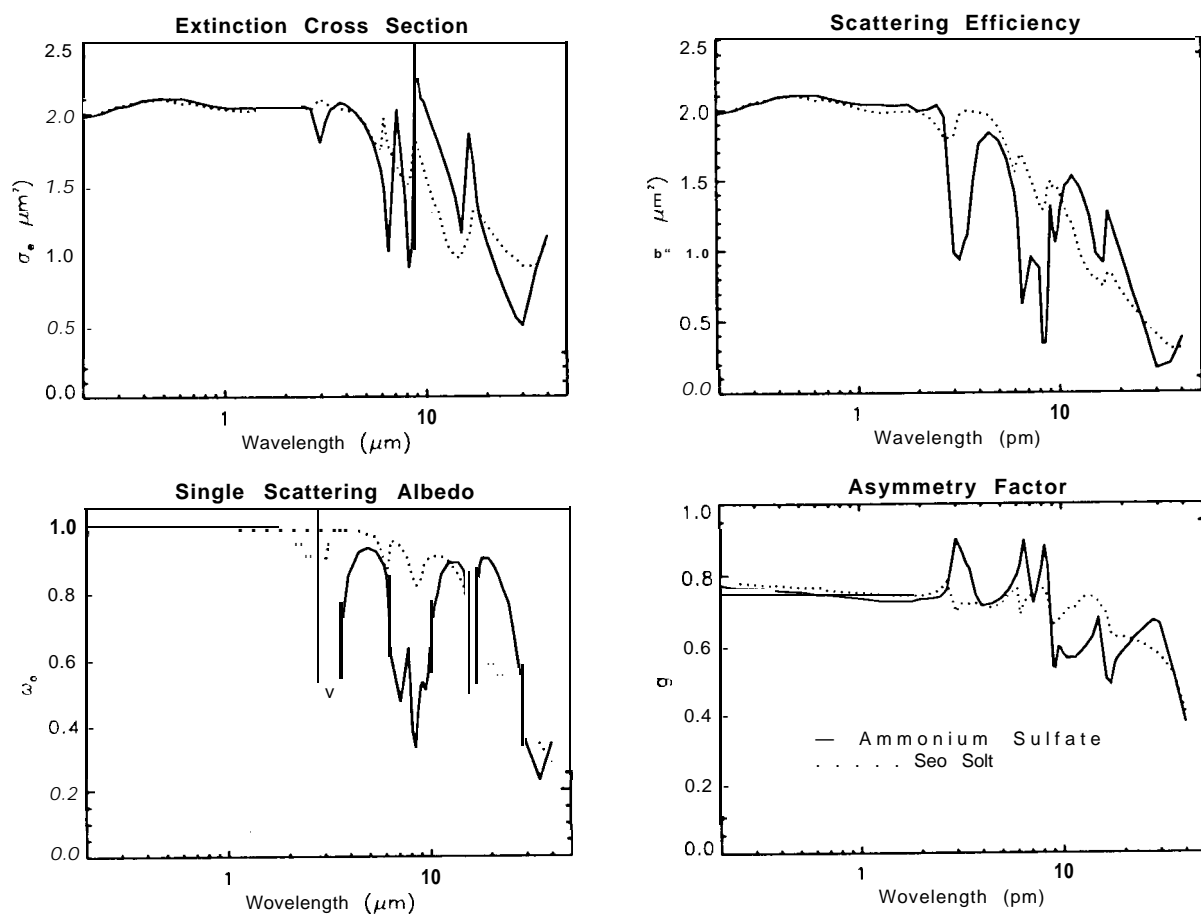


Figure 4. Wavelength-dependent single scattering optical properties for ammonium sulfate and sea salt aerosols with the Jaenicke Maritime size distribution.

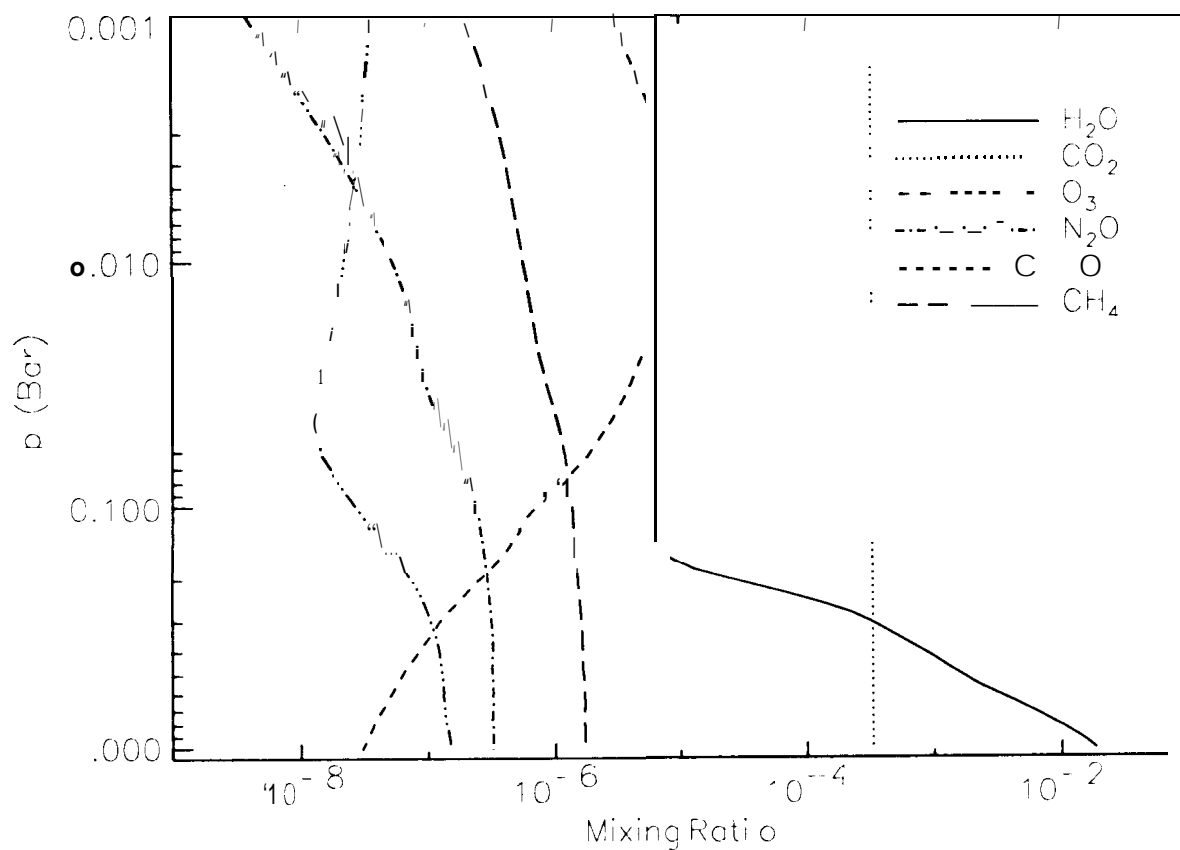


Figure 5. Volume mixing ratios for H_2O , CO_2 , O_3 , N_2O , CO , and CH_4 for the nominal Mid-Latitude Summer (MLS) atmosphere (McClatchey et al. 1972) are shown as a function of pressure. The Volume mixing ratio of O_2 (not shown here) was .21.

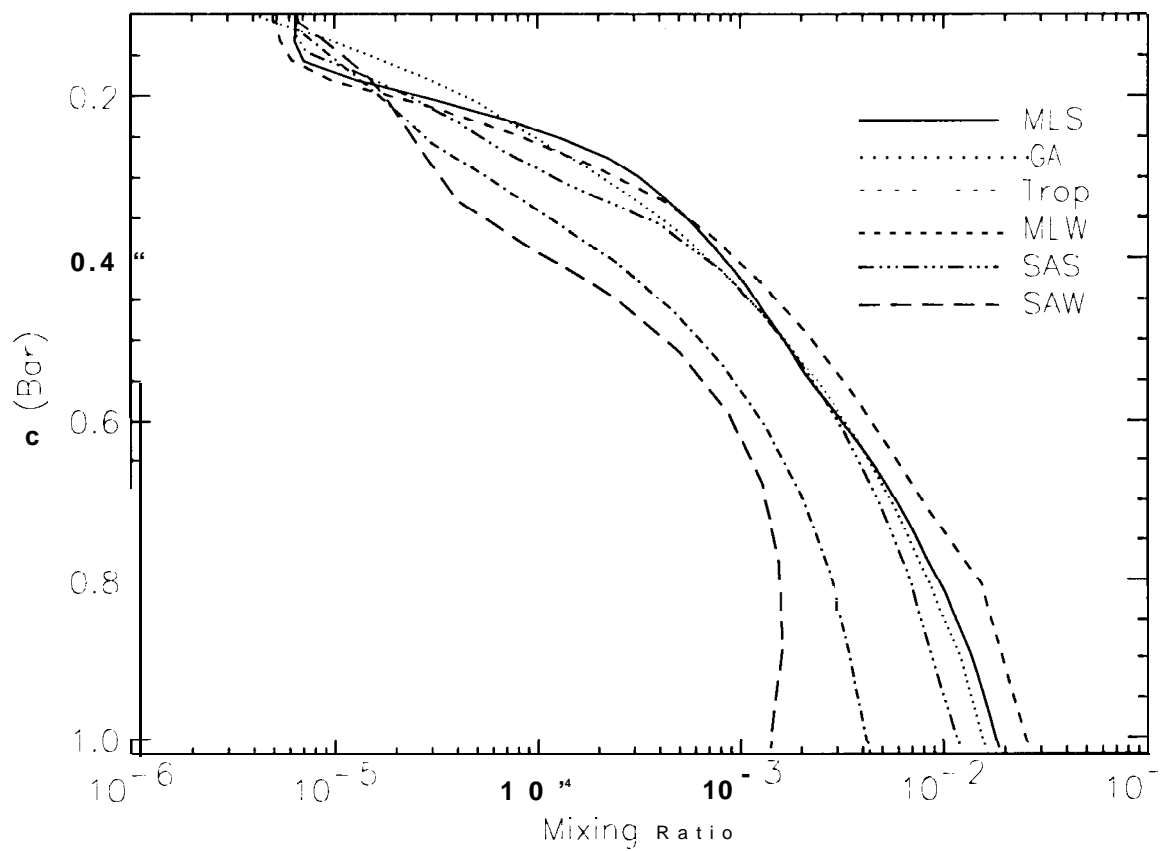


Figure 6. Comparison of water vapor mixing ratio profiles, including the Mid-Latitude Summer (MLS), Tropical (Trop), Mid-Latitude Winter (MLW), Sub-Arctic Summer (SAS), and Sub-Arctic Winter (SAW) from McClatchey et al. (1972). A globally-averaged profile (GA) derived from climatological results presented by Peixoto and Oort (1992) is also shown.

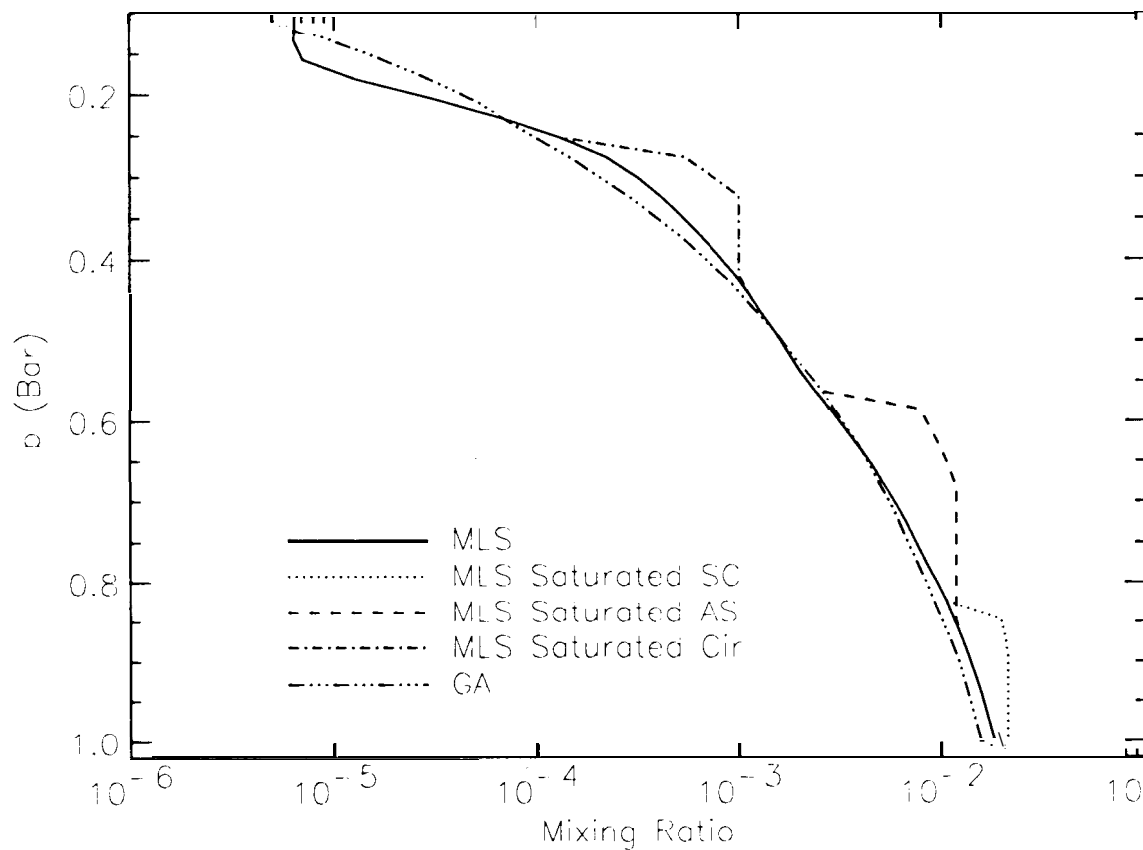


Figure 7. The nominal MLS water vapor profile is compared to alternate profiles that are saturated within Stratocumulus (SC), Altostratus (AS) and Cirrus (Cir) cloud decks. The mixing ratios are set to a constant value between the cloud base and the level where they intersect the nominal mixing ratio profile.

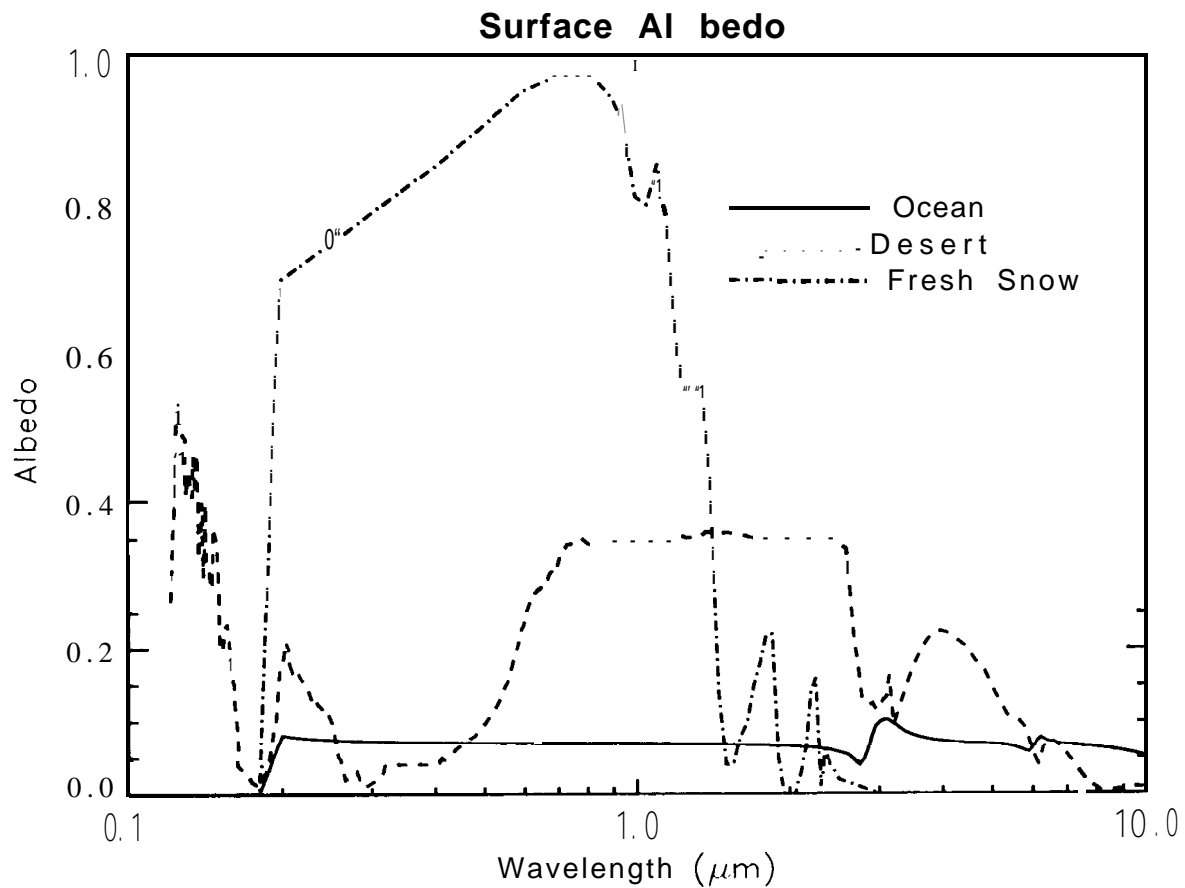


Figure 8. Surface albedo spectra for a moderately rough ocean surface, (rms wave slopes of 15 degrees), a desert surface (adapted from spectra of the planet Mars, which resembles terrestrial deserts at visible and near infrared wavelengths), and a moderately fresh snow-covered surface.

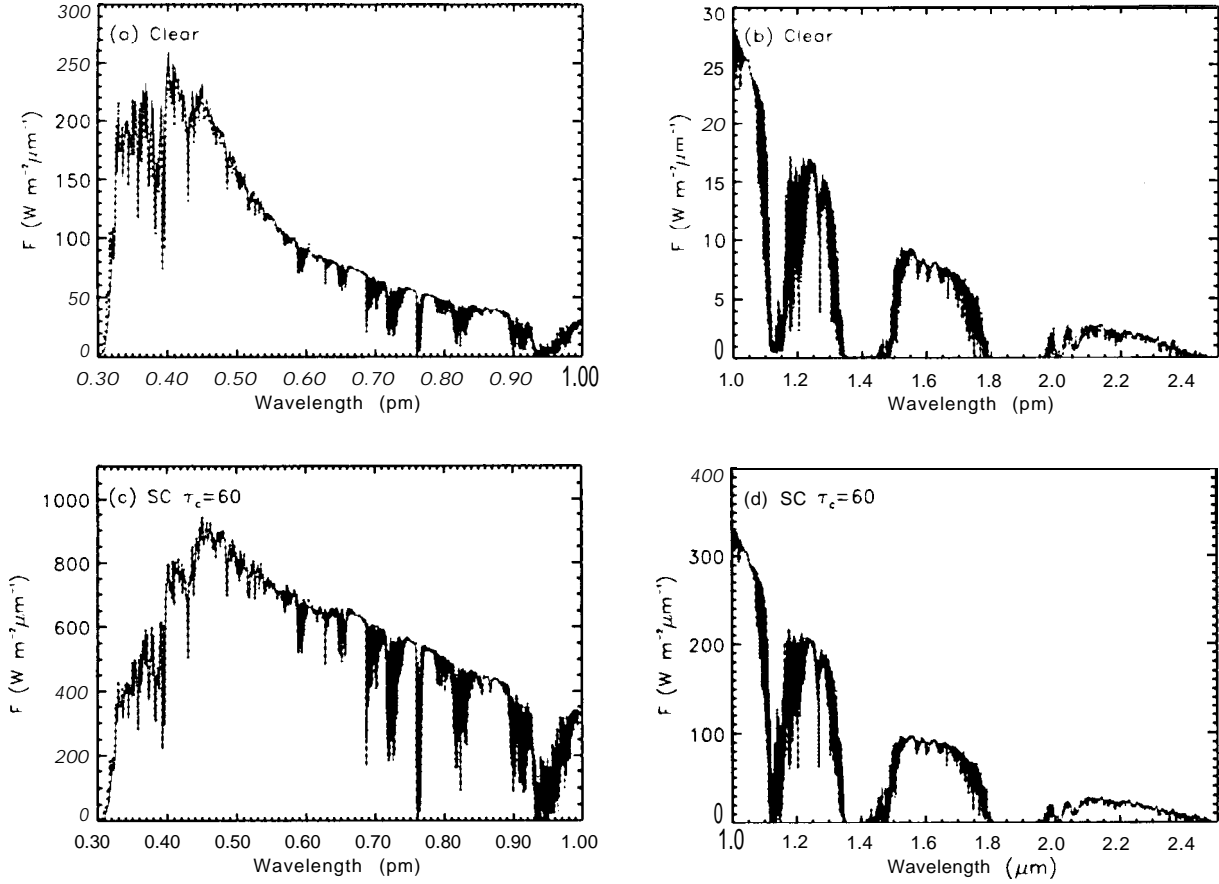


Figure 9. Comparison of upward solar flux spectra above clear and cloudy atmospheres obtained with the DART (solid line) and SMART (dotted line) models. The solar zenith angle is 60° . The visible and near-infrared parts of each spectrum are displayed separately (left and right hand panels) with their wavelength and intensity scales optimized to reveal the most prominent spectra features. Panels (a) and (b) show the reflected fluxes above clear atmospheres with nominal dark ocean surfaces. Panels (c) and (d) show the upward visible and near-infrared fluxes above atmospheres with a single optically-thick ($\tau_c=60$) stratocumulus cloud deck above a dark ocean surface. The results obtained by DART and SMART are virtually indistinguishable for these cases. The largest differences are 2 to 4%, but these differences are both positive and negative, and tend to average out over broad spectral regions.

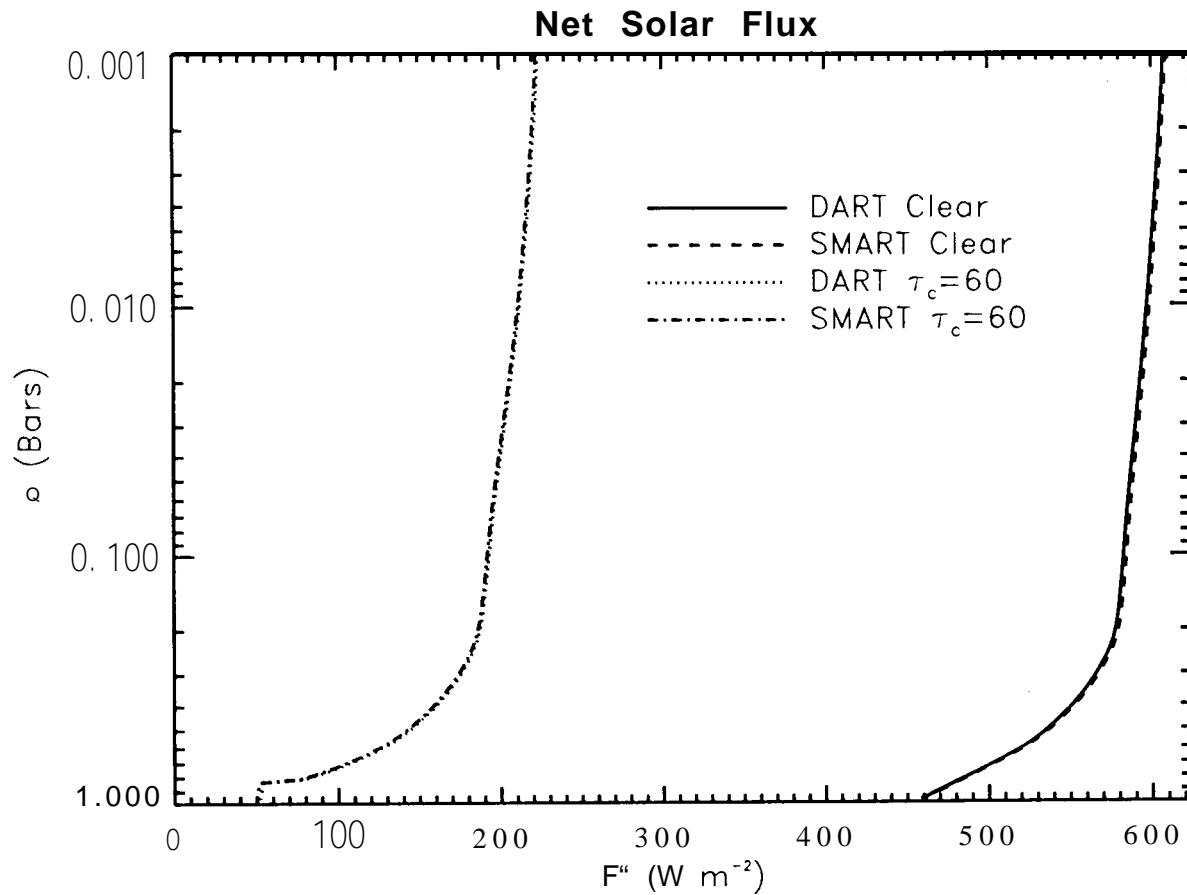


Figure 10. Comparison of spectrally-integrated (O. 125 to $8.3\mu\text{m}$) net solar flux profiles obtained with the DART and SMART models for the clear and cloudy atmospheres described in Figure 9. The differences between these two models never exceeds 2%. The net flux at the top of the atmosphere indicates the total solar energy absorbed by the surface-atmosphere system, while the net flux at the surface indicates the amount of flux absorbed at that level. This column-integrated absorption slightly exceeds that shown here because this plot does not show the flux divergence at mesospheric levels.

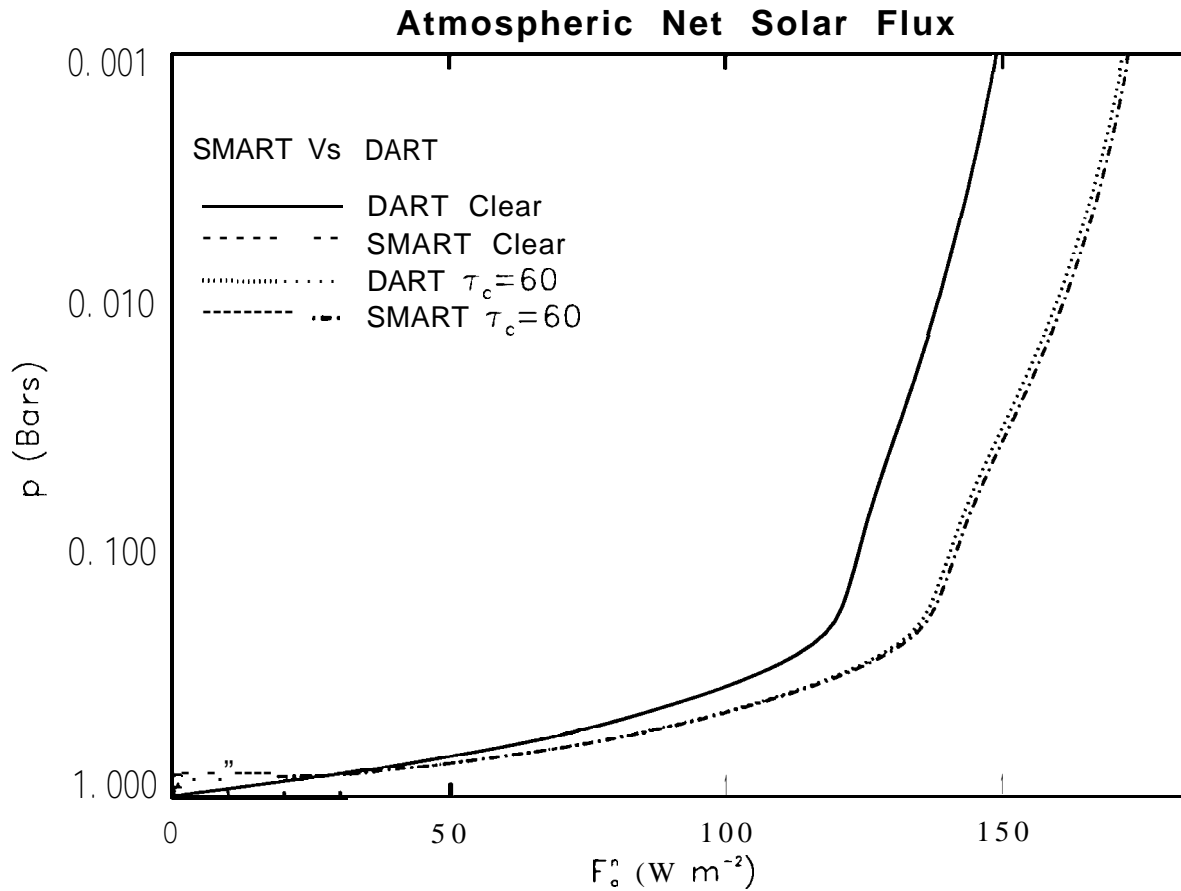


Figure 11. Comparison of spectrally-integrated (0.125 to $8.3\mu\text{m}$) atmospheric net flux profiles obtained with SMART and DART for the clear and cloudy atmospheres described in Figure 9. The quantity, F_a^n is derived from the total (surface + atmosphere) net fluxes (Figure 10) by subtracting the net solar flux absorbed at the surface from the net flux absorbed at each atmospheric level. The value of F_a^n at the top of the atmosphere indicates the total solar flux deposited in the atmospheres. Large flux divergences are seen near the surface ($p = 1 \text{ Bar}$) where water vapor is the principal absorber of solar radiation. Comparisons of these results with those shown in Figure 10 show that even though the surface-atmosphere system absorbs less solar radiation in cloudy regions, the atmosphere can actually absorb more radiation in these regions.

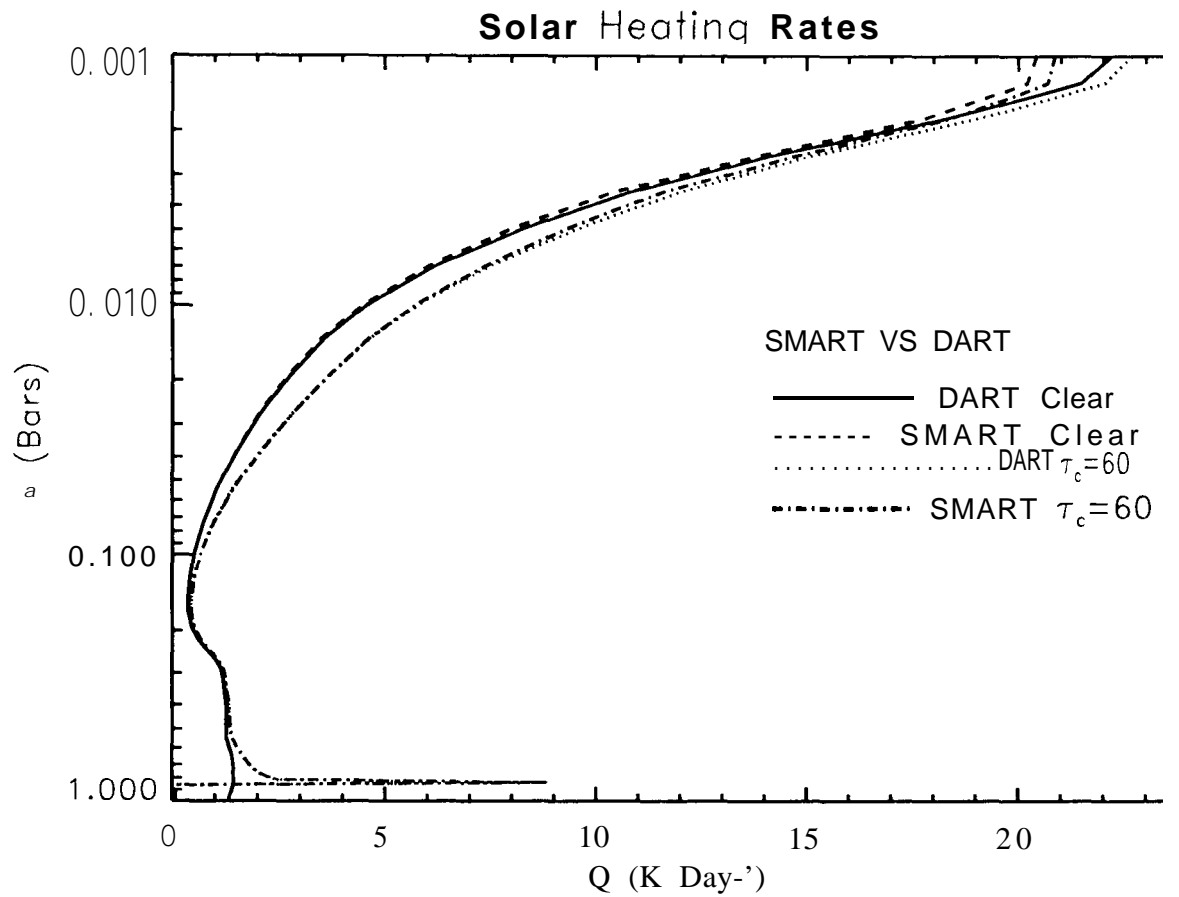


Figure 12. Solar heating rates obtained by DART and SMART for the model atmospheres and solar illumination conditions described in Figure 9. The differences between the exact (DART) and spectral mapping (SMART) models never exceed 2% at pressures greater than 0.002 Bars. The optically-thick ($\tau_c=60$) stratocumulus cloud enhances the heating rates at levels near the cloud top, but decreases the heating rates below the cloud base. The stratospheric heating rates are higher for the cloudy case because the weak ozone bands absorb some of the solar radiation reflected by the cloud tops.

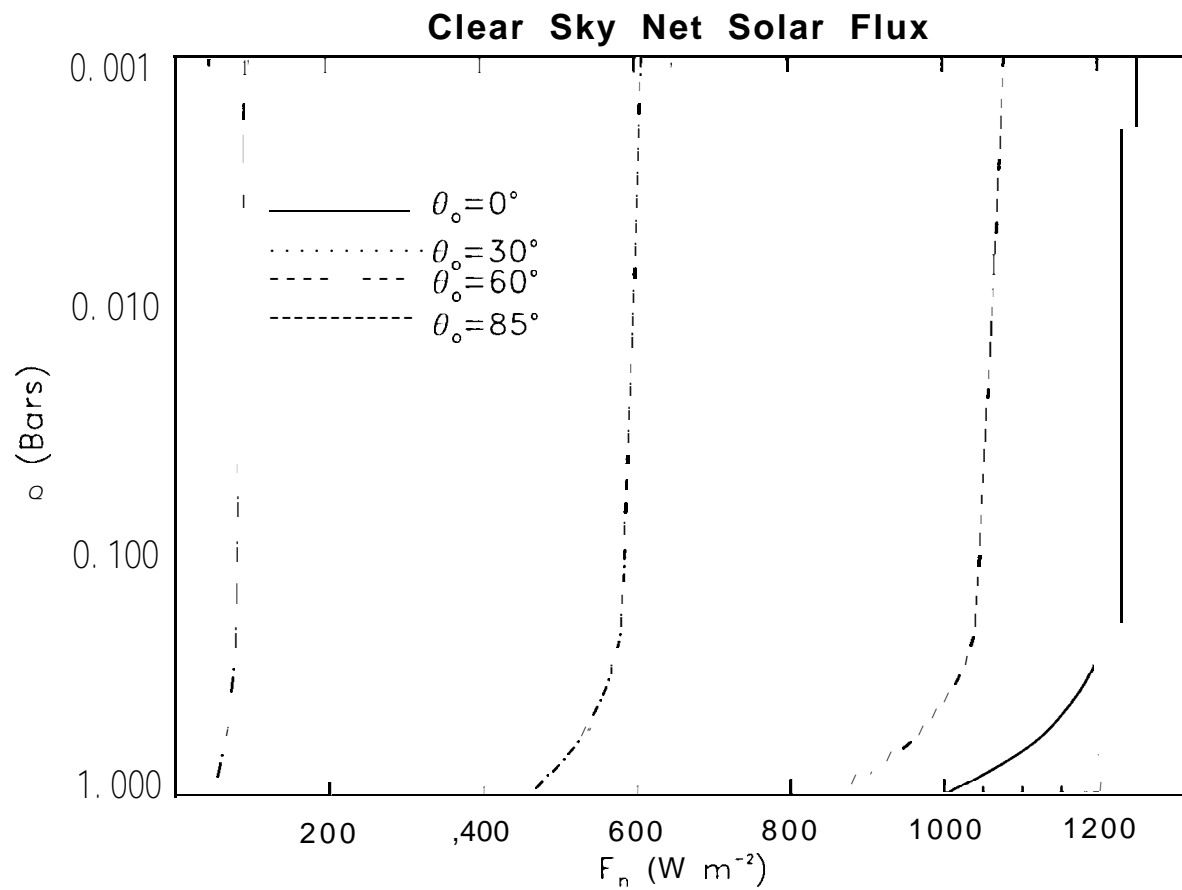


Figure 13. SMART clear sky net solar fluxes for the nominal MLS atmosphere are shown as a function of pressure and solar zenith angle.

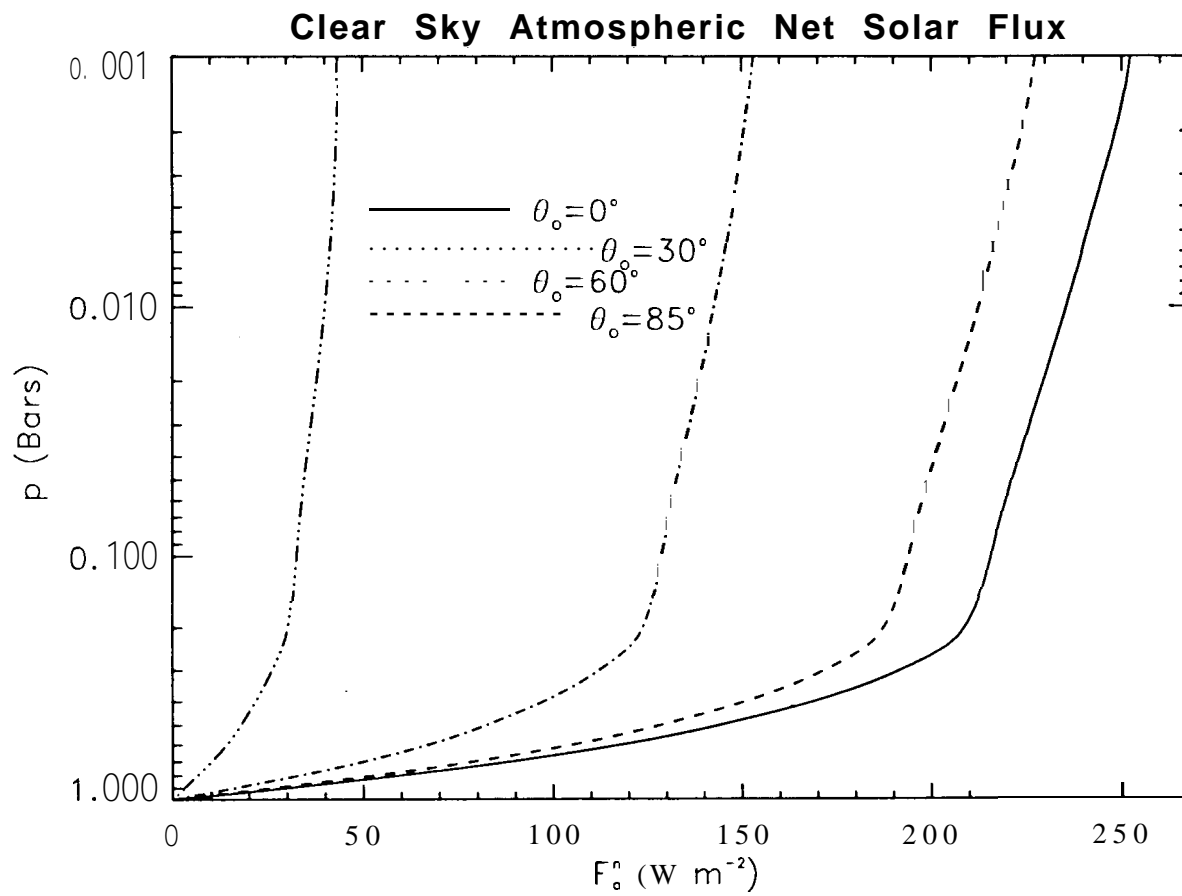


Figure 14. SMART clear sky atmospheric net solar fluxes for the nominal MLS atmosphere are shown as a function of pressure and solar zenith angle.

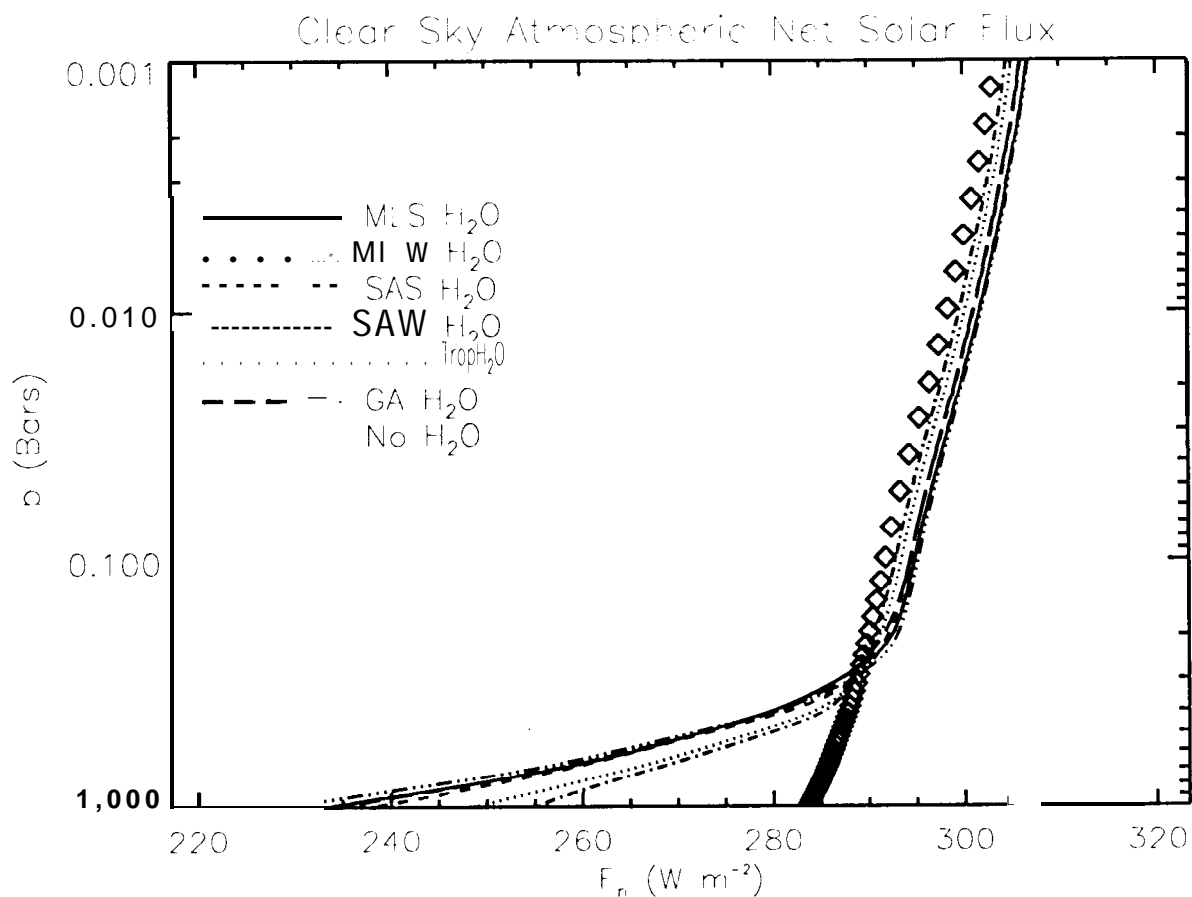


Figure 15. SMART clear-sky net fluxes for globally-averaged illumination conditions and the nominal ocean surface albedos are shown for each of the water vapor mixing ratios shown in Figure 6, and for a case with no water vapor (diamonds). The omission of water vapor dramatically reduces the atmospheric absorption, but produces much smaller changes the solar flux absorbed by the surface-atmosphere system, because the radiation not absorbed by the atmosphere is deposited on the surface.

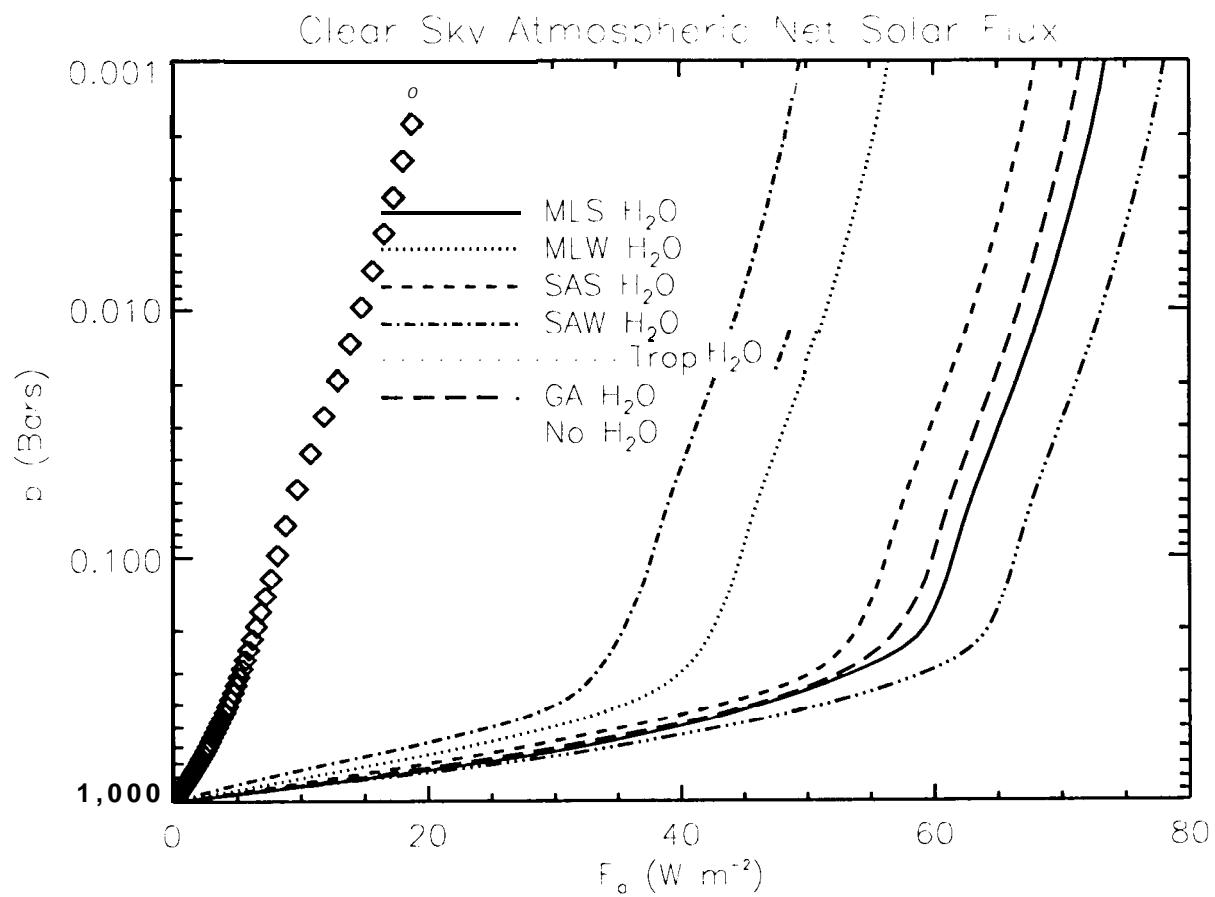


Figure 16. Atmospheric net fluxes as a function of altitude for the range of water vapor mixing ratios described in Figure 15.

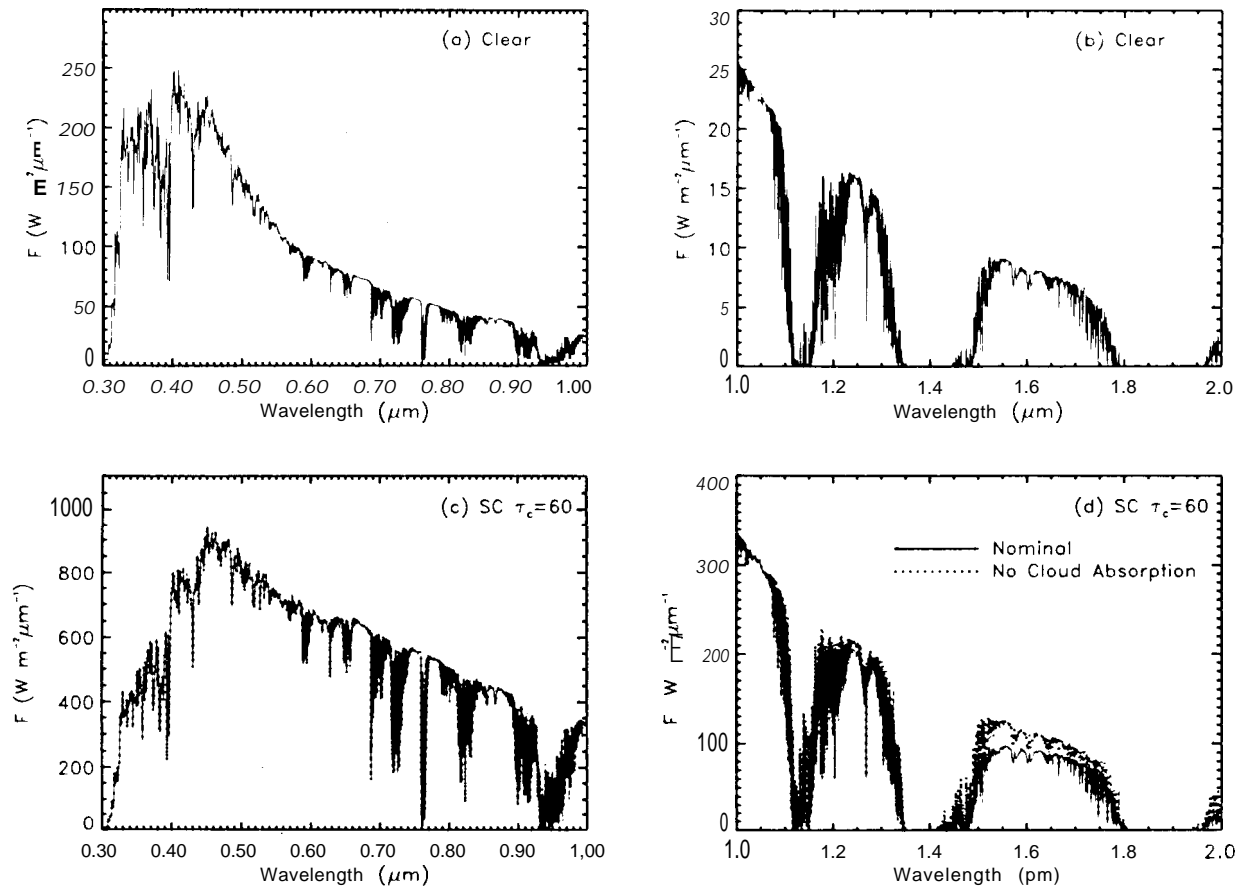


Figure 17. Solar flux spectra generated with the SMART model. These spectra show the reflected fluxes above clear and cloudy atmospheres for a solar zenith angle of 60° . Panels (a) and (b) show solar fluxes reflected by a cloud-free atmosphere above a dark ocean surface. Panels (c) and (d) show the fluxes reflected by an atmosphere that includes a single, optically-thick ($\tau_c=60$) stratocumulus (SC) cloud deck with (solid) and without (dotted) liquid water absorption.

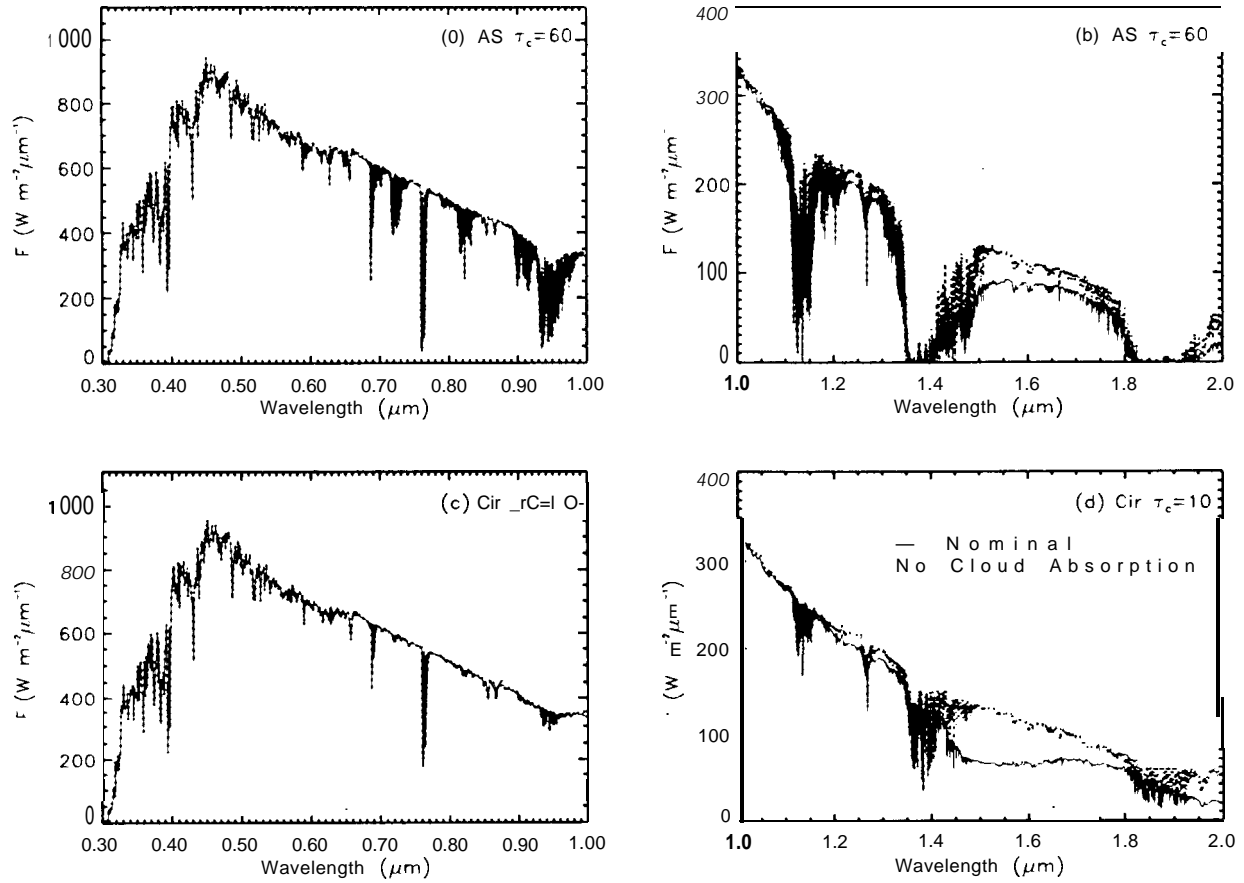


Figure 18. Same as Figure 17 for optically-thick ($\tau_c=60$) altostratus clouds with and without liquid water absorption (panels a and b) and optically-thick ($\tau_c=10$) cirrus clouds with and without water ice absorption (panels c and d).

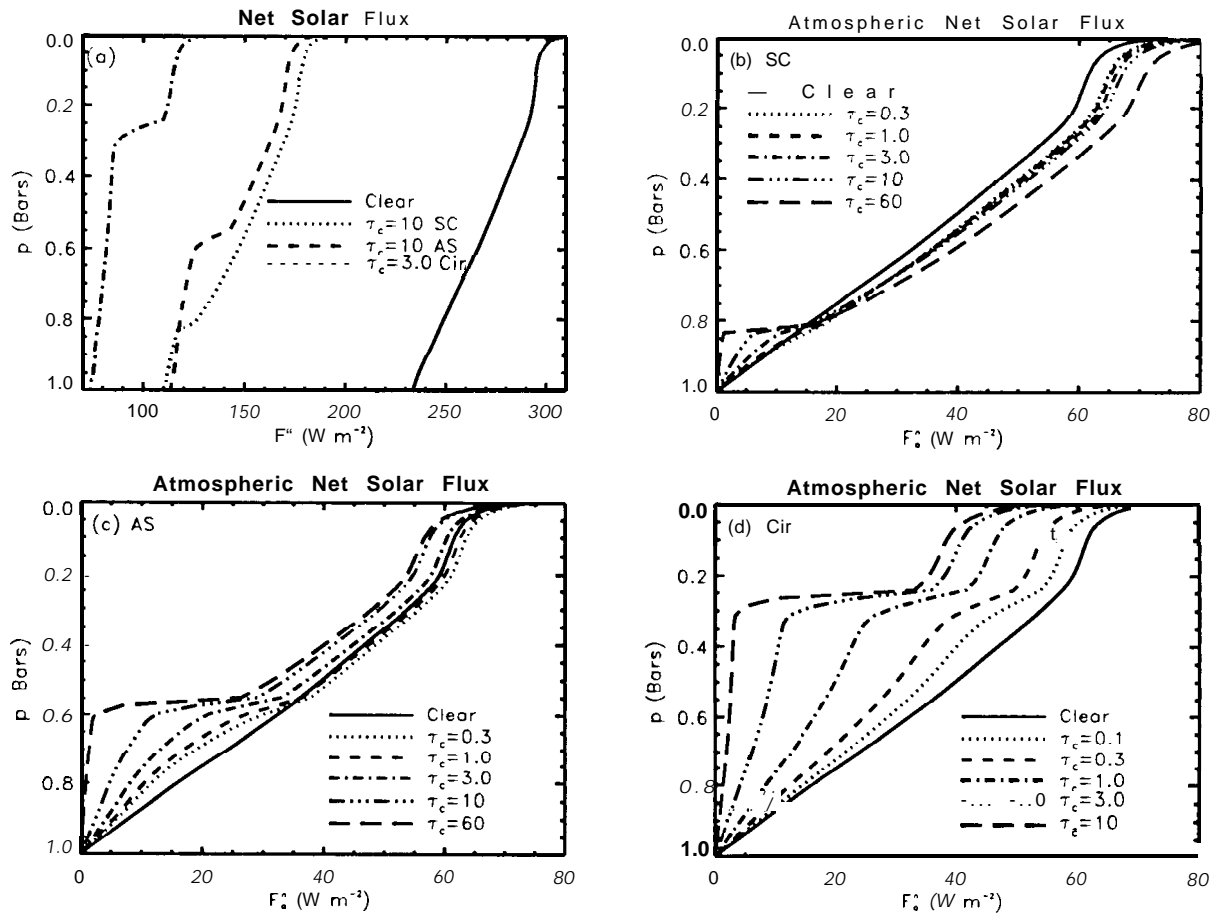


Figure 19. Net solar fluxes in clear and cloudy atmospheres with nominal MLS water vapor mixing ratios, ocean surface albedos and global-annual-average illumination conditions. (a) hTet solar fluxes as a function of pressure in clear and cloudy atmospheres. (b) Atmospheric net solar fluxes for atmospheres with stratocumulus (SC) clouds with a range of optical depths. (c) Atmospheric net solar fluxes for atmospheres with altostratus (AS) clouds with a range of optical depths. (d) Atmospheric net solar fluxes for atmospheres with cirrus (Cir) clouds with a range of optical depths.

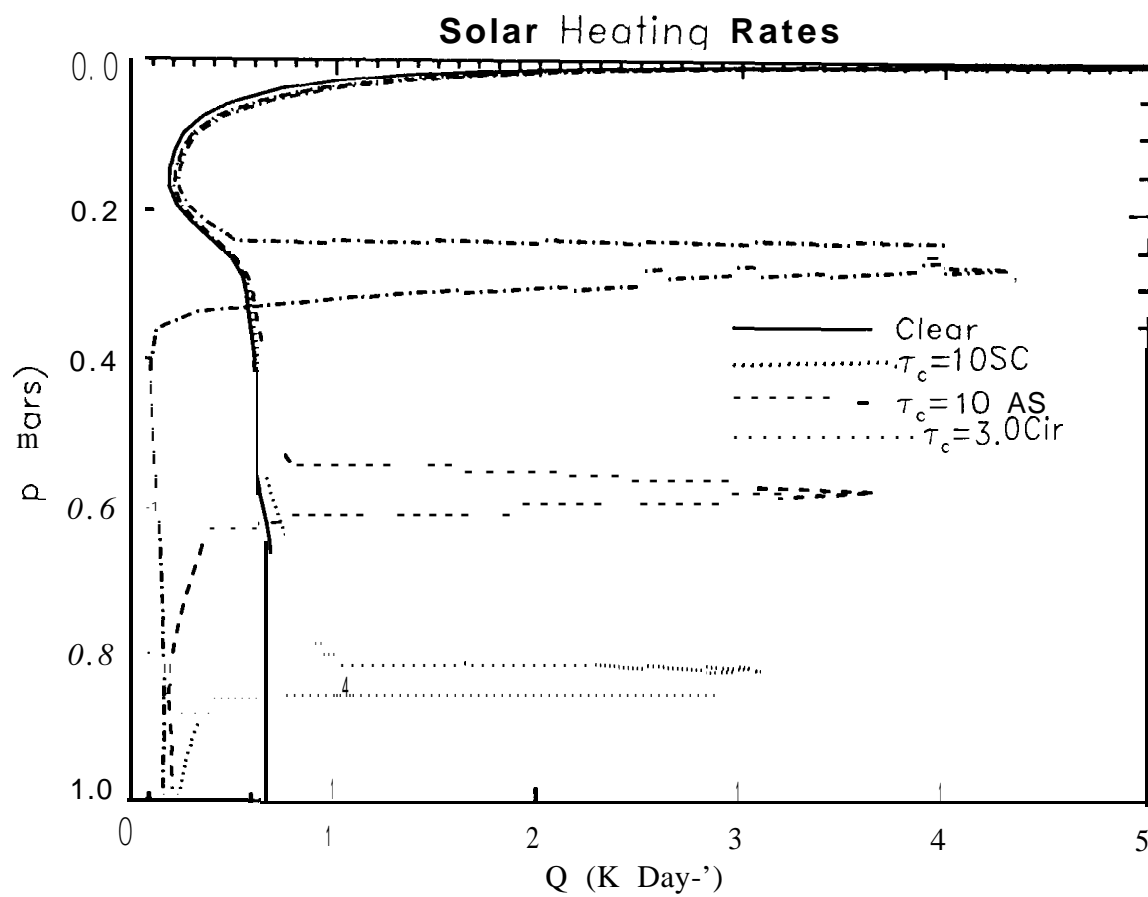


Figure 20. Tropospheric heating rates for clear atmospheres and atmospheres with moderately-thick stratocumulus (SC, $\tau_c=10$), altostratus (AS, $\tau_c=10$), and cirrus (Cir, $\tau_c=3$) clouds and global-annual-average illumination conditions,

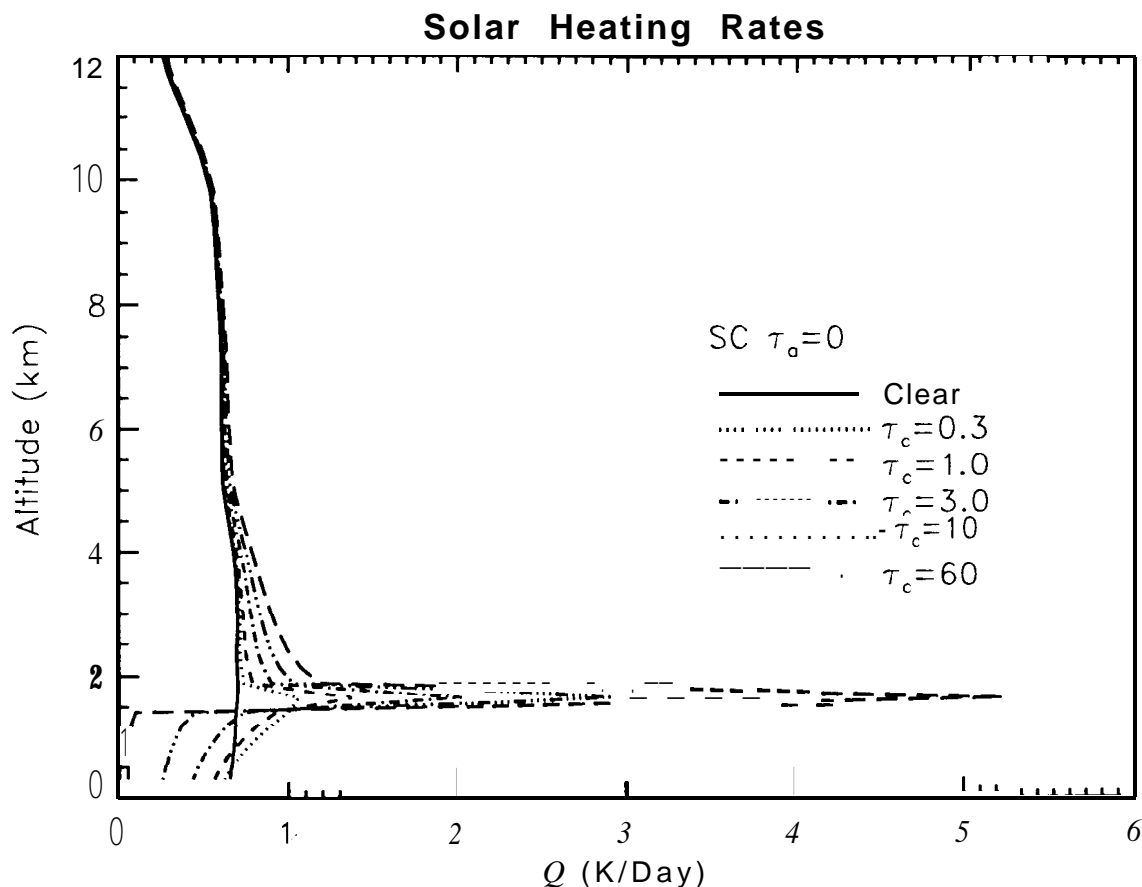


Figure 21. Tropospheric solar heating rates for a clear atmosphere, and for atmospheres with a single stratocumulus cloud deck with a range of optical depths ($0.3 < \tau_c < 60$). Optically-thin clouds increase the absorption and heating rates at all levels. For optically-thick low clouds, the heating rates near the cloud top increase with the cloud optical depth, but the heating rates below the cloud base decrease with increasing optical depth. The enhanced heating rates above the cloud are produced as some of the upwelling solar radiation that is reflected by the cloud is absorbed by water vapor above the cloud.

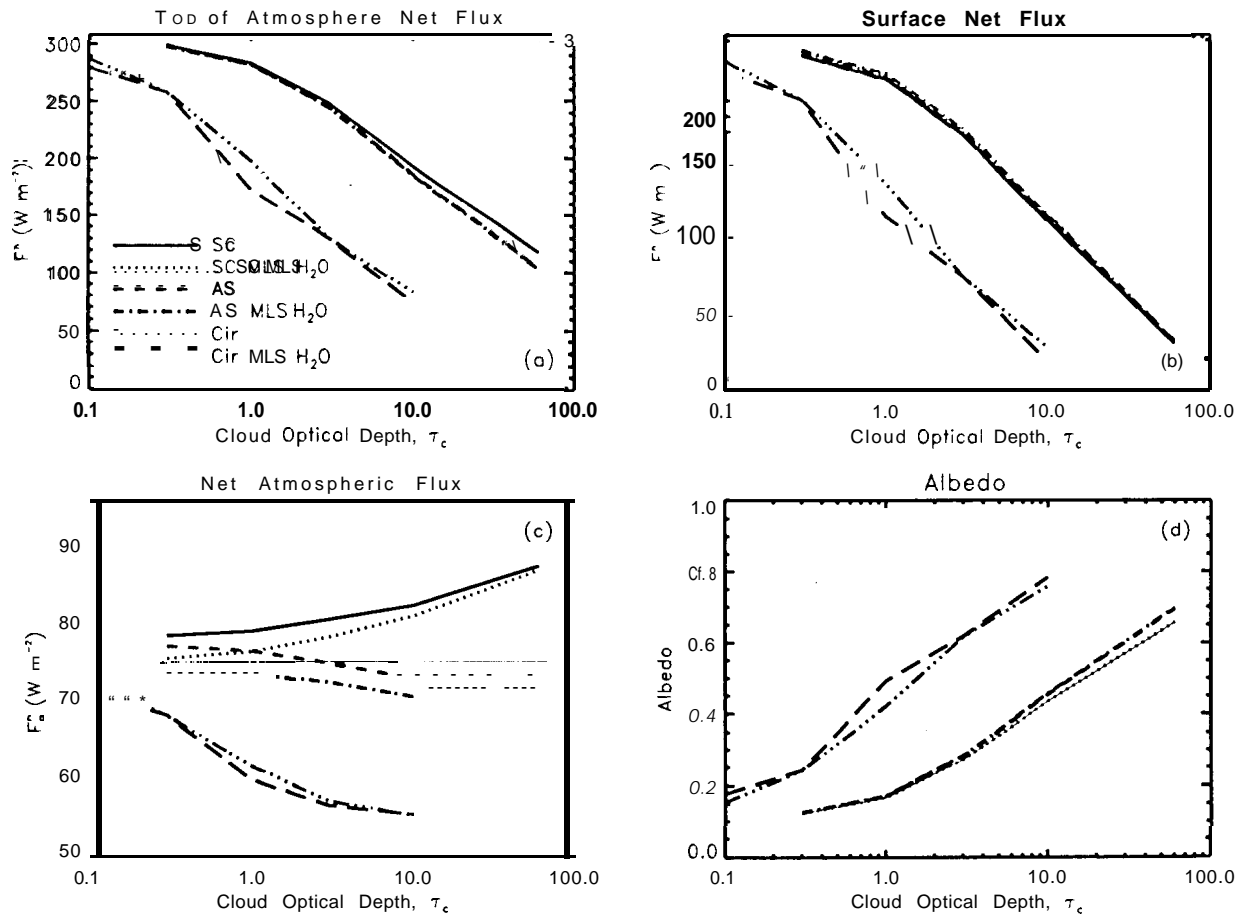


Figure 22. Net downward solar fluxes and albedos for cloudy atmospheres over dark (ocean) surfaces with global-annual-average illumination conditions. Each atmosphere includes a single low (SC), middle (AS), or high (Cir) cloud with a range of optical depths (Table 2). Results obtained for the MLS water vapor profile (MLS H_2O) are compared to those obtained when the water vapor mixing ratios are saturated within the cloud layers. (a) Net fluxes at the top of cloudy atmospheres as a function of cloud height and cloud optical depth, τ_c . The net flux at the top of the baseline clear atmosphere is 307.8 W m^{-2} for these illumination conditions. (b) Net fluxes at the surface as a function of cloud height and optical depth. The baseline clear-sky case absorbs 233.3 W m^{-2} at the surface for these illumination conditions. (c) Net solar flux absorbed by the atmosphere for the cloud and water vapor distributions described in panel (a). The baseline clear atmosphere absorbs 74.5 W m^{-2} (thin solid line). (d) Top-of-atmosphere albedos for the cloud and water vapor distributions used in panel (a).

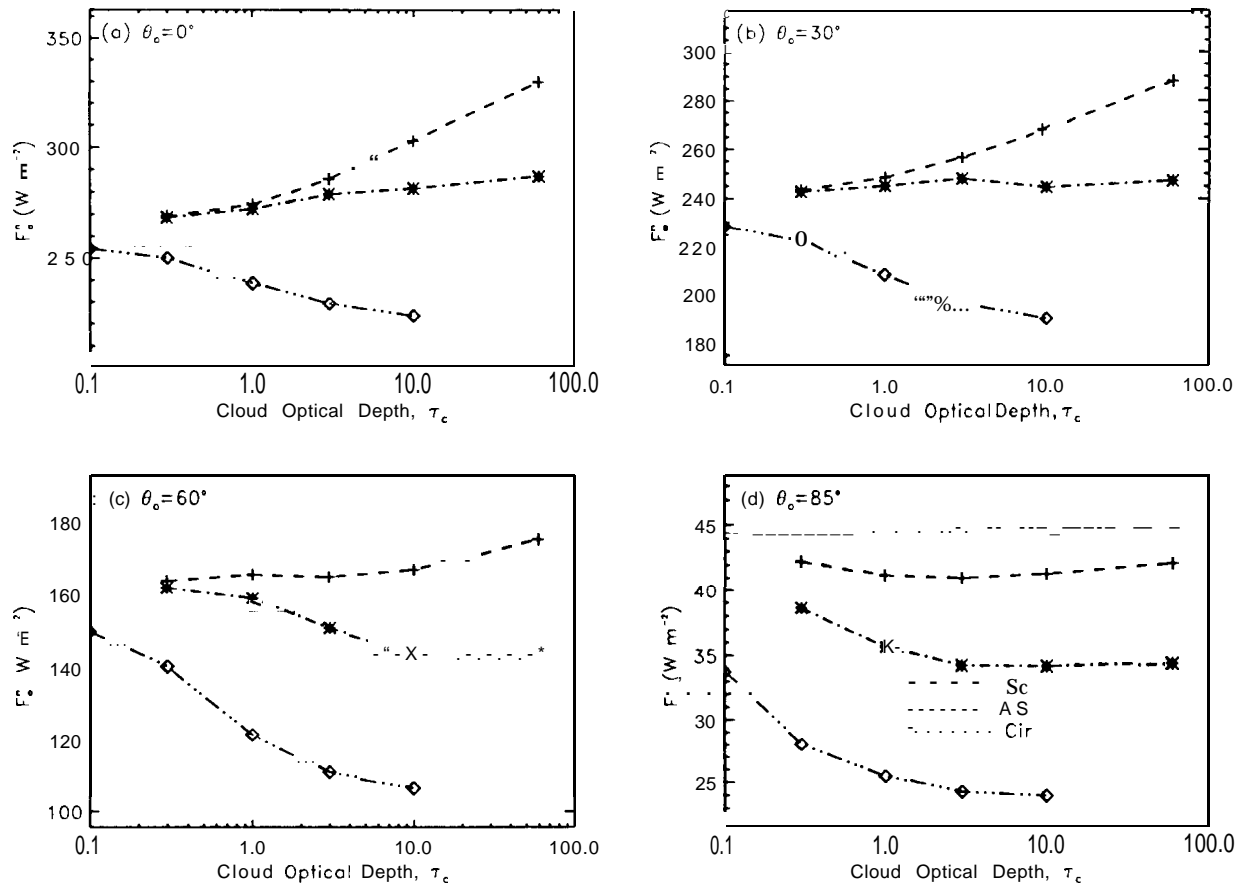


Figure 23. Atmospheric absorption in cloudy skies as a function of solar zenith angle and cloud optical depth. (a) Atmospheric fluxes for saturated low (SC), middle (AS), and high (Cir) clouds when the sun is at the zenith ($\theta_o=0^\circ$). For these conditions, the nominal clear atmosphere absorbs 255.9 W m^{-2} (thin solid line). (b) Same as (a) for a zenith angle of 30° , where the nominal clear atmosphere absorbs 230.2 W m^{-2} . (c) Same as (a) for a zenith angle of 60° , where the nominal clear atmosphere absorbs 155.5 W m^{-2} . (d) Same as (a) for a zenith angle of 85° , where the nominal clear atmosphere absorbs 44.4 W m^{-2} .

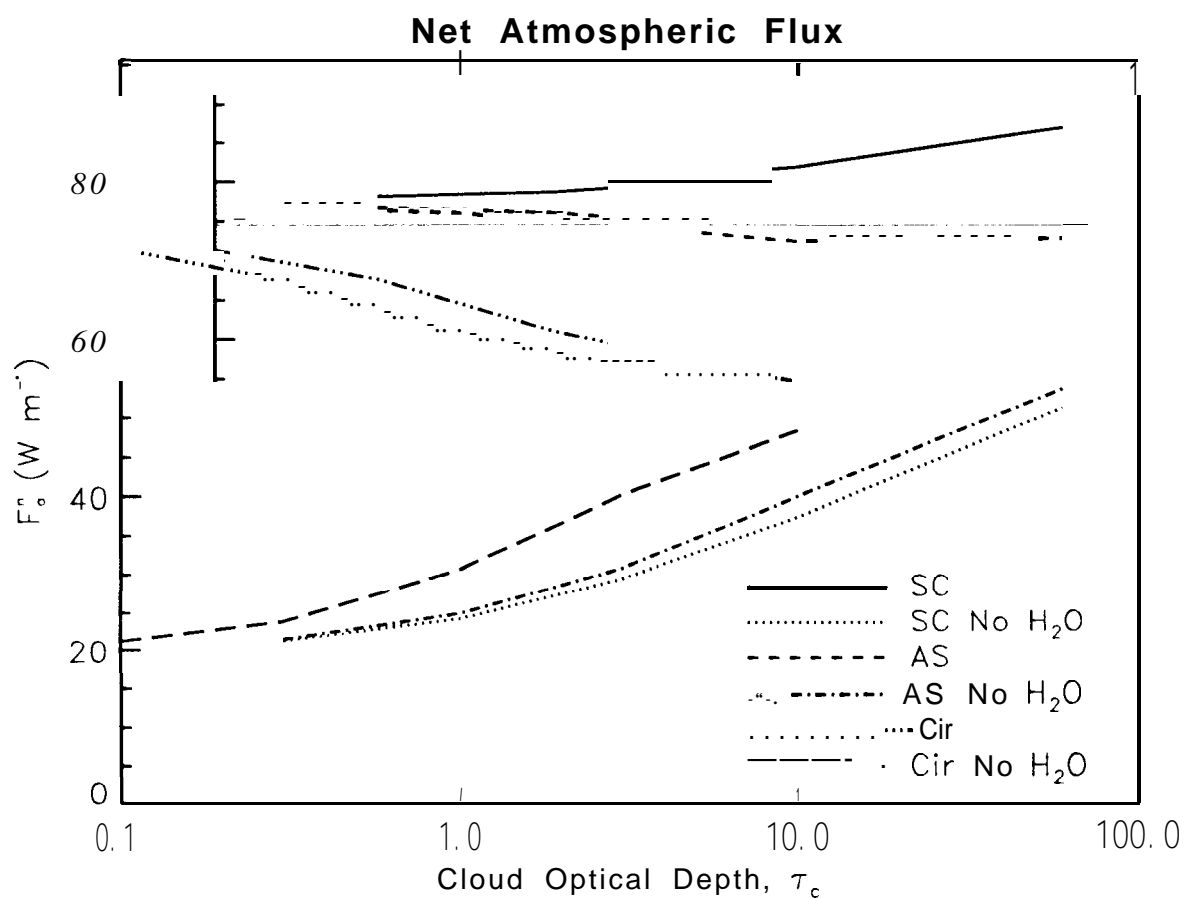


Figure 24. Column-integrated atmospheric absorption by cloudy atmospheres with and without water vapor (No H_2O). The thin, horizontal solid line shows the absorption by the baseline clear atmosphere with MLS gas mixing ratios (74.5 W m^{-2}).

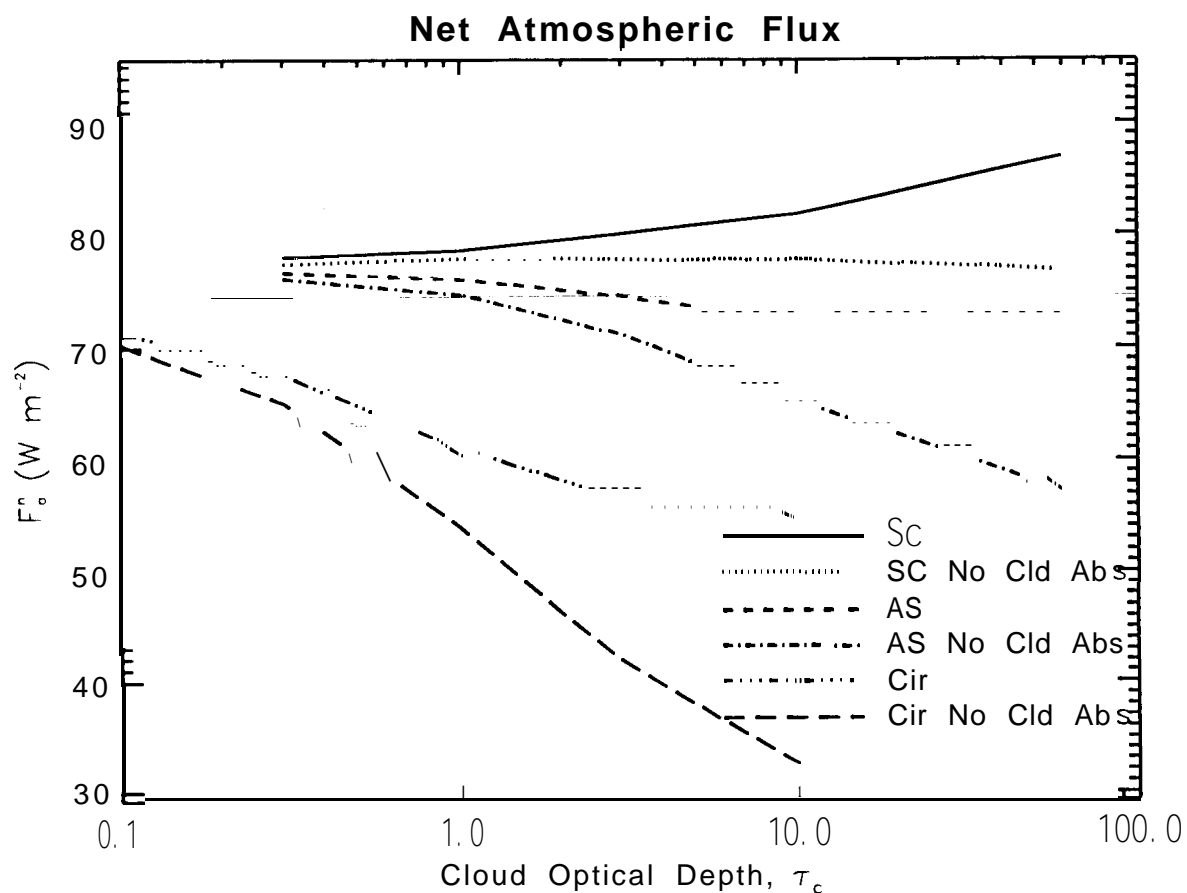


Figure 25. Column-integrated atmospheric absorption by cloudy atmospheres with and without cloud liquid water and ice absorption (No Cld Abs). The thin, horizontal solid line shows the absorption by the baseline clear atmosphere with MLS gas mixing ratios (74.5 W m^{-2}).

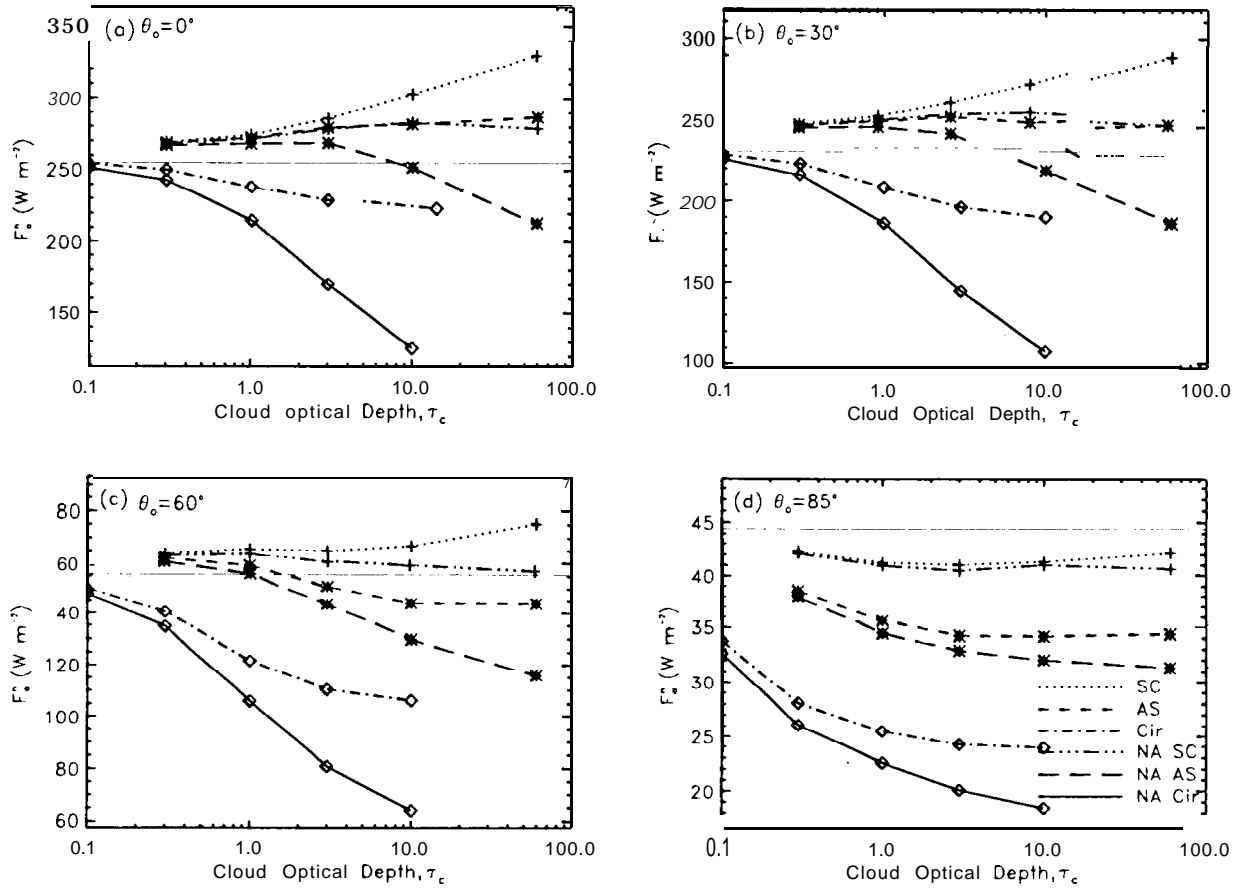


Figure 26. Solar zenith angle dependent absorption by the nominal clear atmosphere (thin solid line) and cloudy atmospheres with and without (NA) cloud liquid water or ice absorption. The solar zenith angles are (a) 0° , (b) 0° , (c) 0° , and (d) 85° .

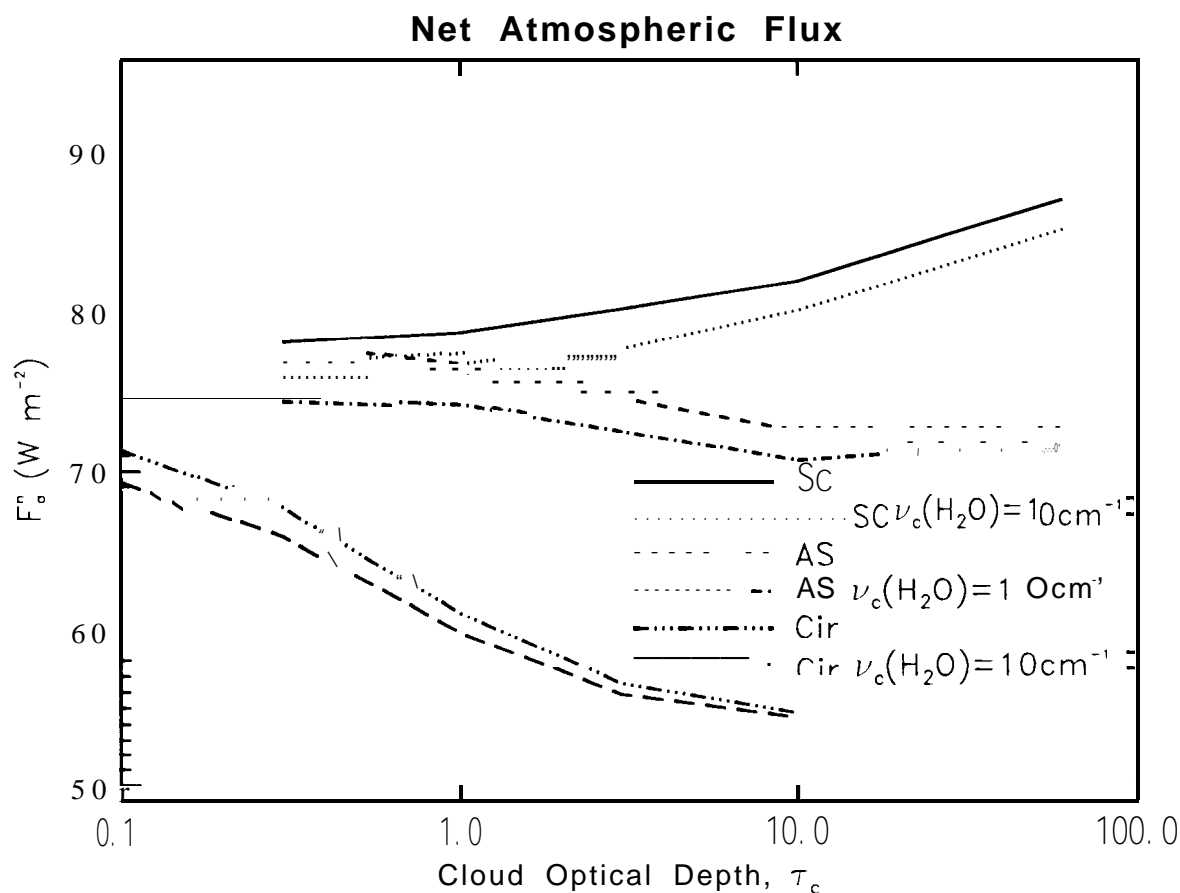


Figure 27. Column-integrated atmospheric absorption by cloudy atmospheres with and without water vapor far-wing continuum absorption for global-annual-average illumination conditions. The absorption by the nominal clear atmosphere is shown by thin solid horizontal line (74.5 W m^{-2}). The atmospheric absorption for stratocumulus (SC), altostratus (AS), and cirrus (Cir) clouds are shown. For the cases without water vapor continuum absorption, the water vapor lines were truncated 10 cm^{-1} from the line centers ($\nu_c(\text{H}_2\text{O})=10\text{cm}^{-1}$).

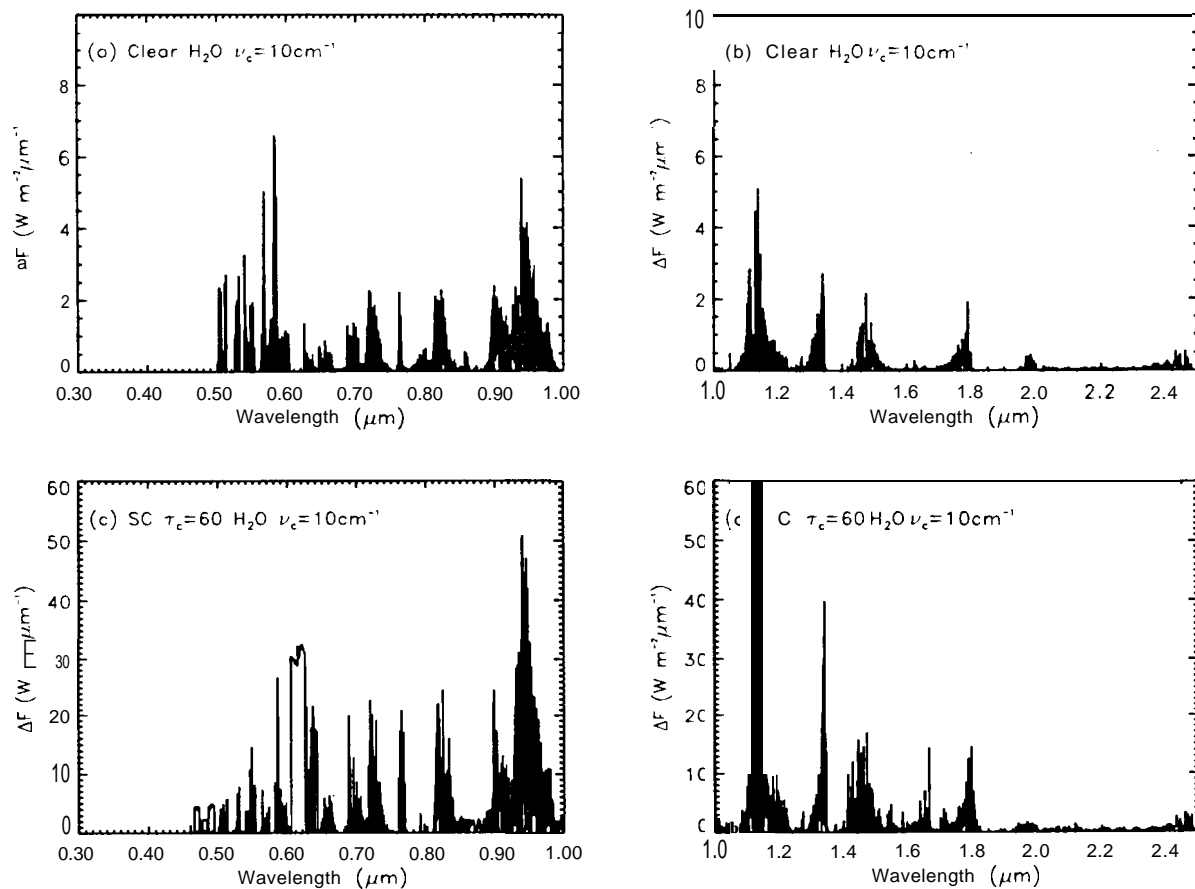


Figure 28. Differences between the reflected solar fluxes at the top of the atmosphere (Figure 9) and those obtained when the water vapor lines are truncated 10 cm^{-1} from the line centers. The solar zenith angle is 60° , and the spectral resolution is 2 cm^{-1} . Panels (a) and (b) show the top-of-atmosphere flux differences for a clear atmosphere with NILS water vapor mixing ratios. Panels (c) and (d) show the flux differences for an atmosphere with an optically-thick ($\tau_c = 60$) stratocumulus cloud.

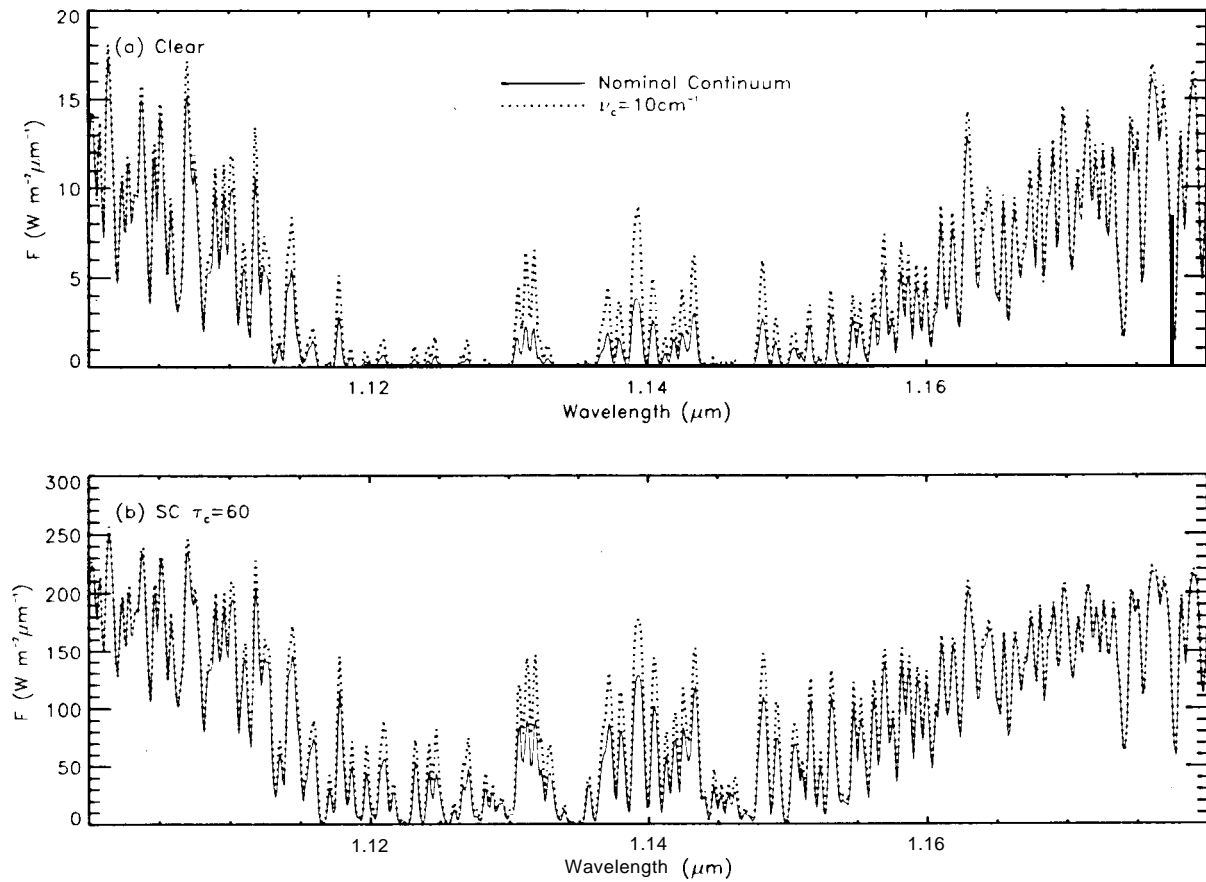


Figure 29. Reflected solar flux spectra at the top of (a) clear and (b) cloudy atmospheres for models with (solid) and without (dotted) far-wing water vapor continuum absorption. The solar zenith angle is 60° , and the spectral resolution is 2 cm^{-1} . For this band, the omission of far-wing absorption introduces the largest errors in micro-windows near the band center.

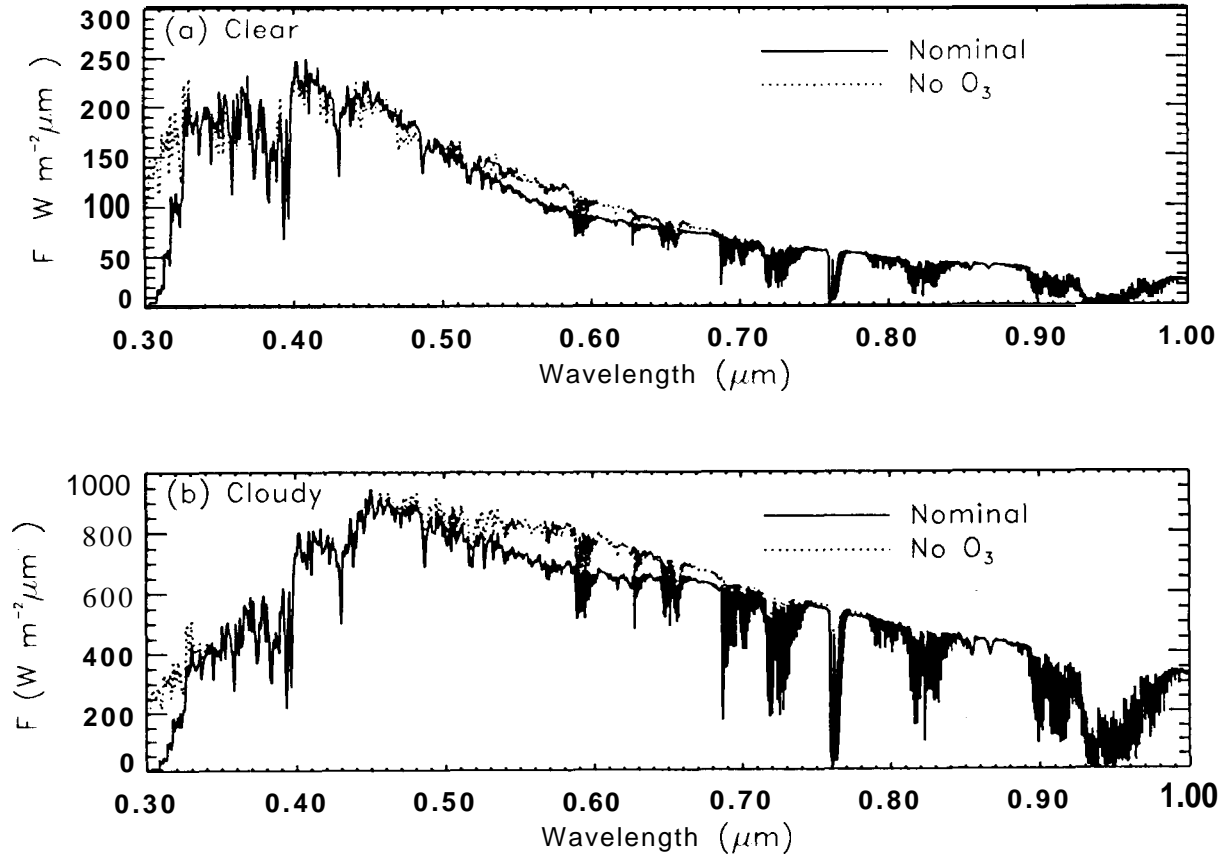


Figure 30. Reflected fluxes at the top of (a) clear and (b) cloudy atmospheres are shown with and without stratospheric ozone absorption. The solar zenith angle is 60° . The cloudy atmosphere includes a optically-thick ($\tau_c=60$) stratocumulus cloud deck at altitudes between 1 and 1.5 km. The nominal atmosphere uses the MLS ozone abundances (solid line), while the ozone has been omitted entirely from the “NO O_3 ” case (dotted line). The largest differences are seen in the weak Huggins bands near 0.3 μm , and the Chappuis bands centered near 0.6 μm . The flux differences are substantially larger in the cloudy case.

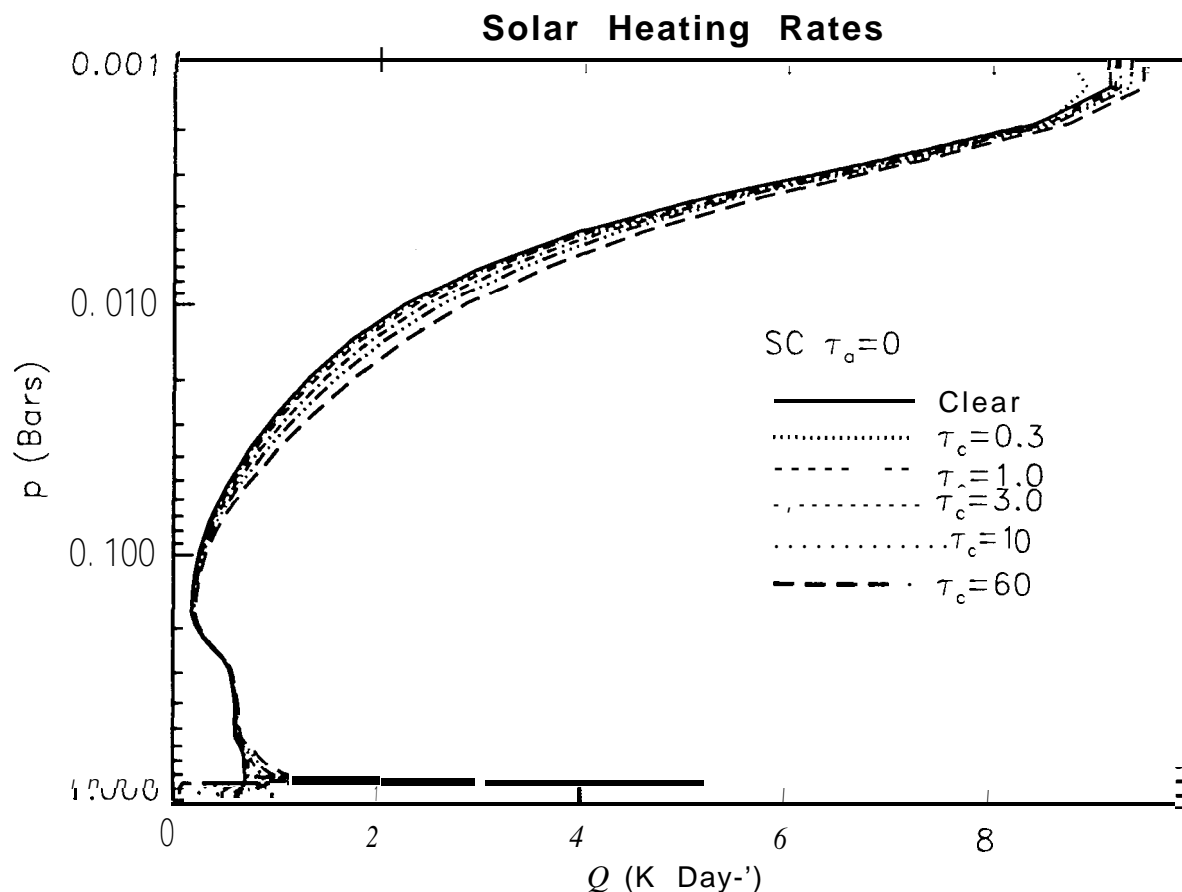


Figure 31. Solar heating rates as a function of pressure for clear and cloudy atmospheres with globally-averaged solar illumination conditions. The cloudy atmospheres include a single stratocumulus cloud deck at altitudes between 1 and 1.5 km with a range of optical thickness ($0.3 < \tau_c < 60$). The largest lower-stratospheric solar heating rates are obtained for the thickest clouds because these clouds reflect a larger fraction of the incident radiation back through the stratosphere for a second pass, where it can be absorbed by the weak Huggins and Chappuis bands.

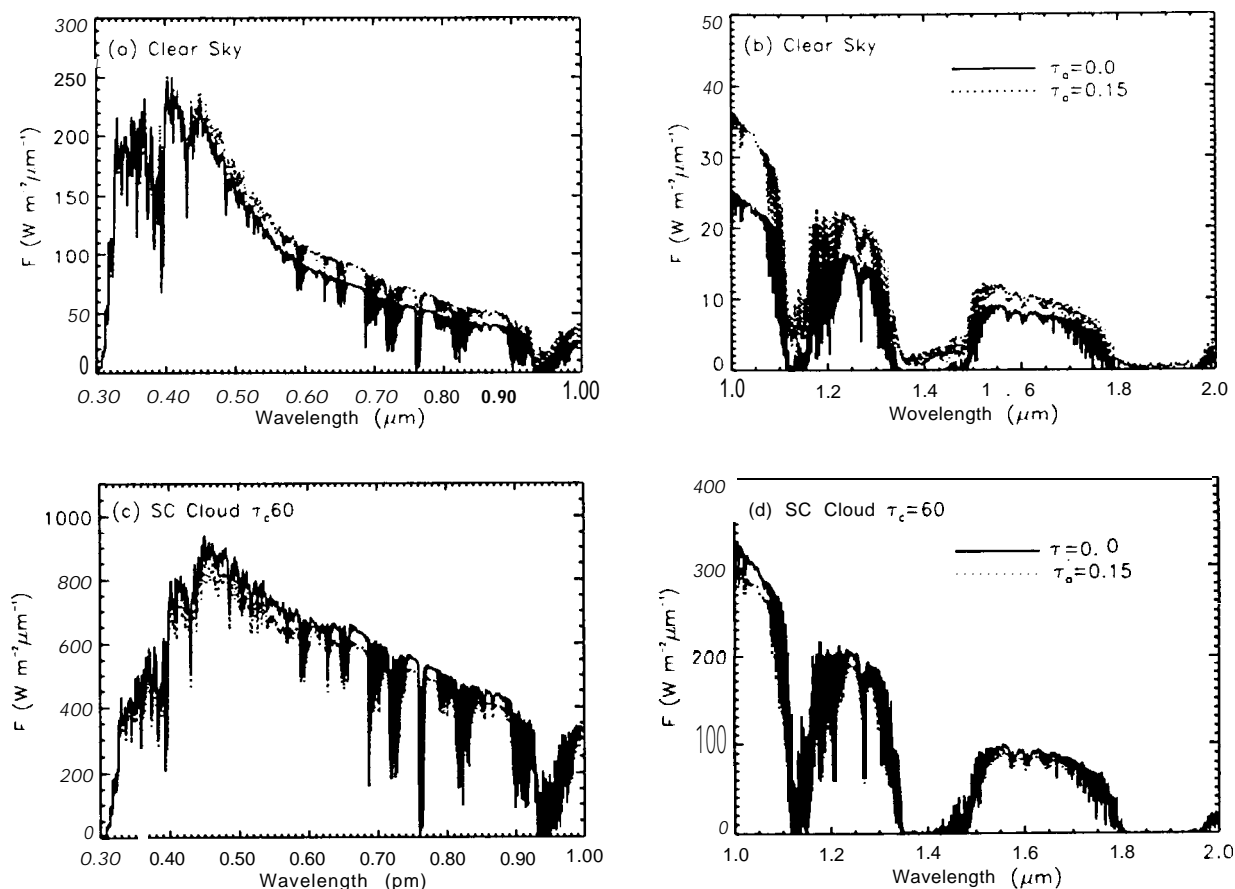


Figure 32. Computed upward solar flux spectra above clear and cloudy atmospheres for a solar zenith angle of 60° . The aerosol-laden atmospheres (dotted lines) have uniform number densities at tropospheric levels (pressures greater than 0.2 bars), column-integrated aerosol optical depths, $\tau_a(0.5\mu\text{m})=0.15$, and single scattering albedos, $\omega(0.5\mu\text{m})\sim 0.9$. The cloud-free cases shown in panels (a) and (b) have nominal MLS gas mixing ratios and surface albedos for a moderately-rough ocean (Figure 8). The cloudy atmospheres in panels (c) and (d) include a single, optically-thick ($\tau_c(0.5\mu\text{m})=60$) stratocumulus (SC) cloud at altitudes between 1 and 1.5 km that is saturated with water vapor. Even though these aerosols enhance the albedos in clear skies over dark surfaces, they decrease the albedos over cloudy regions.

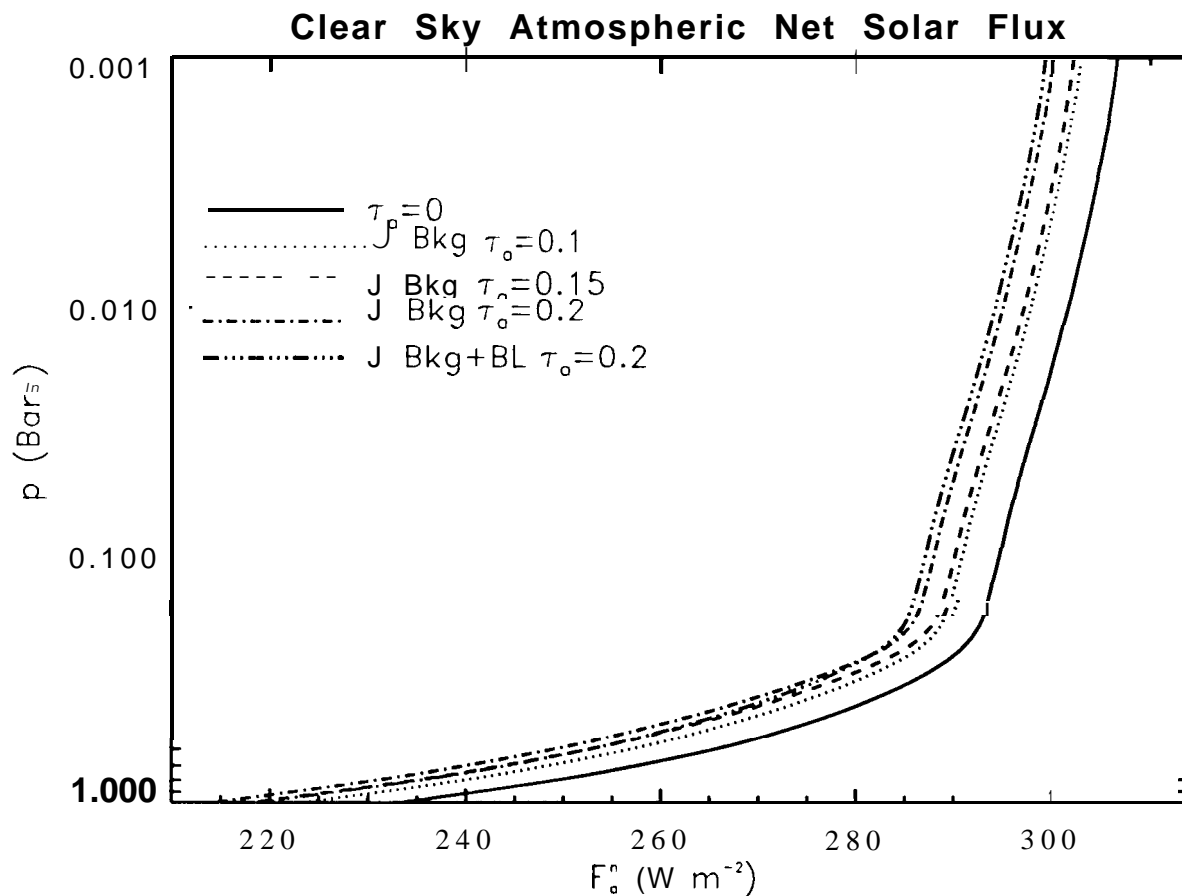


Figure 33. Spectrally-integrated clear-sky net solar fluxes for an aerosol-free atmosphere (solid line) are compared to those obtained for aerosol-laden atmospheres for global-annual-average solar illumination conditions and a relatively-dark ocean surface. The aerosol-laden cases include the nominal, uniformly-mixed Jaenicke Background aerosols (J Bkg) with column-integrated optical depths between 0.1 and 0.2, and solar-averaged single scattering albedos near 0.9. Another case includes a combination of uniformly-mixed Jaenicke Background aerosols ($\tau_a=0.1$) along with equal amounts of the mostly conservative boundary layer aerosols (J Bkg + BL), which are confined near the surface (particle scale height, $H < 1$ km). These aerosol distributions are described in greater detail in the text.

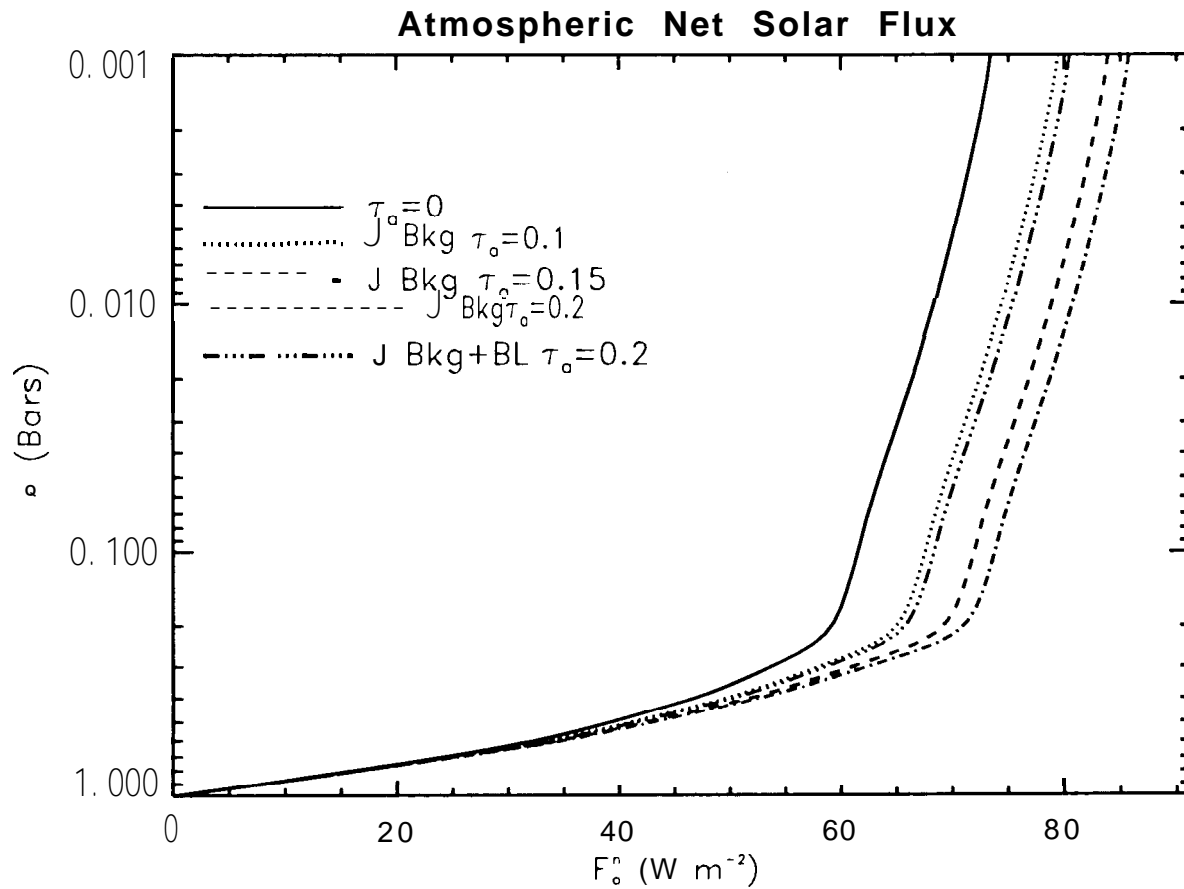


Figure 34. Spectrally-integrated clear-sky atmospheric net solar flux profiles for global-annual-average illumination conditions and the range of aerosol loadings described in Figure 33. Even though aerosols reduce the absorption by the surface-atmosphere system in clear skies over dark surfaces, they can increase the absorption by the atmosphere.

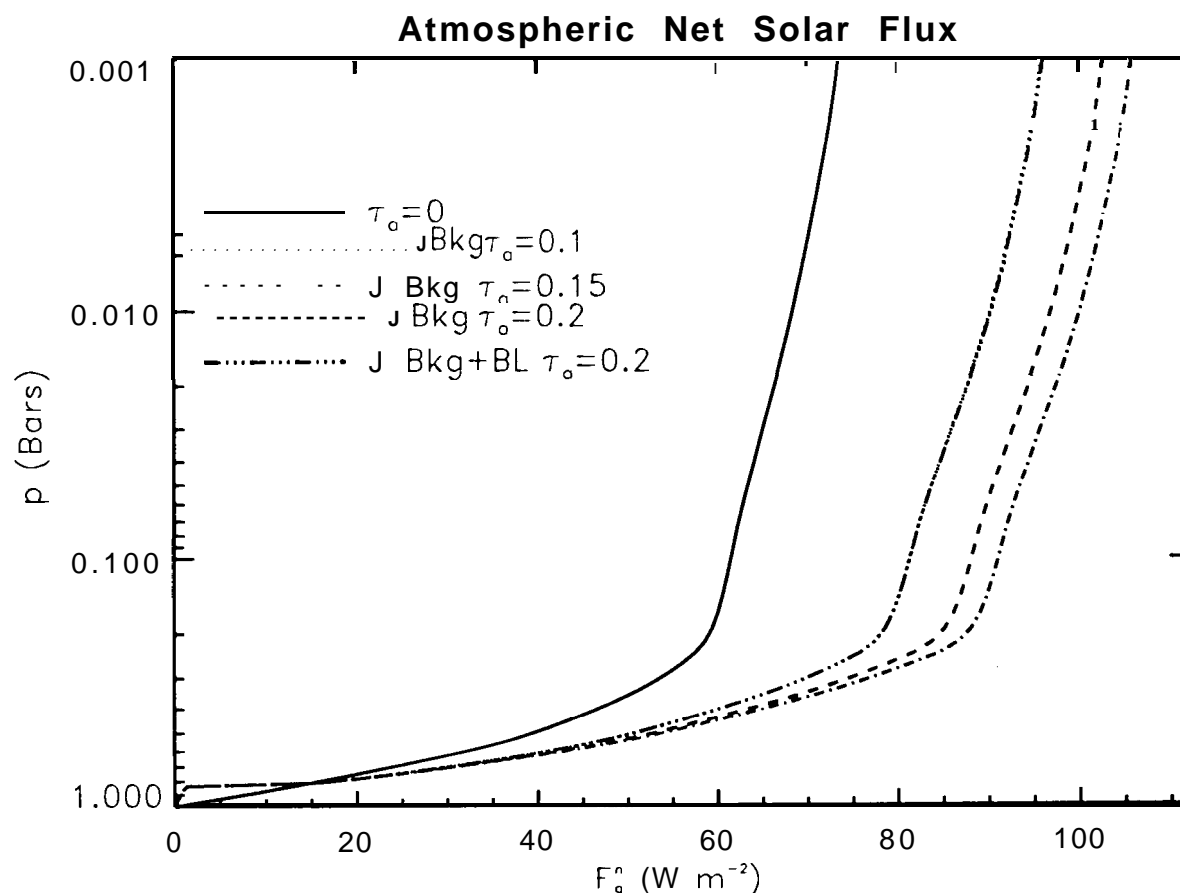


Figure 35. The spectrally-integrated, global-annual-average atmospheric net flux profile for the nominal, aerosol-free, clear atmosphere (solid line) is compared to those obtained for aerosol-laden atmospheres that include a single, optically-thick ($\tau_c=60$) stratocumulus cloud deck and the range of aerosol loadings described in Figure 33. The absorption of the incident and reflected sunlight by optically-thin, weakly-absorbing aerosols above the tops of optically-thick low clouds can produce large enhancements in the atmospheric absorption.

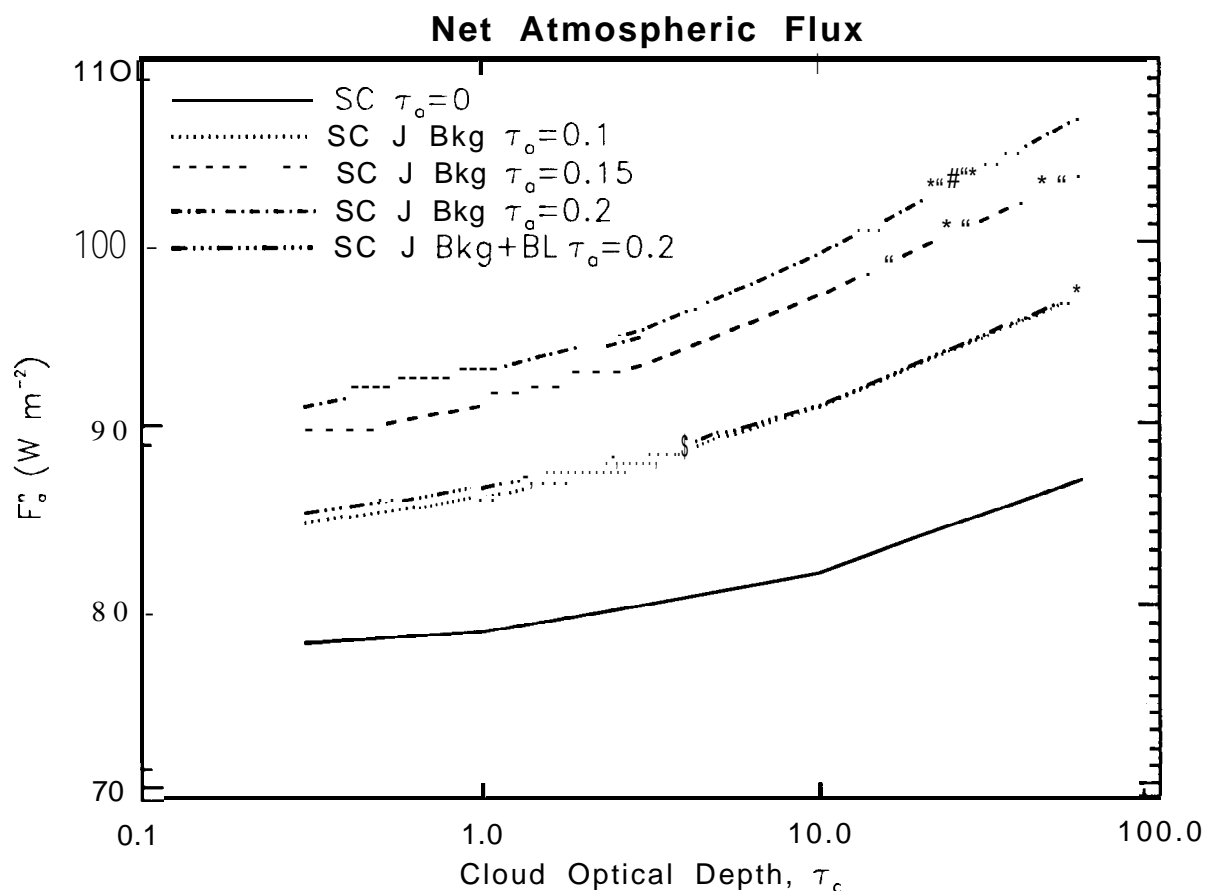


Figure 36. Column-integrated atmospheric absorption for the aerosol-laden atmospheres described in Figure 33 are compared to that of the nominal, cloud-free, aerosol-free atmosphere (solid line at 74.51 W m^{-2}). Each cloudy atmosphere includes a single stratocumulus cloud deck between 1.0 and 1.5 km altitude. The boundary layer aerosols considered here (J Bkg+BL) contribute little to the atmospheric absorption because they have single scattering albedos near unity.

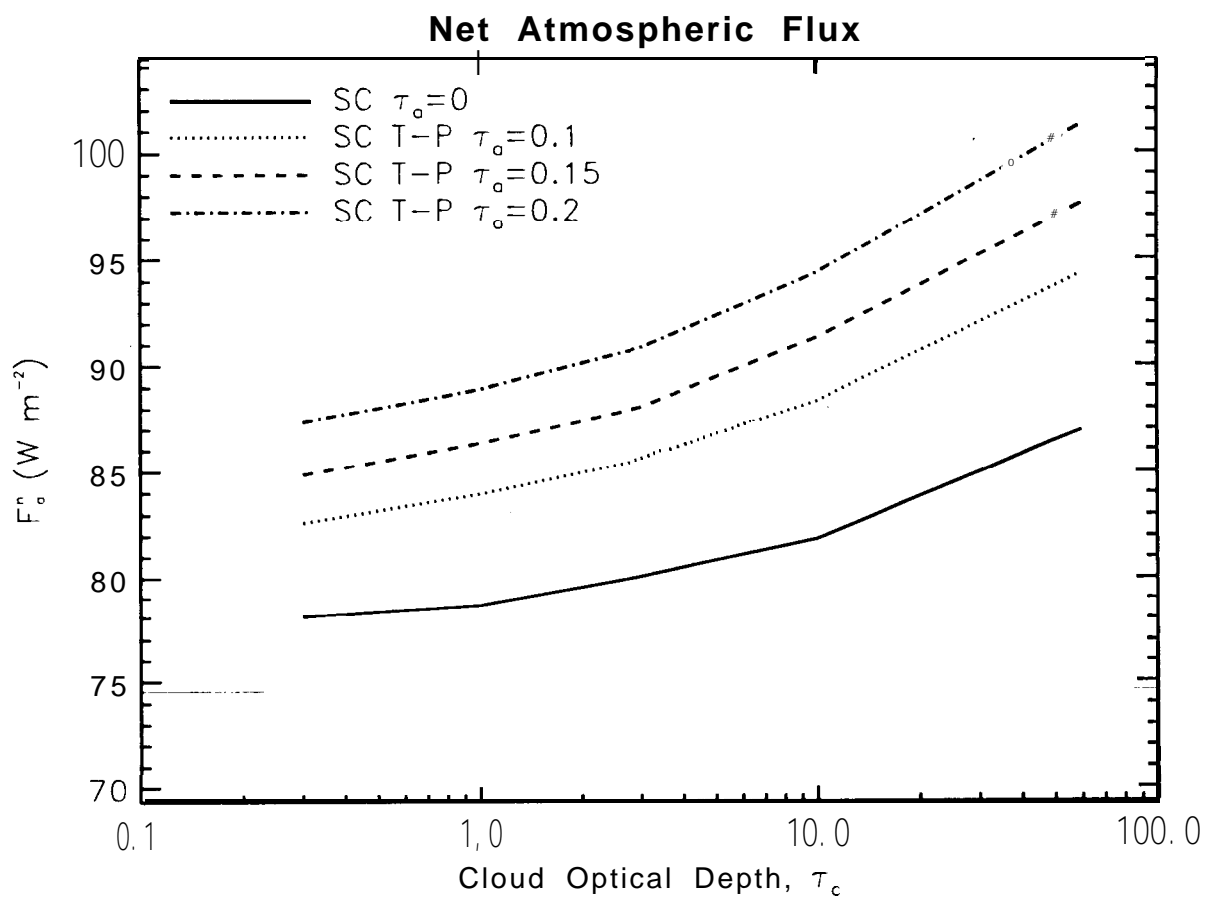


Figure 37. Same as Figure 36 for the somewhat more weakly absorbing Toon-Pollack aerosols.

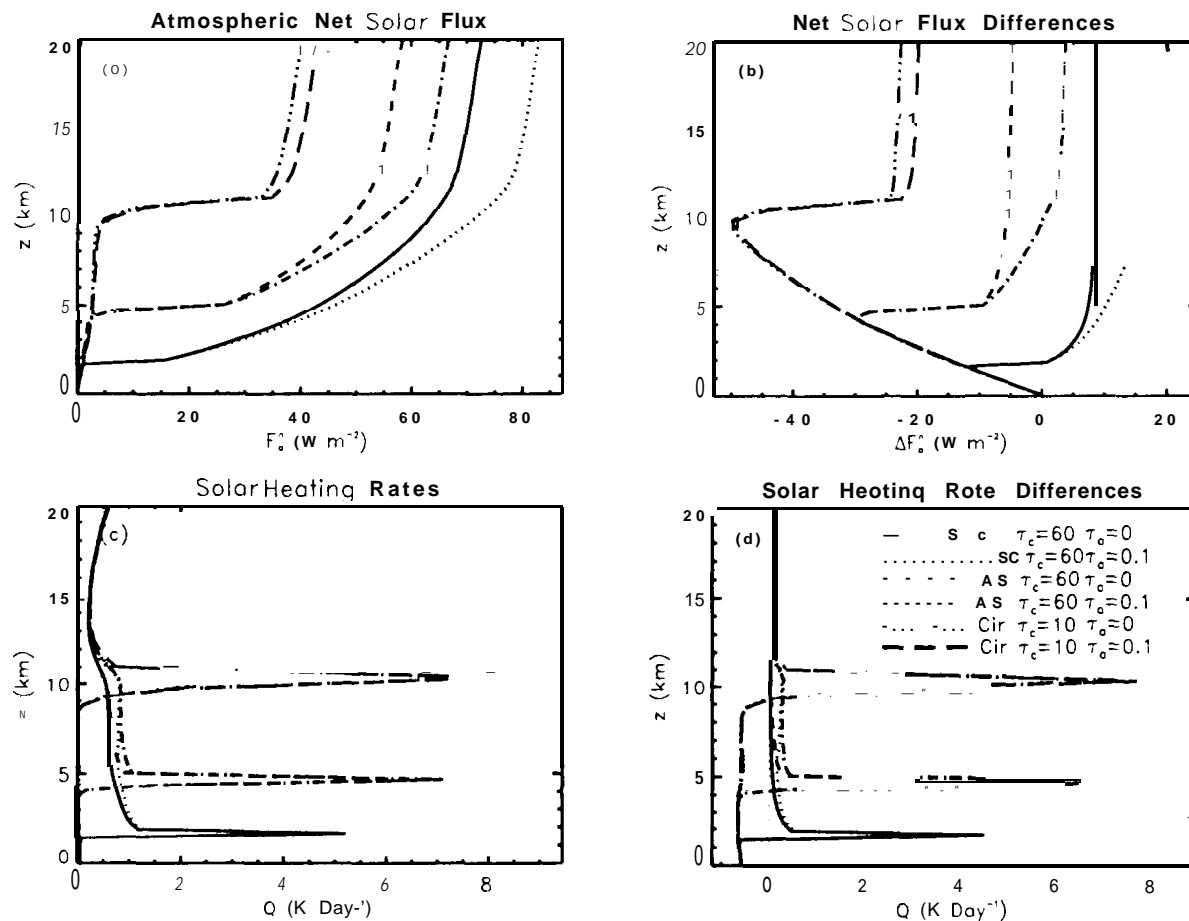


Figure 38. Solar flux and heating rate profiles for aerosol-free and aerosol-laden atmospheres with optically-thick stratocumulus (SC), altostratus (AS), and cirrus (Cir) clouds. The aerosol-laden atmospheres have uniformly-mixed aerosols with the nominal Jaenicke background aerosol size distribution, and column-integrated optical depths near 0.1 at $0.5\mu\text{m}$. Global-annual-average illumination conditions are used. (a) Altitude-dependent atmospheric net solar fluxes for cloudy atmospheres with and without aerosols. (b) Differences between the atmospheric net fluxes for the cloudy cases shown in panel (a) and the nominal, aerosol-free clear atmosphere with MLS gas mixing ratios. Aerosols increase the absorption between the cloud top and the tropopause ($\sim 12\text{ km}$), but produce negligible changes at levels within or below the clouds. (c) Solar heating rates for cloudy atmospheres with and without aerosols. (d) Differences between the cloudy-sky solar heating rates shown in panel (c) and those obtained for the nominal, aerosol-free clear atmosphere.

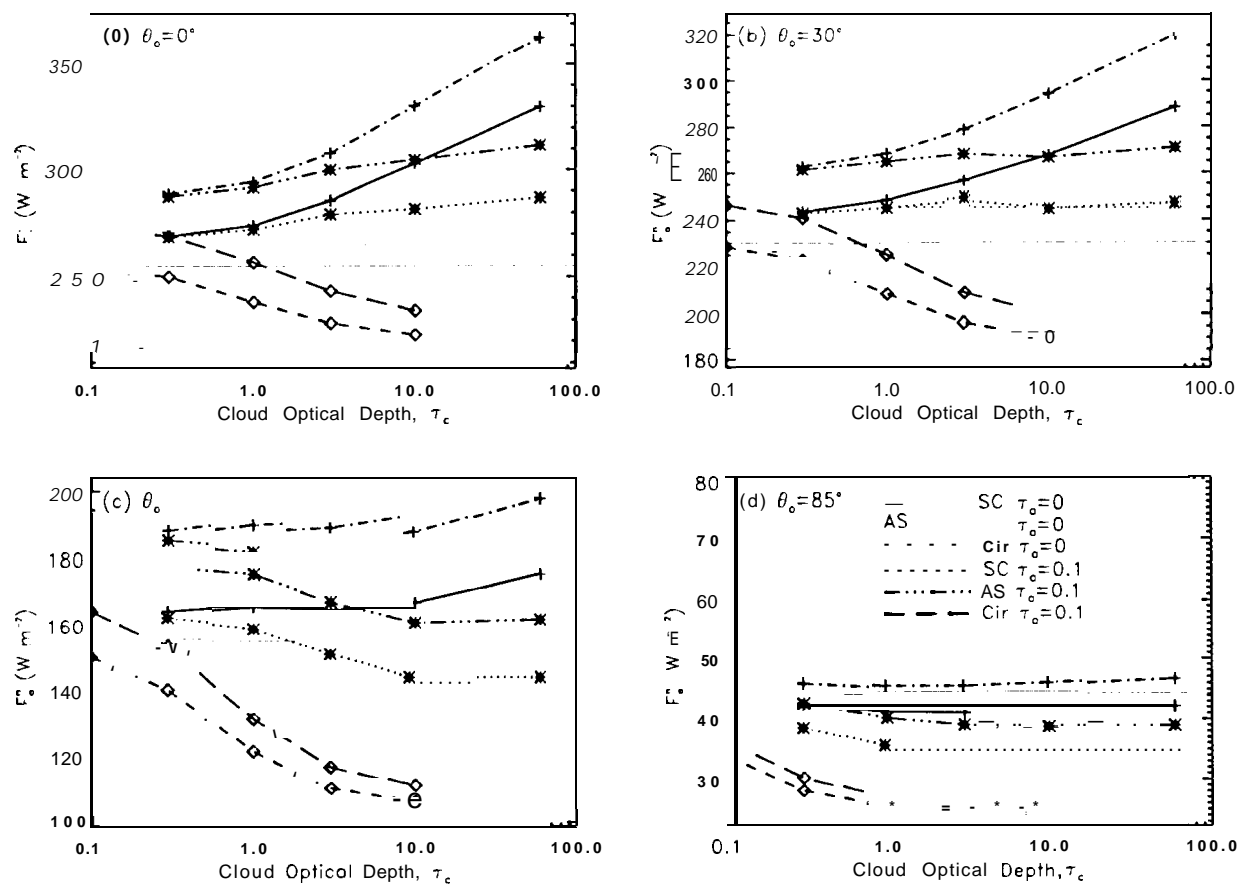


Figure 39. Column-integrated atmospheric absorption for the atmospheres described in Figure 38 are shown as a function of cloud optical depth, τ_c , and solar zenith angle, θ_0 . Results for the nominal, cloud-free, aerosol-free atmosphere are shown as a thin solid horizontal line. The solar zenith angles are (a) 0° , (b) 30° , (c) 60° , and (d) 85° .

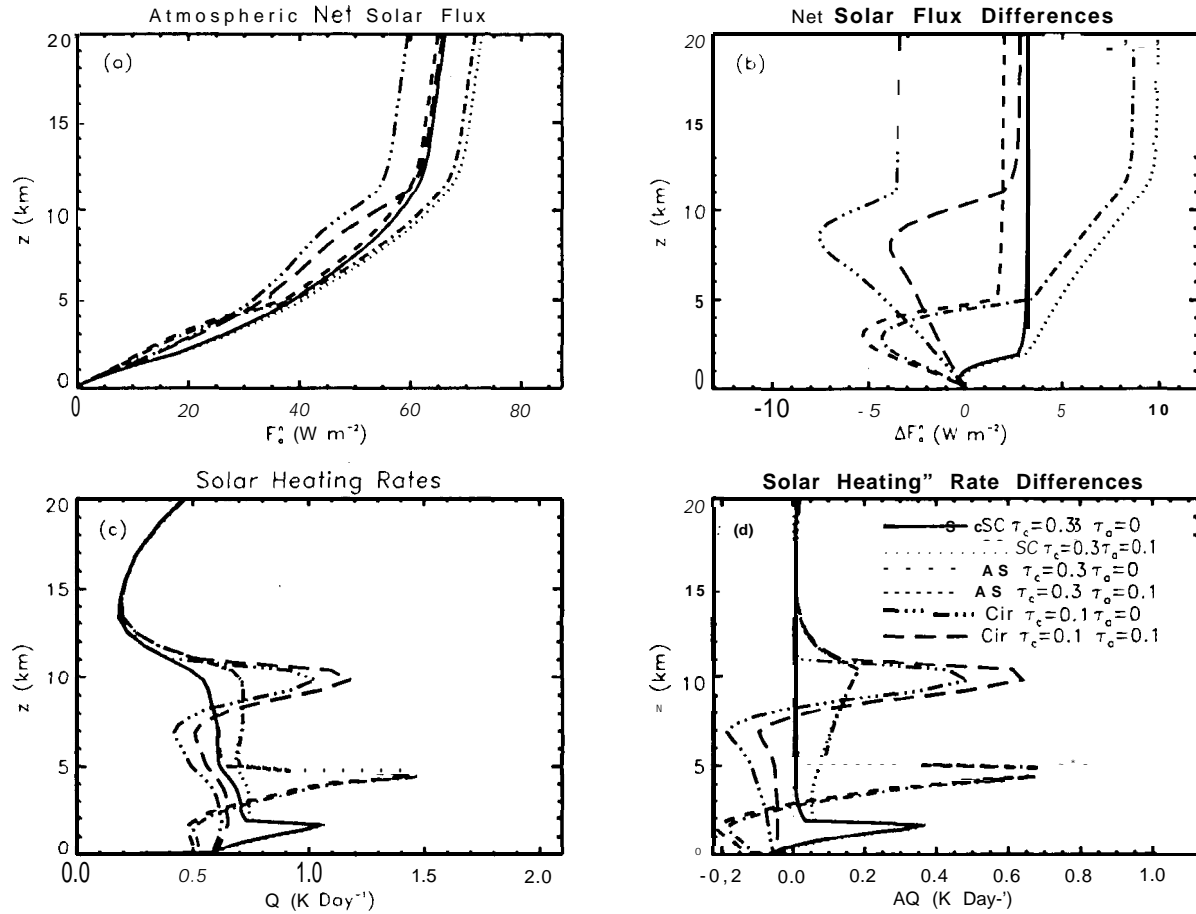


Figure 40. Solar fluxes and heating rates for aerosol-free and aerosol-laden atmospheres with optically-thin stratocumulus (SC), altostratus (AS), and cirrus (Cir) clouds. The aerosol-laden atmospheres have uniformly-mixed aerosols with the nominal Jaenicke background aerosol size distribution, and column-integrated optical depths near 0.1 at $0.5\mu\text{m}$. Global-annual-average illumination conditions are used. (a) Altitude-dependent atmospheric net solar fluxes for cloudy atmospheres with and without aerosols. (b) Differences between the atmospheric net fluxes for the cloudy cases shown in panel (a) and the nominal, aerosol-free clear atmosphere with MLS gas mixing ratios. In atmospheres occupied by optically-thin clouds, aerosols can enhance the absorption of sunlight above, within, and below the cloud deck. Also, in aerosol-laden atmospheres, thin cirrus clouds can produce a positive solar radiative forcing, while these clouds produce a strong negative forcing in aerosol-free atmospheres. (c) Solar heating rates for cloudy atmospheres with and without aerosols. (d) Differences between the cloudy-sky solar heating rates shown in panel (c) and those obtained for the nominal, aerosol-free clear atmosphere.

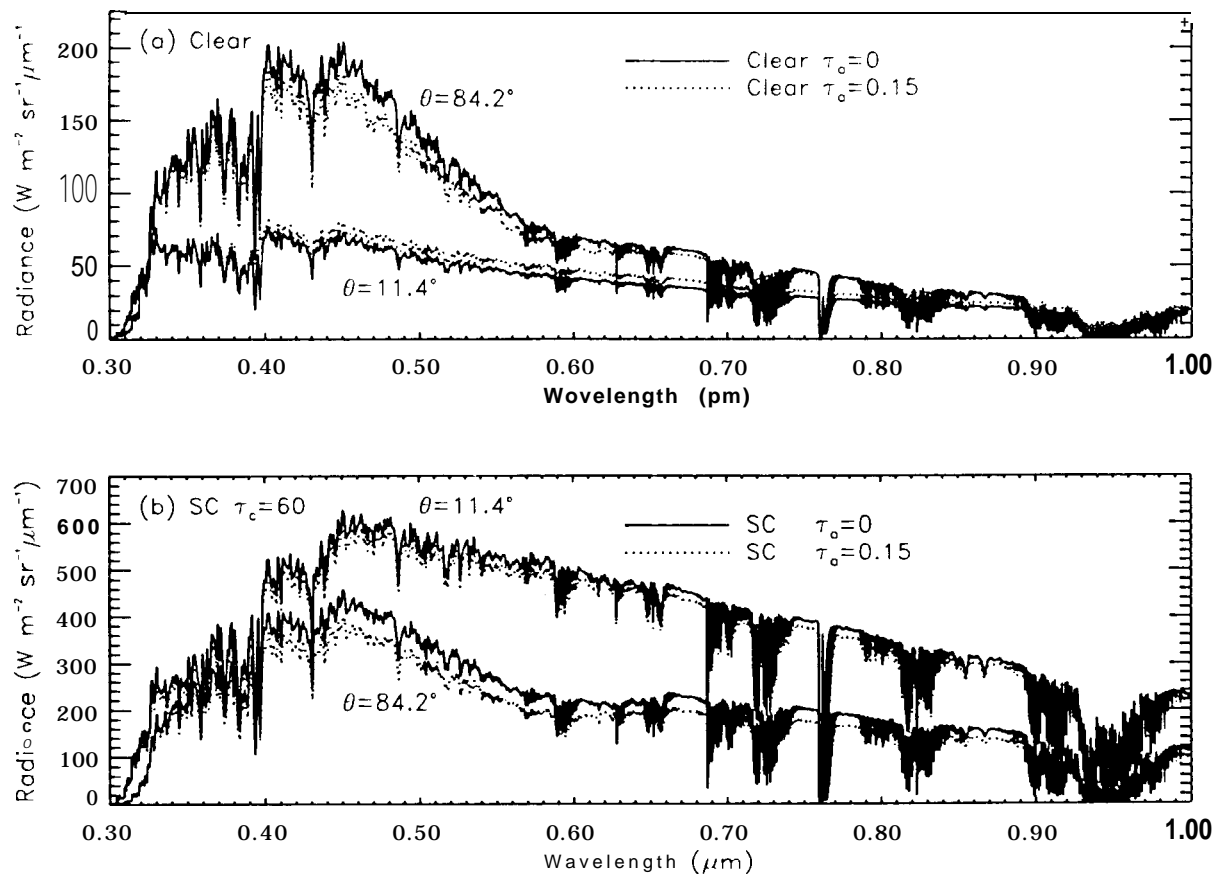


Figure 41. Reflected radiances at the top of the atmosphere are shown as a function of emission zenith angle for clear and cloudy atmospheres with and without aerosols. The sun is at the zenith and the nominal dark ocean albedos are used for all cases shown here. The aerosol-laden atmospheres have uniformly-mixed aerosols with the nominal Jaenicke background aerosol size distribution, and column-integrated optical depths near 0.15 at $0.5 \mu\text{m}$. (a) In cloud-free skies over dark surfaces with the sun at the zenith, Rayleigh scattering enhances the reflected radiances at the larger emission zenith angles. For these conditions, aerosols produce modest increases in the reflected radiances at emission zenith angles less than 20° , but they attenuate the reflected radiation at the largest emission zenith angles ($\theta > 80^\circ$). (b) The cloudy atmospheres include a single, optically-thick ($\tau_c=60$) stratocumulus cloud at altitudes between 1.0 and 1.5 km. In cloudy skies, weakly-absorbing aerosols attenuate the reflected sunlight at all emission angles.

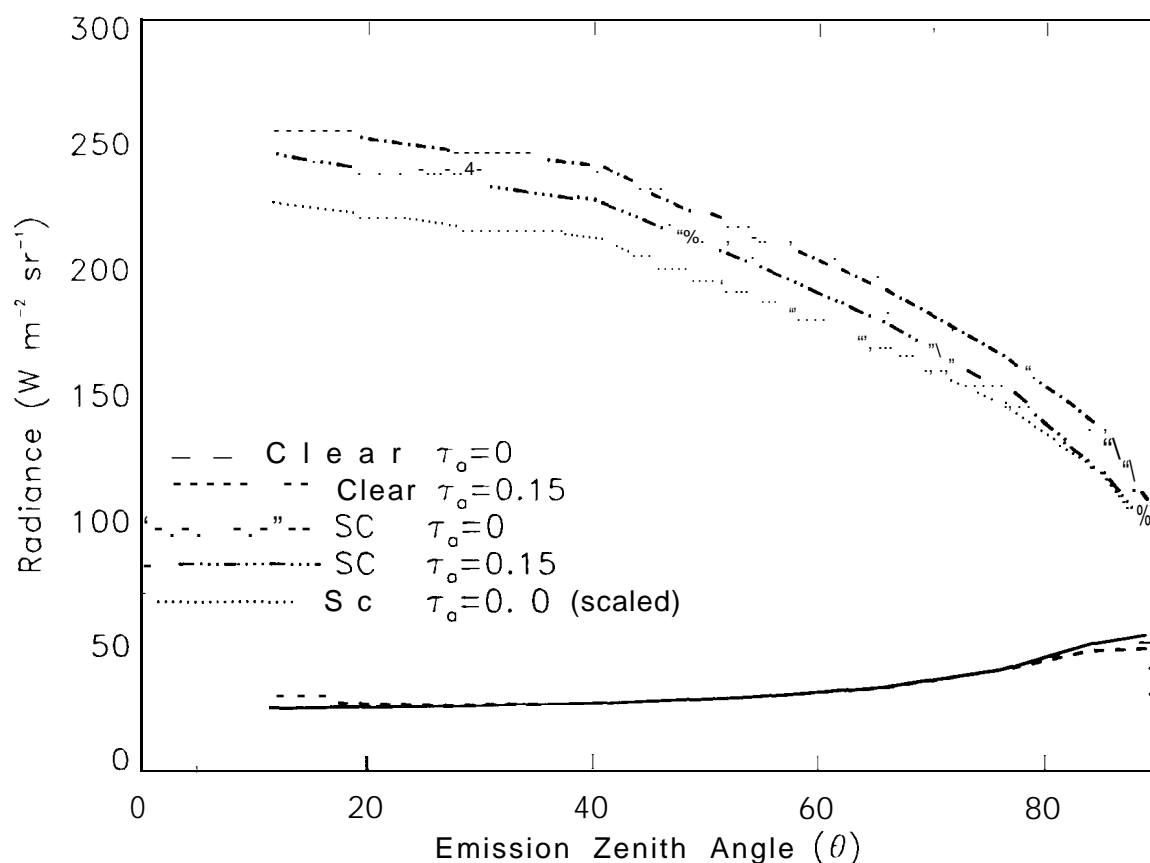


Figure 42. Reflected radiances shown in Figure 41 were integrated over the wavelength range, 0.3 to $1.0\mu\text{m}$ and displayed as a function of emission zenith angle for clear and cloudy atmospheres with and without aerosols. In clear skies, weakly absorbing aerosols increase the reflected radiance at small emission angles because they are much brighter than the underlying dark surface. However, at the largest emission angles, where Rayleigh scattering dominates, these aerosols can reduce the intensity of the reflected radiation. In atmosphere occupied by optically-thick clouds, aerosol absorption above the cloud tops attenuates the reflected sunlight at all emission angles, but a larger fraction of the radiation reflected into the largest zenith angles is absorbed by these aerosols. The thin dotted line shows the effect of scaling the radiances reflected by the aerosol-free atmosphere ($\text{SC } \tau_a=0$) by a constant factor (0.877) such that they matched the results for the aerosol laden atmosphere at the largest emission angle. If the aerosol absorption was independent of the emission angle, this dotted curve would lie along the results for the aerosol-laden atmosphere (dash-dot-dot-dot).

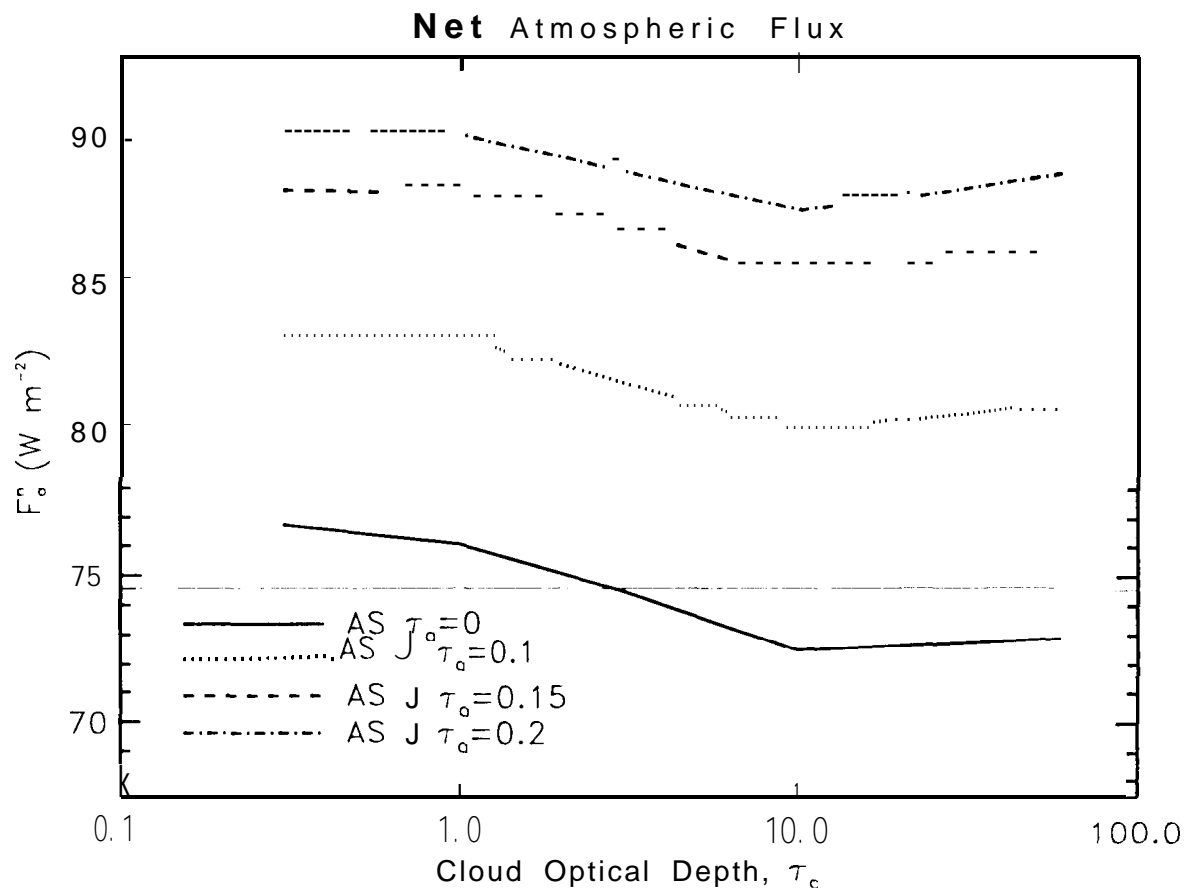


Figure 43. Column-integrated atmospheric absorption in cloudy, aerosol-laden atmospheres for global-annual-average illumination conditions. Each cloudy atmosphere includes a single altostratus (.4S) cloud deck with $0.5 \mu\text{m}$ optical depths between 0.3 and 60 at altitudes between 3.6 and 4.8 km. The aerosol-laden atmospheres have uniformly-mixed aerosols with the nominal Jaenicke size distribution (Figures 1 and 2), and column-integrated optical depths between 0.1 and 0.2 at $0.5 \mu\text{m}$. About half of the aerosol column extends above the cloud tops. Results for the nominal, cloud-free, aerosol-free atmosphere are shown as a thin, solid, horizontal line (74.5 W m^{-2}).

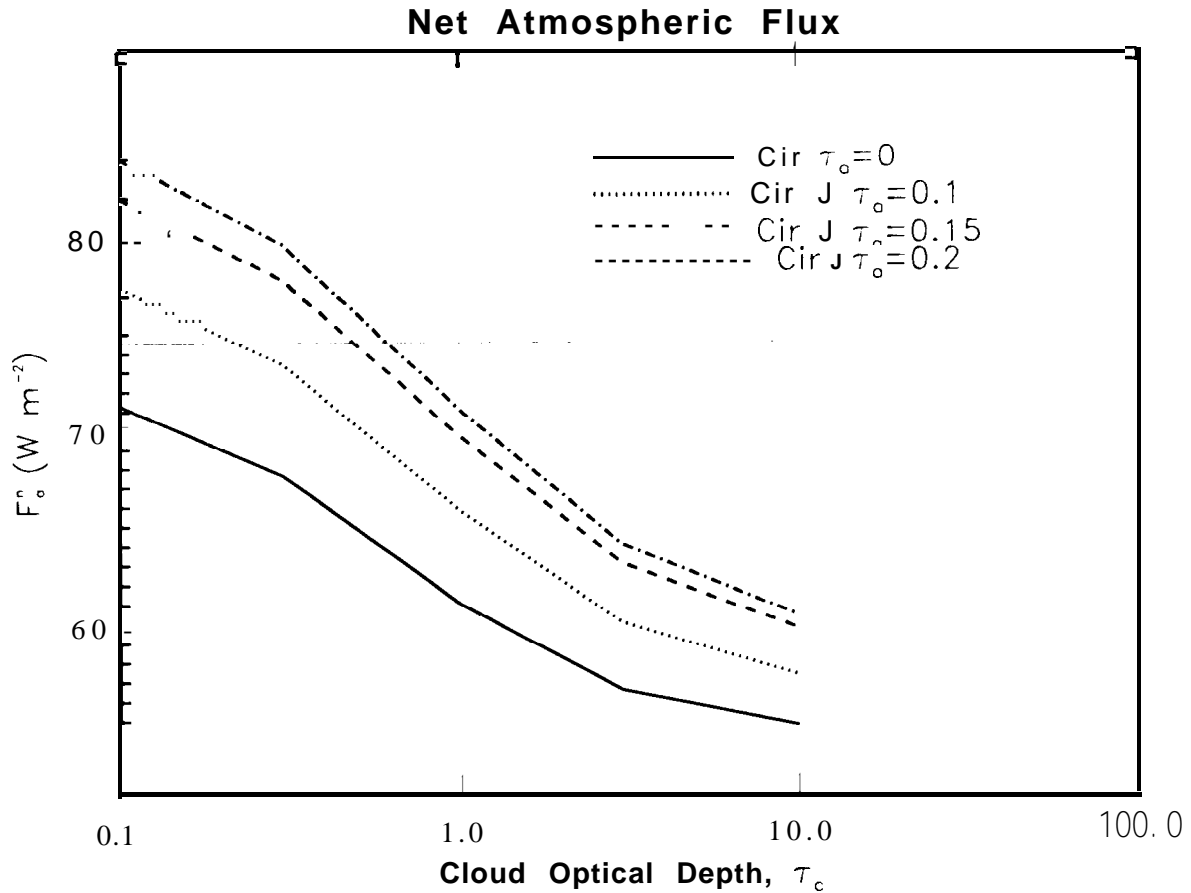


Figure 44. Column-integrated atmospheric absorption in cloudy, aerosol-laden atmospheres for global-annual-average illumination conditions. Each cloudy atmosphere includes a single cirrus cloud deck with $0.5 \mu\text{m}$ optical depths between 0.3 and 60 at altitudes between 7 and 10 km. The aerosol-laden atmospheres have uniformly-mixed aerosols with the nominal Jaenicke size distribution (Figures 1 and 2), and column-integrated optical depths between 0.1 and 0.2 at $0.5 \mu\text{m}$. Less than 20% of the aerosol column extends above the cloud tops. Results for the nominal, cloud-free, aerosol-free atmosphere are shown as a thin, solid, horizontal line (74.51 W m^{-2}).

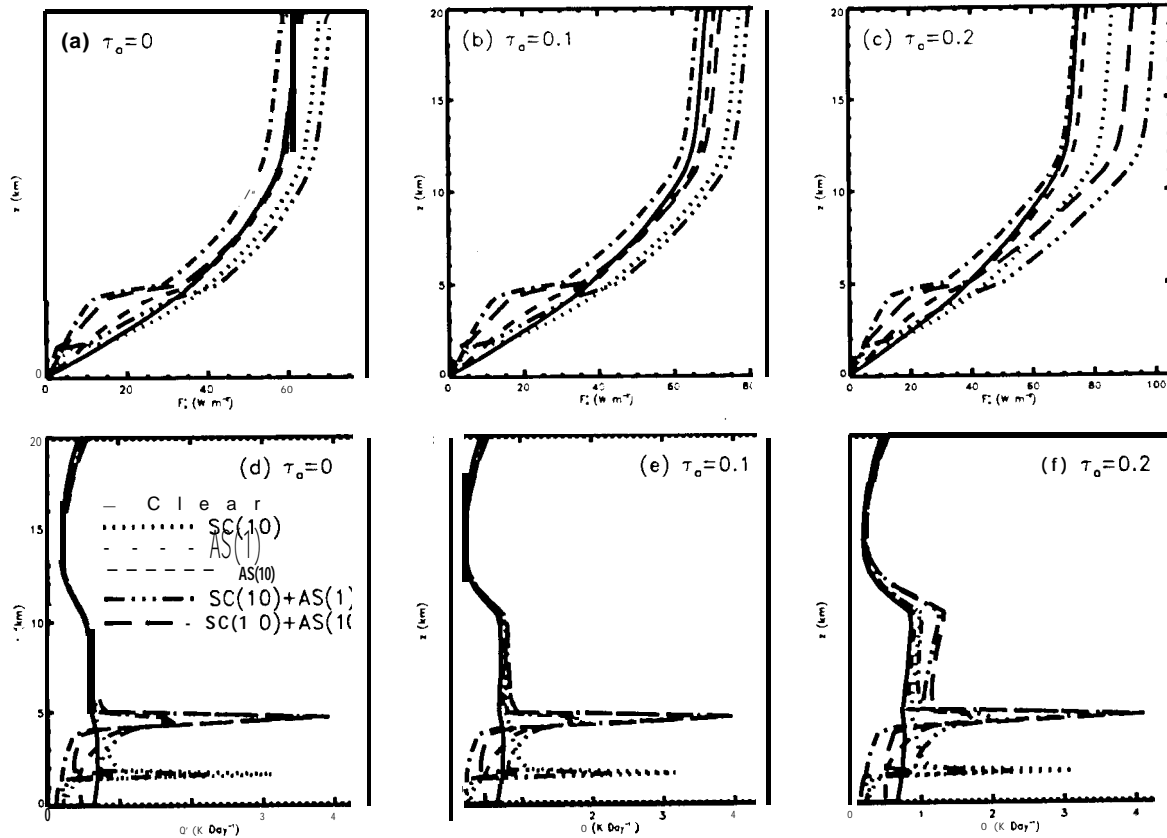


Figure 45. Atmospheric net fluxes and heating rates for atmospheres with isolated or overlapping stratocumulus (SC) and alto-stratus (AS) clouds. Global-annual-average illumination conditions were used. The cloud types include moderately thick ($\tau_c=10$) SC clouds (SC(10)), moderately-thick ($\tau_c=10$) AS clouds (AS(10)), optically-thin ($\tau_c=1$) AS clouds (AS(1)), and “cloud sandwiches” composed of SC clouds with optically-thick AS clouds (SC(10)+AS(10)), or optically-thin AS clouds (SC(10)+AS(1)). Results for aerosol free and aerosol-laden atmospheres are shown. The aerosol laden atmospheres have constant particle number densities below 12 km (0.2 Bars), the nominal aerosol size distribution, and $0.5\mu\text{m}$ optical depths of 0.1 or 0.2. (a) Atmospheric net solar flux distributions in clear and cloudy aerosol-free atmospheres. (b) same as (a) for aerosol-laden atmospheres with column-integrated aerosol optical depths, $\tau_a=0.1$. (c) Same as (b) for $\tau_a=0.2$. (d) Solar heating rates in clear and cloudy aerosol-free atmospheres. (e) Same as (d) for aerosol-laden atmospheres with $\tau_a=0.1$. (f) Same as (e) for aerosol-laden atmospheres with $\tau_a=0.2$.

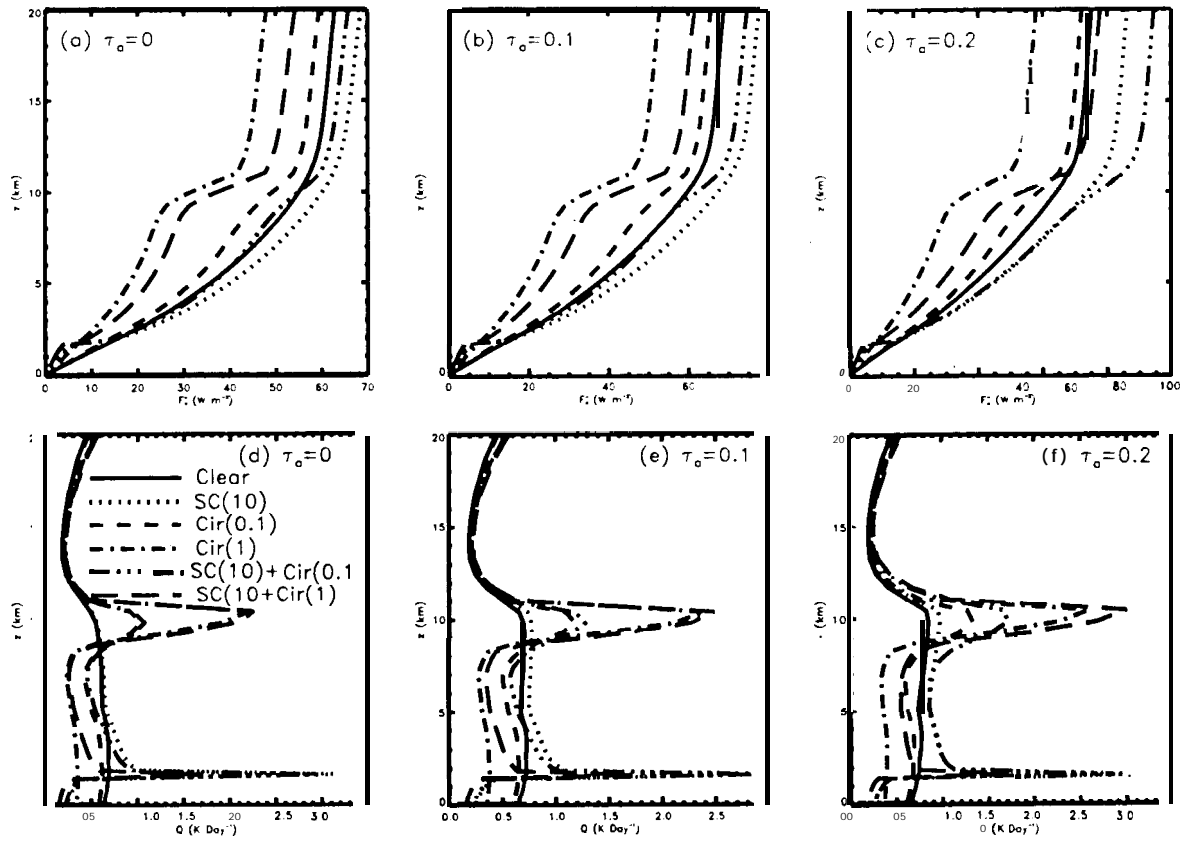


Figure 46. Atmospheric net fluxes and heating rates are shown as functions of altitude in clear atmospheres and atmospheres with isolated or overlapping stratocumulus (SC) and cirrus (Cir) clouds. Global-annual-average illumination conditions were used. The cloud types include moderately thick ($\tau_c=1.0$) SC clouds (SC(10)), moderately-thick ($\tau_c=1$) Cir clouds (Cir(1)), optically-thin ($\tau_c=0.1$) Cir clouds (Cir(0.1)), and “cloud sandwiches” composed of SC clouds with optically-thick Cir clouds (SC(10)+Cir(1)), or optically-thin Cir clouds (SC(10)+Cir(0.1)). Results for aerosol free and aerosol-laden atmospheres are shown (see Figure 45). (a) Atmospheric net solar flux distributions in clear and cloudy aerosol-free atmospheres. (b) same as (a) for aerosol-laden atmospheres with column-integrated aerosol optical depths, $\tau_a=0.1$. (c) Same as (b) for $\tau_a=0.2$. (d) Solar heating rates in clear and cloudy aerosol-free atmospheres. (e) Same as (d) for aerosol-laden atmospheres with $\tau_a=0.1$. (f) Same as (e) for aerosol-laden atmospheres with $\tau_a=0.2$.

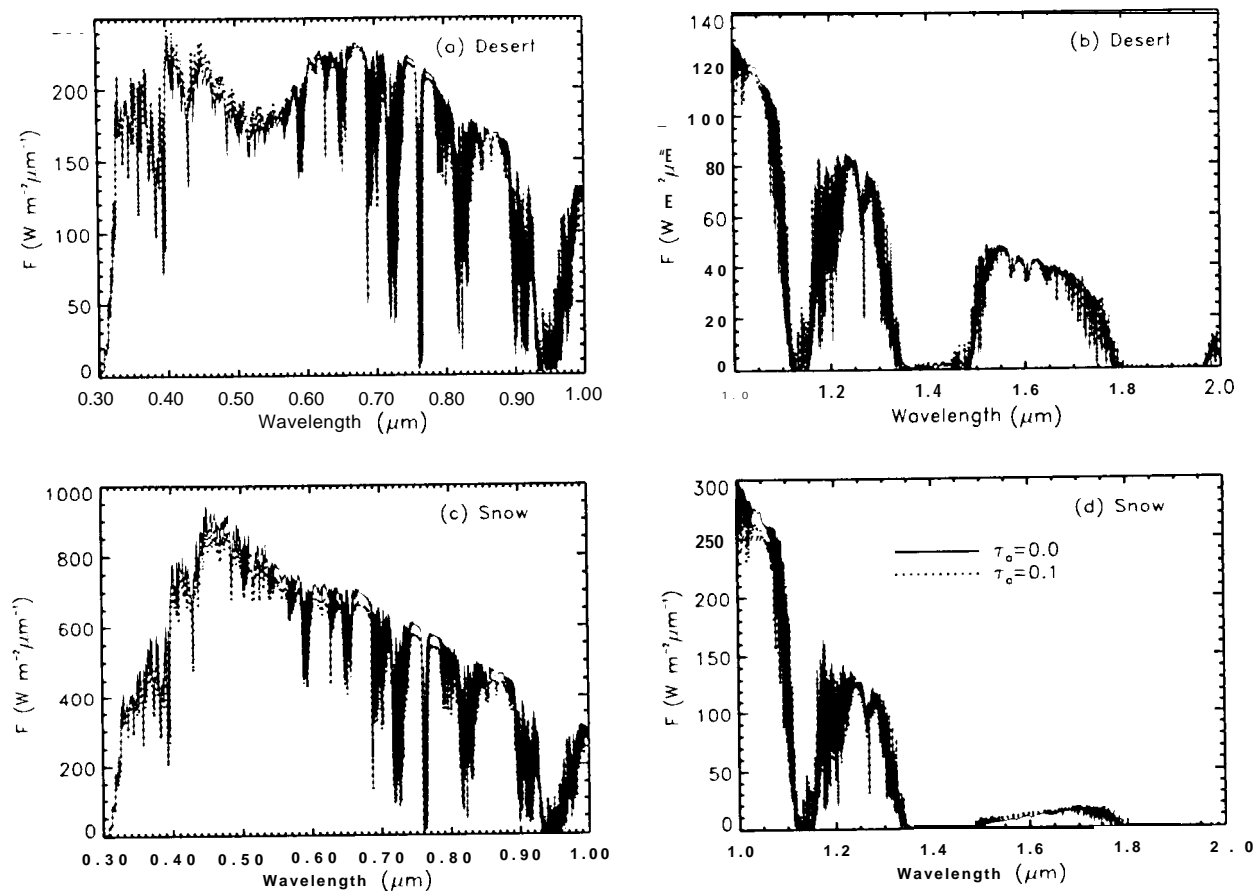


Figure 47. Upward solar fluxes at the top of the atmosphere are shown for clear atmospheres above desert (panels a and b) and snow (panels c and d) covered surfaces (Figure 8). The solar zenith angle is 60 degrees. Results for aerosol free (solid line) and aerosol-laden (dotted line) atmospheres are shown. The aerosol laden atmospheres have constant particle number densities at altitudes below 12 km (0.2 Bars), the nominal Jaenicke aerosol size distribution, and column-integrated optical depths of 0.15.

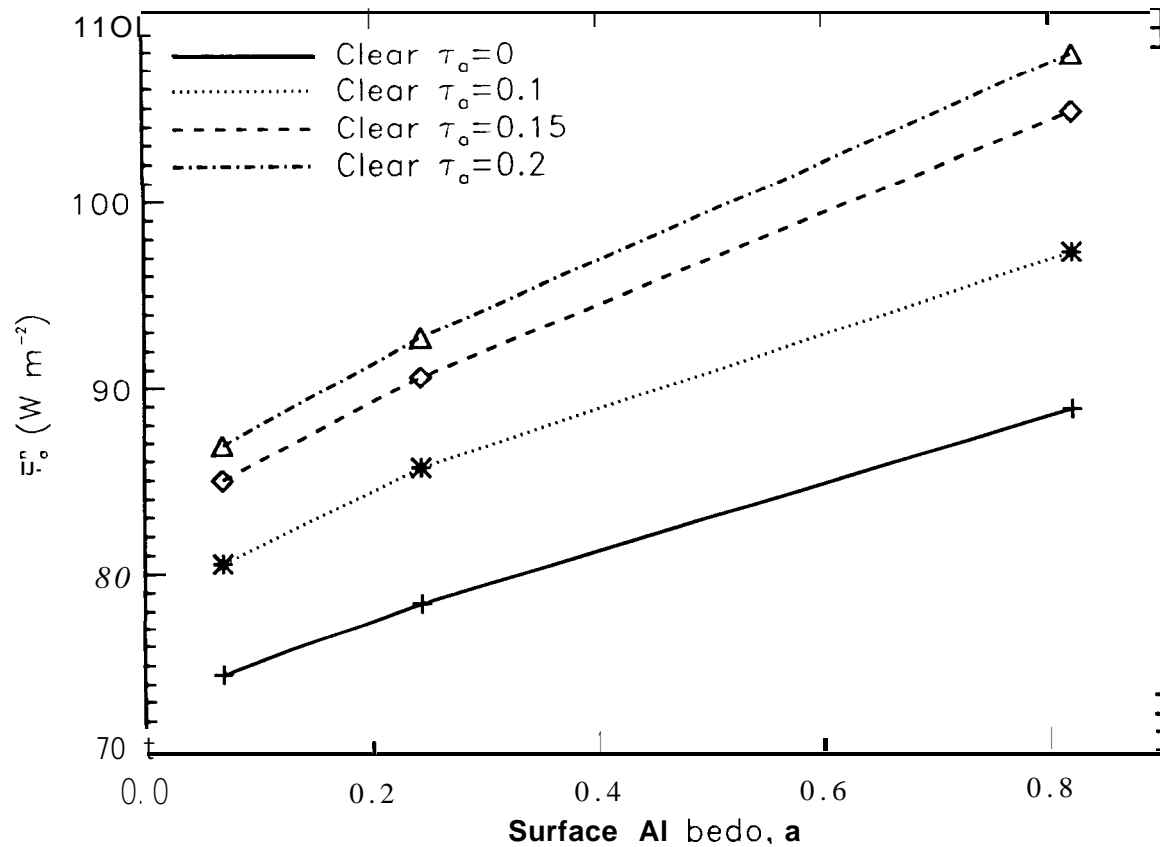


Figure 48. Solar flux absorbed by clear atmospheres as a function of surface albedo and aerosol loading for global-annual-average illumination conditions. The aerosol laden atmospheres have constant particle number densities at altitudes below 12 km (0.2 Bars), the nominal Jaenicke aerosol size distribution, and column-integrated optical depths of 0.1 to 0.2.

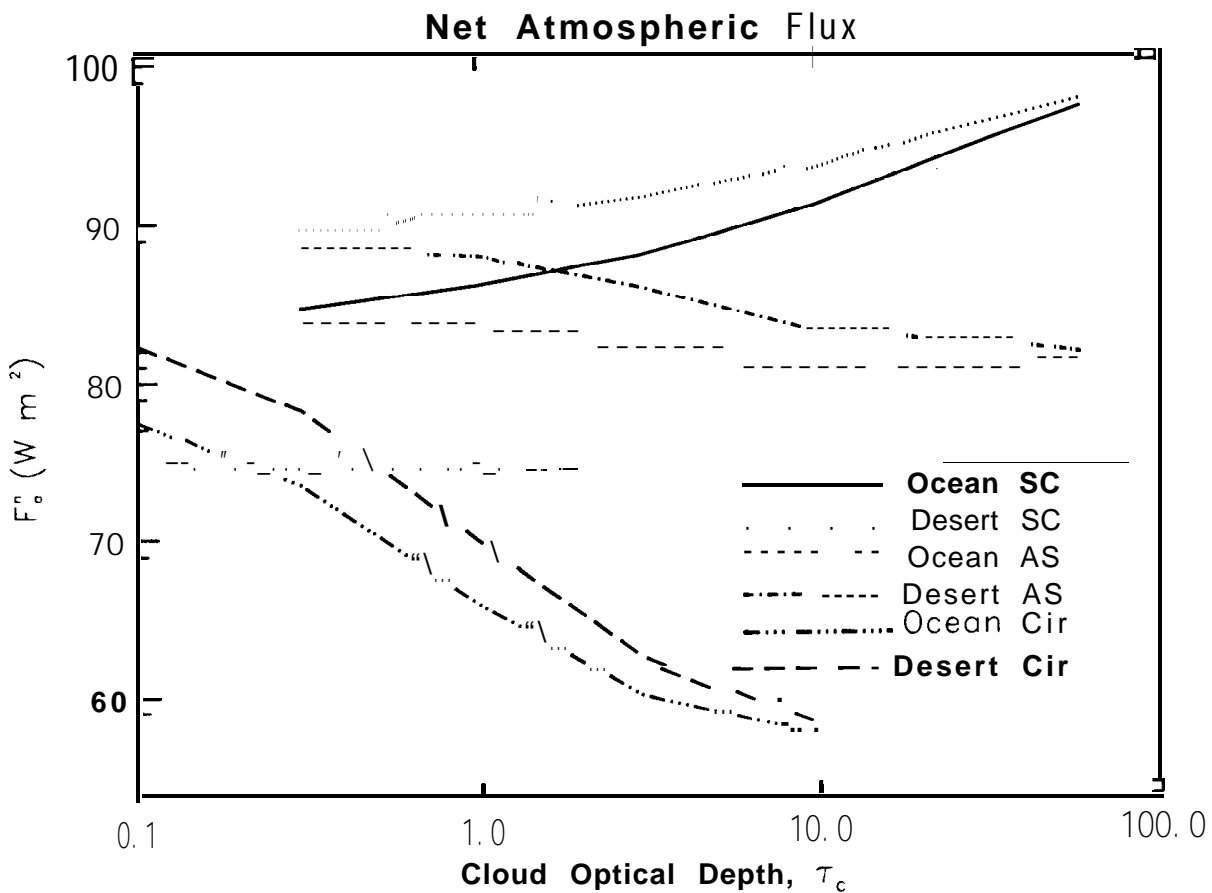


Figure 49. column-integrated atmospheric absorption in cloudy, aerosol-laden atmospheres over dark (Ocean) and moderately-bright (Desert) surfaces for global-annual-average illumination conditions. Each cloudy atmosphere includes a single stratocumulus (SC), altostratus (AS), or cirrus (Cir) cloud, and uniformly-mixed aerosols with the nominal Jaenicke size distribution (Figures 1 and 2), and column-integrated optical depths of 0.1.